Search for
Second-Generation Leptoquarks
in $p\bar{p}$ Collisions

vorgelegt von / submitted by
Tim Christiansen
geboren in / born in Schleswig

Search for
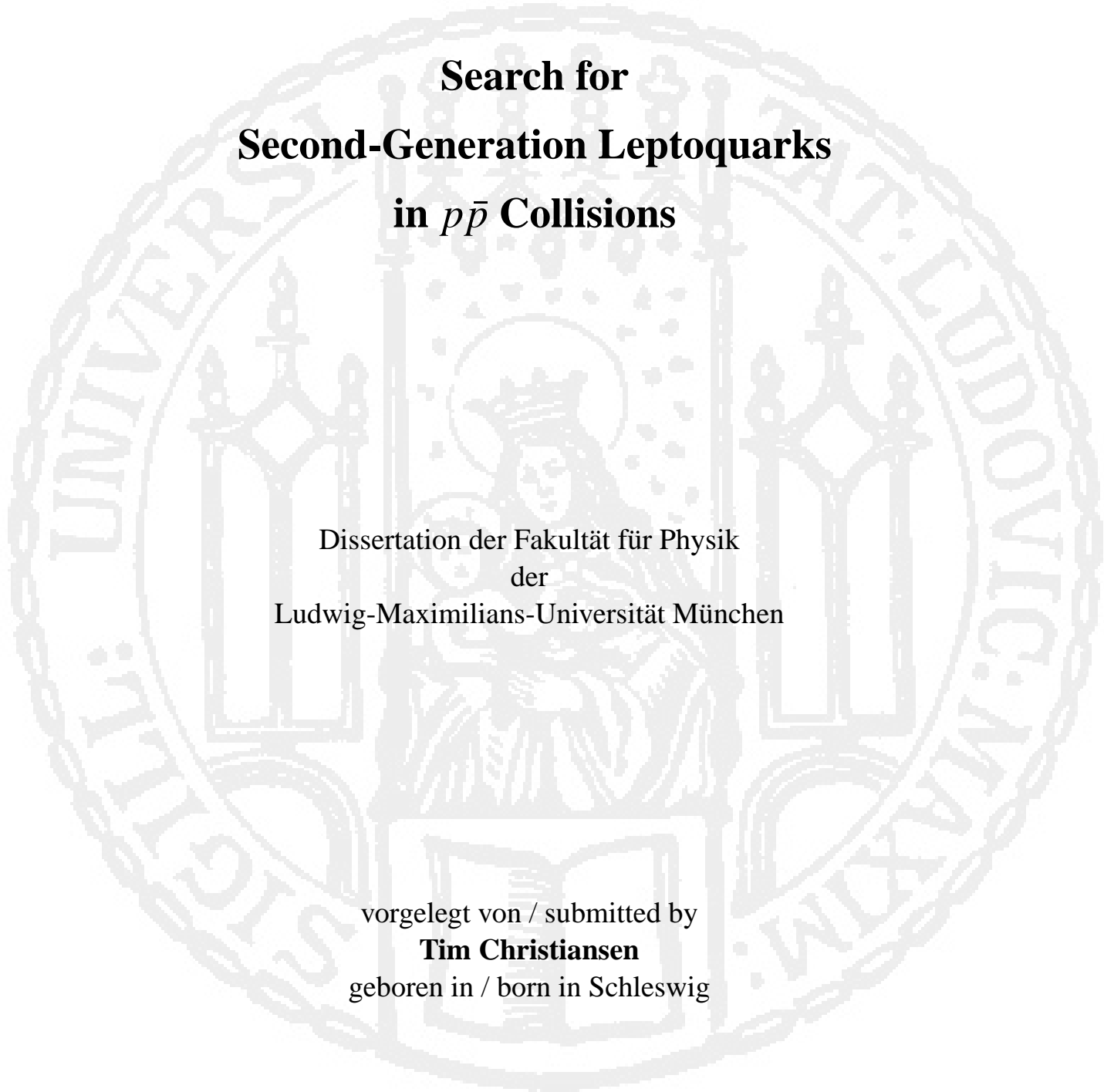# Second-Generation Leptoquarks
in $p\bar{p}$ Collisions

Dissertation der Fakultät für Physik
der
Ludwig-Maximilians-Universität München

vorgelegt von / submitted by
Tim Christiansen
geboren in / born in Schleswig

München, den 23. Dezember 2003

1. Gutachterin / 1st referee: Prof. Dr. Dorothee Schaile
2. Gutachter / 2nd referee: Prof. Dr. Wolfgang Dünnweber

Tag der mündlichen Prüfung /
date of oral exam: 16. März 2004

Zusammenfassung

In diesem Dokument wird die Suche nach Leptoquarks der zweiten Generation (LQ_2) in Proton-Antiproton-Kollisionen beschrieben, die mit dem DØ-Detektor am TeVatron-Beschleuniger aufgezeichnet wurden. Im Zeitraum von September 2002 bis Juni 2003 wurde eine integrierte Luminosität von rund $114\,\text{pb}^{-1}$ bei einer Schwerpunktsenergie von $\sqrt{s} = 1.96\,\text{TeV}$ gesammelt.

Die Vorhersagen des Standardmodells der Teilchenphysik und darüber hinausgehender Modelle mit skalaren Leptoquarks wurden mit den Daten verglichen. Da kein Überschuss an Daten über der Standardmodellvorhersage beobachtet werden konnte, wurde unter der Annahme, dass Leptoquarks zu $100\,\%$ in geladene Leptonen und Quarks zerfallen ($\beta = BF(LQ_2 \rightarrow \mu j) = 100\,\%$), eine untere Schranke von $M_{LQ_2}^{\beta=1} > 200\,\text{GeV}$ ($95\,\%$ C.L.) für die Masse von skalaren Leptoquarks der zweiten Generation ermittelt. Die entsprechende Ausschlussgrenze für $\beta = 1/2$ liegt bei $M_{LQ_2}^{\beta=1/2} > 152\,\text{GeV}$.

Schließlich wurden die Resultate mit den Ergebnissen einer Suche im gleichen Kanal bei DØ Run I kombiniert. Diese Kombination liefert die Ausschlussgrenzen $M_{LQ_2}^{\beta=1} > 222\,\text{GeV}$ ($177\,\text{GeV}$) für $\beta = 1$ ($1/2$) und ist somit für $\beta = 1$ das zur Zeit beste Ergebnis für skalare Leptoquarks der zweiten Generation eines einzelnen Experimentes.

Abstract

This document describes the search for second-generation leptoquarks (LQ_2) in around $114\,\text{pb}^{-1}$ of $p\bar{p}$ collisions, recorded with the DØ detector between September 2002 and June 2003 at a centre-of-mass energy of $\sqrt{s} = 1.96\,\text{TeV}$. The predictions of the Standard Model and models including scalar leptoquark production are compared to the data for various kinematic distributions. Since no excess of data over the Standard Model prediction has been observed, a lower limit on the leptoquark mass of $M_{LQ_2}^{\beta=1} > 200\,\text{GeV}$ has been calculated at $95\,\%$ confidence level (C.L.), assuming a branching fraction of $\beta = BF(LQ_2 \rightarrow \mu j) = 100\,\%$ into a charged lepton and a quark. The corresponding limit for $\beta = 1/2$ is $M_{LQ_2}^{\beta=1/2} > 152\,\text{GeV}$.

Finally, the results were combined with those from the search in the same channel at DØ Run I. This combination yields the exclusion limit of $M_{LQ_2}^{\beta=1} > 222\,\text{GeV}$ ($177\,\text{GeV}$) for $\beta = 1$ ($1/2$) at $95\,\%$ C.L., which is the best exclusion limit for scalar second-generation leptoquarks (for $\beta = 1$) from a single experiment to date.

Contents

1 Introduction

The concept of symmetry[1] in modern physics goes beyond the notion of repetitive patterns or the reflexion of structures as they are commonly known in art. In physics, symmetry is not only related to objects (e.g. structures of crystals), but also to the underlying laws of physical interactions and motion. These symmetries are closely connected to associated conservation laws (Noether theorem). In Particle Physics, for instance, the interaction between elementary particles is described by a symmetry group containing the electromagnetic, the weak and the strong force. The corresponding conserved quantities are the "charges" of these gauge-invariant interactions: the electric charge for the electromagnetic force, the weak isospin for the weak interaction and the "colour-charge" of the strong force.

The Standard Model of Elementary Particle Physics is comprised of the matter particles, the fermions, and contains a description of their interactions, the forces, plus an additional mechanism to obtain mass for the heavy gauge bosons of the (electro-)weak force. The fermions come in three families of leptons (the electron e^-, the muon μ^-, and the tau-particle τ^-, together with the corresponding neutrinos) and three families of quarks (the up (u) and down (d) quark, the charm (c) and strange (s) quark, and the top (t) and bottom quark (b)). In addition, each lepton and quark has an associated antiparticle with opposite electric charge.

Neglecting gravity, which is much weaker than all other known fundamental forces between elementary particles, the Standard Model has shown tremendous success in describing the particles and their interactions as known to date.

None the less, one experimentally finds additional symmetries for which the Standard Model does not supply a further explanation. The observed symmetry in the spectrum of elementary particles between leptons and quarks, i.e. the fact that there exist three generations each, motivates the existence of leptoquarks [1]. Leptoquarks (LQ) are bosons carrying both quark and lepton quantum numbers and fractional electric charge. Although leptoquarks could in principle decay into any combination of a lepton and a quark, experimental limits on lepton number violations, on flavour-changing neutral currents and on

---

[1]The word *symmetric*, which originates from Greek, is probably best "translated" with the terms regular, harmonic in its shape, (counter)balanced, even and uniform.

proton decay lead to the assumption that there would be three different generations of leptoquarks, each coupling to only one quark and lepton family and therefore individually conserving the family lepton numbers [2].

In 1997, the H1 collaboration at the electron(positron)-proton collider HERA observed an excess of events at very high Q^2 [3]. These events, whose number could not be explained by the Standard Model, were $e + p \rightarrow e + j + X$ [2] events with a reconstructed electron(positron)-jet mass[3] clustering around $M(ej) \approx 200\,\text{GeV}$. At the same time, the ZEUS experiment at HERA also observed a small excess of similar events [4], although not quite as compelling as the excess seen by the H1 collaboration.

The existence of leptoquarks deemed to be an interesting, exotic candidate model for such an apparently resonant production of ej events: $e + p \rightarrow LQ + X \rightarrow e + j + X$. Although the excess of high-momentum ej events in deep-inelastic-scattering processes seen by H1 turned out to be merely a statistical fluctuation [5], the result triggered an "avalanche" of theoretical and experimental effort in the particle physics community to search for leptoquarks.

Electron-proton collider experiments, such as H1 and ZEUS at HERA, provide an excellent tool for the direct search for first-generation leptoquarks (LQ_1, coupling to electrons or electron-neutrinos and quarks). However, the sensitivity to second-generation leptoquarks (LQ_2, coupling to quarks and the second lepton family) is much smaller and arises only through virtual corrections. The same is true for the third-generation leptoquarks which also cannot be observed in ep collisions. Hadron colliders such as the TeVatron proton-antiproton collider, on the other hand, are sensitive to all three generations of leptoquarks, provided their masses are sufficiently small.

Assuming 100% branching fraction to a charged lepton and a quark, $\beta = BF(LQ_2 \rightarrow \mu j) = 1$, a pair of second-generation leptoquarks decays into two highly-energetic muons and two highly-energetic jets with no or little missing transverse energy. During the TeVatron Run I, no evidence for the existence of second-generation leptoquarks was found. Therefore, the DØ collaboration published limits on the cross-section of the production of LQ_2-pairs as a function of the leptoquark mass M_{LQ_2} and β. Applying commonly used leptoquark models, these results were translated into lower limits of $M_{LQ_2}^{\beta=1} > 200\,\text{GeV}$ and $M_{LQ_2}^{\beta=1/2} > 180\,\text{GeV}$ (at 95 % confidence level) on the mass of scalar leptoquarks for $\beta = 1$ and $\beta = 1/2$, respectively [6].

In the study presented in this document, about $114\,\text{pb}^{-1}$ of $p\bar{p}$ collisions from Run II, collected with the DØ detector between September 2002 and June 2003, are compared to Standard-Model predictions and predictions from models including scalar second-generation leptoquarks. Since no deviation from the Standard Model is observed, upper

---

[2] The notation j stands for hadronic jets.

[3] For convenience, the units in this document are chosen such that $c = 1$ and $\hbar = 1$. Therefore, energies, masses and momenta all have the units of energies.

limits on the leptoquark cross-section are calculated and translated into lower bounds to the mass of scalar leptoquarks. Consequently, the results are combined with earlier results from DØ Run I in the same channel.

2 Introduction to a World with Leptoquarks

2.1 The Standard Model and Beyond

2.1.1 The Standard Model and its Limitations

The Standard Model (SM) describes the interactions of matter as a gauge theory based on the $SU(3)_C \otimes SU(2)_L \otimes U(1)_Y$ symmetry group. In this model, gravitation is omitted.

All known fundamental particles can be divided into two main groups: fermions of half-integer spin and integer-spin bosons. While fermions are the particles that matter is built of, the forces between the fermions arise from the exchange of spin-1 gauge bosons.

In addition to these gauge bosons, the mediators of the interactions, there is another boson, the yet undetected Higgs boson[1]. The existence of this scalar, i.e. spin 0, particle is a consequence of the Higgs mechanism of spontaneous symmetry breaking which is needed to provide the heavy electroweak gauge bosons, the Z and $W^\pm$ bosons, with non-vanishing masses. For a general and more detailed description of the Standard Model, the reader is referred to [7].

The Standard Model has proven to be a remarkable success. It has withstood all its experimental challenges. But despite of all its successes, the SM is unlikely to be the final theory even if we neglect gravity. We require a theory which not only describes the fundamental particles and their interactions at the energy scales accessible to date but also at much higher energies up to the Planck scale, M_{Planck}, at which gravity becomes too large to be neglected in particle physics. Many questions already arise at much lower scales than M_{Planck}:

- Why are the local SM gauge interactions the $SU(3)_C \otimes SU(2)_L \otimes U(1)_Y$ with three independent local SM gauge couplings?

---

[1]The Standard Model usually contains a single observable Higgs boson, although there are variations of the underlying Higgs mechanism, which would imply one or more additional Higgs particles.

- Why are there three families of quarks and leptons?

- What determines (and what is the origin of) the quark and lepton masses, or the apparent hierarchy of family masses and quark mixing angles?

- Why does each family consist of the states (Q, u_R, d_R, L, and e_R), where $Q = (u, d)$ and $L = (v, e)$ are $SU(2)_L$ doublets and u_R, d_R, and e_R are $SU(2)_L$ singlets?

Furthermore, if the charge quantisation were understood, we would also understand why there are no fractionally[2] charged hadrons.

In addition to these problems concerning the Standard Model in itself, there are additional problems like the almost complete matter-antimatter asymmetry observed in the universe—which appears too strong to originate from a complex phase in the CKM matrix as seen in e.g. the neutral Kaon system—or the nature of dark matter and dark energy. The Standard Model has 19 arbitrary parameters, which are chosen to fit the experimental data: three gauge couplings, nine charged fermion masses, three quark-mixing angles and a phase in the complex CKM matrix, the Z (or $W^\pm$) and the Higgs mass. Additional parameters for the neutrino masses and neutrino mixing angles are also not predicted by the SM, but are arbitrary values as well. In summary, the Standard Model has too many arbitrary parameters and leaves too many questions unresolved to be considered complete. Theories beyond the Standard Model try to address these problems. [8]

The following sections will briefly introduce a few of these *new* theories with a focus on models in which new particles with new lepton-quark interactions appear. This list is, by far, incomplete, but it will show that there is a whole range of models beyond the Standard model in which leptoquarks arise, in one way or another, as *natural* consequence.

2.1.2 Leptoquarks in Grand Unified Theories

Leptoquarks (*LQ*), new bosons carrying both quark and lepton quantum numbers, can emerge in various theories beyond the Standard Model. As an example of how leptoquarks could enter the scene of particle physics, this section describes in a simplified and incomplete fashion the first steps and symmetry arguments that lead to Grand Unified Theories (GUTs). Grand Unified Theories, which exist in a whole range of GUT derivatives, usually imply the existence of leptoquarks. This introduction closely follows reference [9]. For a general view of Grand Unified Theories see [10].

Ignoring gravity for the moment, the aim of Grand Unified Theories is to find a gauge group G, with a single coupling constant, that describes all known Standard-Model interactions and therefore contains $SU(3)_C \otimes SU(2)_L \otimes U(1)_Y$ as a sub-group. Naturally, in

---

[2]Fractionally with respect to the elementary charge, i.e. the charge of the electron $|Q_{em}(e^-)|$.

GUT theories, an energy scale exists, at which the $SU(3)_C$, $SU(2)_L$, and $U(1)_Y$ couplings unite. This scale, M_{GUT}, must be very large, since the couplings are quite different at the electro-weak scale ($O(M_Z)$) and since they change logarithmically with energy.

Since $SU(3)_C \otimes SU(2)_L \otimes U(1)_Y$ is a sub-group of G, the photon must be one of G's gauge bosons and the charge operator Q_{ch} one of the generators of G. Since all of the generators of G are represented by traceless matrices, $Tr(Q_{ch}) = 0$ must be true in any irreducible representation of G. As a consequence, the sum of all electric charges of all particles vanishes, which is indeed satisfied within each fermion family (e.g. $Q(e) + Q(\nu_e) + \sum_{c=1}^{3}(Q(u_c) + Q(d_c)) = -1 + 0 + 3(2/3 - 1/3) = 0$). This relationship between the quark and lepton charges is not valid if the quark and lepton sectors are considered separately. In other words, we already see an indication for G containing bosons, which "transform" leptons into quarks and vice-versa.

$SU(5)$ is the smallest group with the required properties, i.e. it contains the $SU(3) \otimes SU(2) \otimes U(1)$ as a subgroup. Herein, the eight Gell-Mann matrices of $SU(3)_C$, the three Pauli matrices of $SU(2)_L$, and the phase of $U(1)_Y$ are replaced by 24 hermitian and traceless matrices. $SU(5)$ is assumed to be a local symmetry and each of the generators corresponds to a gauge boson. In $SU(5)$, a fermion family can be accommodated in the $\bar{\mathbf{5}}$ and $\mathbf{10}$ representations of the gauge group. The $SU(3) \otimes SU(2)$ content for each family then becomes:

$$\begin{aligned}
\bar{\mathbf{5}} &= (\bar{3},1) + (1,2) = \bar{d}_c + (\nu_l, l^-), \\
\mathbf{10} &= (\bar{3},1) + (3,2) + (1,1) = \bar{u}_c + (u_c, d_c) + l^+,
\end{aligned}$$

where the index c denotes the three colours of QCD and where the letters u (d) represent the up-type (down-type) quarks of each family.

The gauge bosons belong to the 24 adjoint representation:

$$\mathbf{24} = \underbrace{(3,2) + (\bar{3},2)}_{\binom{X}{Y}\,^{Q_X=4/3}_{Q_Y=1/3}} + \underbrace{(8,1)}_{8 \text{ gluons}} + \underbrace{(1,3) + (1,1)}_{\gamma, Z, W^{\pm}}. \tag{2.1}$$

Equation 2.1 reveals twelve new gauge bosons, X and Y with the charges $\pm 4/3$ and $\pm 1/3$, respectively. These gauge bosons belong to a doublet of $SU(2)_L$ and a triplet of $SU(3)_C$.

A 24-plet of Higgs bosons can provide the first stage of symmetry breaking from $SU(5)$ down to $SU(3)_C \otimes SU(2)_L \otimes U(1)_Y$ in the most simple fashion. The super-heavy X and Y bosons get their masses through absorbing twelve of these Higgs bosons as their longitudinal components, while the remaining twelve Higgs bosons are additional super-heavy particles. The second stage of symmetry breaking down to $SU(3)_C \otimes U(1)_{em}$ is the usual electro-weak symmetry breaking. The remaining two symmetries are unbroken (i.e.
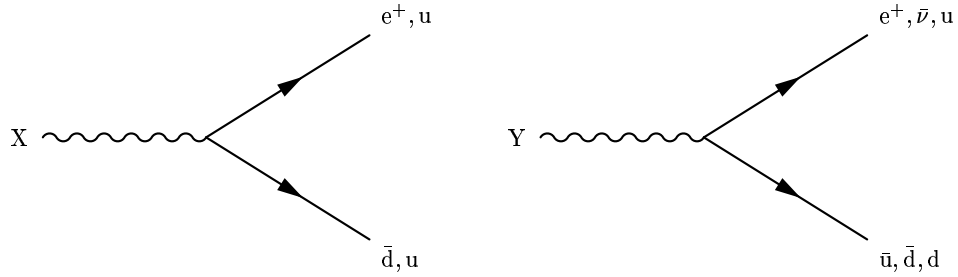
Figure 2.1: Basic vertices of the X and Y bosons of a minimum $SU(5)$ GUT. The light leptoquarks of the modified $SU(5)$ GUT proposed by H. Murayama and T. Yanagida (1992) [14] have the same basic vertices apart from the di-quark couplings.

exact). As discussed in reference [9] this *minimum SU(5)* model encounters problems, because is requires the mass ratios of $m(d)/m(s)$ and $m(e)/m(\mu)$ to be equal even at the electroweak scale, which is in strong disagreement with the actual observation of the fermion mass spectrum.

Another experimental test of Grand Unified Theories such as the $SU(5)$ model comes from the GUT prediction of the Weinberg angle $\sin^2\theta_W$. At the GUT scale M_{GUT}, the minimum $SU(5)$ model fixes $\sin^2\theta_W(M_{\text{GUT}})$ to $\frac{3}{8}$, following from the equality of the coupling constants at M_{GUT} and other symmetry arguments [9, 11]. Propagated down to the electroweak scale, this leaves

$$\sin^2\theta_W(M_{\text{W}}) = 0.214 \pm 0.004 \ [13], \tag{2.2}$$

which is close to but in disagreement with the observed value of $\sin^2\theta_W = 0.2224 \pm 0.0002$ [12] [3] by around two standard deviations.

Furthermore, Grand Unified Theories predict transitions between quarks and leptons, and thus imply the decay of the proton and the bound neutron or nucleon-antinucleon oscillations. These predictions can be understood by considering the basic vertices of the X and Y bosons, shown in Figure 2.1, where these bosons have both lepton-quark and quark-quark couplings. These vertices violate the baryon (B) and lepton numbers (L), however, they conserve $B - L$. With a predicted GUT scale of about $M_{SU(5)\,\text{GUT}} \simeq 10^{15}\,\text{GeV}$, such minimum $SU(5)$ models yield a life-time for the proton which is ruled out by experiments.

A way to avoid the disagreement between these and similar predictions from the minimum $SU(5)$ model is to apply additional constraints and use a different symmetry-breaking scheme as described by H. Murayama and T. Yanagida (1992) [14]: Murayama

---

[3]In this context, $\sin^2\theta_W$ is defined as $\sin^2\theta_W = 1 - \frac{M_W^2}{M_Z^2}$ and is calculated with the W and Z boson masses $M_W = (80.412 \pm 0.042)\,\text{GeV}$ [12] and $M_Z = (91.1875 \pm 0.0021)\,\text{GeV}$ [12].

and Yanagida point out that the difficulties of a $SU(5)$ GUT with the experimental boundary to the proton lifetime and the measurement of the Weinberg angle can both be overcome by introducing a pair of light leptoquarks with masses of the order of $M(Z)$, while the other new bosons (cf. eq. (2.1)) remain super-heavy. The pair of light scalar leptoquarks would have couplings to leptons and quarks like the X and Y bosons in Figure 2.1, apart from di-quark couplings, and thus conserves the lepton and baryon numbers separately. The *mass splitting*, i.e. that all particles are either super-heavy ($M > O(10^{15}\,\text{GeV})$) or light ($M \leq O(100\,\text{GeV})$), which is the central idea of this model, also applies to the Higgs bosons and is referred to as the "desert" hypothesis. Although this refined $SU(5)$ model pushes the proton lifetime to a value, which is in accordance with current experimental limits [4], it bares the disadvantage that it requires an extensive fine-tuning to cope with the particles' loop contributions to the Higgs mass. On the other hand, its predictions of both the strong coupling constant $\alpha_s(M_Z)$ (using the measured low-energy values for the electromagnetic and weak couplings α_1 and α_2 as an input and requiring $\alpha_1 = \alpha_2 = \alpha_3$ at the GUT scale) and the weak mixing angle $\sin^2 \theta_W$ are compatible with experimental results [14].

Of course, there are more possibilities for the gauge group G, of which $SU(5)$ is only the most simple option that contains $SU(3)_C \otimes SU(2)_L \otimes U(1)_Y$. $SO(10)$, for instance, provides complete unification with one universal coupling constant. One of the two maximal breaking patterns, $SO(10) \to SU(4)_C \otimes SU(2)_L \otimes SU(2)_R$, leading to the Pati-Salam GUT model [15], predicts weak-isospin singlet vector leptoquarks. In this model, the lepton sector is treated as a fourth colour, thus leading to $SU(4)_C$.

2.1.3   Superstring Inspired E_6 Models

Among the most interesting GUT alternatives are superstring inspired E_6 models [16]. E_6 (one of the five so-called *exceptional* Lie algebras) has rank 6 and its fundamental representation is **27** (27 dimensions). From a "GUT point of view", E_6 is just the continuation of the sequence $SU(5)$ (rank-4 group) and $SO(10)$ (rank-5 group). The ten-dimensional Superstring theory $E_8 \otimes E_8'$ [5] has been shown to be free of anomalies [17]. In order to reduce this theory down to an effective low-energy theory in the usual four dimensional space-time, it is assumed that the ten dimensions compactify to four dimensions at the Planck scale $M_{\text{Planck}} \approx 10^{19}\,\text{GeV}$. This can be achieved if the compactified six-dimensional space resembles an $SU(3)$ structure, i.e. with the breaking $E_8 \to SU(3) \otimes E_6$

---

[4]It appears, that the proton lifetime, $7 \cdot 10^{29}\,\text{y} < \tau_{\text{GUT}}(\text{p} \to \text{e}^+ + \pi^0) < 7 \cdot 10^{32}\,\text{y}$, predicted by the modified $SU(5)$ GUT model described in [14], is yet again excluded by the latest limits of $\tau_{90\%\,\text{C.L.}}(p \to e^+ + \pi^0) > 1.6 \cdot 10^{33}\,\text{y}$, measured with the Super-Kamiokande experiment in 1998 (see [8] and references therein).

[5]The group $SU(32)$ is also anomaly-free in a ten-dimensional superstring theory, as has been shown by Green and Schwarz [17], but $E_8 \otimes E_8'$ has the interesting feature that it automatically leads to chiral fermions.

leading to the E_6-group as an effective GUT group (therefore the term "superstring inspired"). The remaining E_8' group interacts with the *normal* E_6 fields only through gravitation and might play the role of the "hidden sector" in supergravity models. The hidden sector is necessary to generate terms in the Lagrangian which are responsible for the supersymmetry breaking (see [18] and references therein). Furthermore, the generational problem, i.e. why there is not only one family but two more "approximately identical" copies, may be solved because it is expected that any theoretically favoured compactification scheme generates the appropriate number of generations.

Superstring inspired E_6 models contain a large number of particles in addition to those present in the Standard Model: Superpartners of the known matter fermions and gauge bosons, scalar di- or leptoquarks, extended gauge and Higgs bosons and new "exotic" quarks and leptons. However, most of these particles tend to be very heavy and since there are many ways of implementing the Higgs sector, it is quite involved to predict strong upper bounds to the masses of leptoquarks. A detailed description of superstring inspired E_6 models can be found in the references [16, 18].

2.1.4 Leptoquark-like Couplings in R-Parity violating Supersymmetry

Leptoquark-like couplings appear in some supersymmetric models. Supersymmetry models (SUSY), of which there exists a whole variety of derivatives, have in common that they propose the existence of so-called super-partners to the Standard-Model fermions and bosons. The super-partners, which are assumed to be sufficiently massive in order to have escaped experimental observation so far, are usually written with a *tilde*, e.g. the notation of the super-partner of a quark q, the *squark*, is $\tilde{q}$. For a general view of Supersymmetry, the reader is referred to [19].

SUSY models are often broken down into two distinct categories, those which conserve and those which violate R-parity. Simply speaking, R-parity in Supersymmetry models refers to the requirement that SUSY particles can only be created in pairs of a SUSY particle and a SUSY anti-particle, which can be seen from the definition of the discrete, multiplicative quantum number

$$R = (-1)^{3B+L+2S}, \tag{2.3}$$

where B and L are the baryon and lepton numbers, respectively, and S denotes the spin of the particle. SM particles, therefore, have $R = +1$, while $R = -1$ is assigned for their supersymmetric partners. If R-parity is required, supersymmetric particles could only be created in pairs, and the lightest SUSY particle would be stable.

Squarks in *R*-parity violating models, however, might possess leptoquark-like decay modes through Yukawa couplings. The $\tilde{u}$-like[6] and $\tilde{d}$-like squarks (which are bosons with spin 0) can have leptoquark couplings. For instance, the $\tilde{u}_L$ (the super-partner of the left-handed up-quark) couples to $\nu_e + u$ or $e^- + d$ pairs just like first-generation leptoquarks of charge $-1/3$. As a general consequence, it is possible to translate constraints on the λ_{lq} coupling of the $LQ - l - q$ vertex from leptoquark searches into constraints on the couplings of squarks in *R*-parity violating supersymmetry [20].

2.2 The Effective Leptoquark Model

Direct searches for leptoquarks at collider experiments are usually carried out in the context of effective models. Following reference [20], this chapter introduces the phenomenology of leptoquark interactions essential to leptoquarks in reach of hadron colliders such as the TeVatron.

The assumptions that leptoquarks

  I) have renormalisable interactions,

 II) have interactions invariant under the Standard Model gauge groups
      $SU(3) \otimes SU(2) \otimes U(1)$, and

III) couple to Standard-Model fermions and gauge bosons only,

lead to the most general effective Lagrangian for leptoquark interactions [21]. In order to preserve the stability of the proton, leptoquarks

 IV) are required to conserve the leptonic number L_l and the baryonic number B_q separately,

i.e. leptoquarks are bosons which carry both the (family) lepton and the quark quantum-numbers, which are conserved in leptoquark interactions. Such leptoquarks carry the fermionic number

$$F = 3B_q + L_l \tag{2.4}$$

of either $|F| = 0$ or $|F| = 2$ and the interactions with quarks and leptons is described by the Lagrangian

$$\mathcal{L} = \mathcal{L}_{|F|=2} + \mathcal{L}_{|F|=0} \tag{2.5}$$

---

[6]The suffix "like" in this context is understood in the following sense: Since supersymmetry, if it exists, must be broken (otherwise SUSY particles would have the same mass as their SM partners and therefore would have already been observed), the mass and the interaction Eigenstates of the SM particles and their SUSY partners need not to be identical, but mixings generally appear.

$|F| = 2$ Leptoquarks				$|F| = 0$ Leptoquarks			
LQ	Q_{em}	T_3	Decay	LQ	Q_{em}	T_3	Decay
$S_{0,L}$	$-1/3$	0	$l_L^- u_L$ or $\nu_L d_L$	$V_{0,L}$	$-2/3$	0	$l_L^- \bar{d}_R$ or $\nu_L \bar{u}_R$
$S_{0,R}$			$l_R^- u_R$	$V_{0,R}$			$l_R^- \bar{d}_L$
$\hat{S}_{0,R}$	$-4/3$	0	$l_R^- d_R$	$\hat{V}_{0,R}$	$-5/3$	0	$l_R^- \bar{u}_L$
$S_{1,L}$	$-4/3$	-1	$l_L^- d_L$	$V_{1,L}$	$-5/3$	-1	$l_L^- \bar{u}_R$
	$-1/3$	0	$l_L^- u_L$ or $\nu_L d_L$		$-2/3$	0	$l_L^- \bar{d}_R$ or $\nu_L \bar{u}_R$
	$+2/3$	$+1$	$\nu_L u_L$		$+1/3$	$+1$	$\nu_L \bar{d}_R$
$V_{1/2,L}$	$-4/3$	$-1/2$	$l_L^- d_R$	$S_{1/2,L}$	$-5/3$	$-1/2$	$l_L^- \bar{u}_L$
$V_{1/2,R}$	$-4/3$		$l_R^- d_L$	$S_{1/2,R}$	$-5/3$		$l_R^- \bar{u}_R$
	$-1/3$	$+1/2$	$l_R^- u_L$		$-2/3$	$+1/2$	$l_R^- \bar{d}_R$
$\hat{V}_{1/2,L}$	$-1/3$	$-1/2$	$l_L^- u_R$	$\hat{S}_{1/2,L}$	$-2/3$	$-1/2$	$l_L^- \bar{d}_L$
	$+2/3$	$+1/2$	$\nu_L u_R$		$+1/3$	$+1/2$	$\nu_L \bar{d}_L$

Table 2.1: Scalar (S) and vector (V) leptoquarks incorporated in the mBRW model, grouped with respect to the weak isospin and the absolute value of the fermionic number F (see equation 2.4). Q_{em} is the electromagnetic charge of the leptoquark (LQ) while T_3 is the third component of the weak isospin. The third row shows the possible decay products of the various leptoquarks.

where $\mathcal{L}_{|F|=0,2}$ are given by

$$
\begin{aligned}
\mathcal{L}_{|F|=2} &= (g_{1L}\bar{q}_L^c i\tau_2 l_L + g_{1R}\bar{u}_L^c i e_R^-)S_0 + \hat{g}_{1R}\bar{d}_R^c e_R^- \hat{S}_0 + g_{3L}\bar{q}_L^c i\tau_2 \tau l_L S_1 \\
&\quad + (g_{2L}\bar{d}_R^c \gamma^\mu l_L + g_{2R}\bar{q}_L^c \gamma^\mu e_R^-)V_{1/2\mu} + \hat{g}_{2L}\bar{u}_R^c \gamma^\mu l_L \hat{V}_{1/2\mu} + h.c. \\
\mathcal{L}_{|F|=0} &= (h_{1L}\bar{q}_L \gamma^\mu l_L + h_{1R}\bar{d}_R \gamma^\mu e_R^-)V_{0\mu} + \hat{h}_{1R}\bar{u}_R \gamma^\mu e_R^- \hat{V}_{0\mu} + h_{3L}\bar{q}_L \tau \gamma^\mu l_L V_{1\mu} \\
&\quad + (h_{2L}\bar{u}_R l_L + h_{2R}\bar{q}_L i\tau_2 e_R^-)S_{1/2} + \hat{h}_{2L}\bar{d}_R l_L \hat{S}_{1/2} + h.c.
\end{aligned}
$$

Herein, q_L and l_L denote the left-handed quark and lepton $SU(2)$ doublets while e_R, d_R, and u_R are the corresponding right-handed singlets for leptons, down-type and up-type quarks. The superscript c is the charge conjugate of the corresponding fermion field: $\psi^c \equiv C\bar{\psi}^T$. The subscripts L and R refer to coupling constants corresponding to the chirality of the fermion involved. Indices referring to the $SU(3)$ colour and the three generations are dropped in this notation. S_T and V_T denote the scalar and vector leptoquarks, their index $T = 0$, $1/2$, or 1 refers to the weak isospin. g_i, $\hat{g}_i$, h_i, and $\hat{h}_i$ are the various leptoquark couplings to quarks and leptons. This effective leptoquark model, together with its Lagrangian (2.5), will henceforth be referred to as the Minimum Buchmüller-Rückl-Wyler model (mBRW) [21]. The new particles incorporated in this model are summarised in Table 2.1. This generic leptoquark model allows different couplings to left- and right-handed fermions, hence the indices L and R for the leptoquarks distinguish the chirality of the coupled lepton.

With the above choice of an effective Lagrangian for the leptoquark interactions with lepton-quark pairs, i.e. a Lagrangian which preserves the gauge symmetries of the Standard Model, the possible representations of the leptoquarks with respect to the gauge groups and the couplings to the gauge bosons are in principle determined. While this is strictly true for scalar leptoquarks, the cross-section for vector leptoquarks depends on their trilinear and quartic couplings to gauge bosons, which might require damping by the introduction of anomalous couplings. The anomalous couplings for vector lepto-quarks can be parameterised by in total six a priori undetermined couplings (four for the electro-weak, another two for the strong sector) and are free parameters of the effective model. For a detailed discussion of the interaction of vector leptoquarks with the SM gauge bosons, the reader is referred to the references [22, 23].

Another two useful constraints reduce the number of free parameters: In the mBRW model, leptoquarks

V) each couple to a single lepton-quark generation only and

VI) each have pure chiral couplings to Standard Model fermions.

After imposing these additional constraints, the different Yukawa couplings g, $\hat{g}$, h, and $\hat{h}$ of the Lagrangian (2.5) can be described by the generic symbol λ. The restriction (V) on intra-generational connections avoids flavour-changing neutral currents and flavour-universality violations at tree-level, and the last restriction (VI) removes direct contributions to chirally suppressed meson decays such as $\pi \to e\nu_e$ as well as virtual-loop contributions to the $g-2$ of the muon. Thus, introducing these two additional restrictions allows relatively small leptoquark masses in reach of today's hadron colliders [2, 21].

Theoretical Interpretations of the Effective Leptoquark Model

For experimental searches, like the search for scalar leptoquarks of the second generation presented here, degeneracy of the masses within each isospin family of the leptoquarks is generally assumed, since one would expect all leptoquarks within a given $SU(2)$ representation to have equal mass, loop-corrections aside. For instance, $S_{1/2,L}$ denotes both the leptoquark $S_{1/2}$ states of electric charge $-5/3$ and $-2/3$, coupling to a left-handed lepton. Consequently, we distinguish 14 types of leptoquarks: seven scalars ($S_{0,L}$, $S_{0,R}$, $\hat{S}_{0,R}$, $S_{1,L}$, $S_{1/2,L}$, $S_{1/2,R}$, and $\hat{S}_{1/2,L}$) and seven vectors ($V_{1/2,L}$, $V_{1/2,R}$, $\hat{V}_{1/2,L}$, $V_{0,L}$, $V_{0,R}$, $\hat{V}_{0,R}$, and $V_{1,L}$) as can be seen in Table 2.1.

A specific underlying theory usually predicts only a subset of the allowed mBRW-leptoquark states: The leptoquark state in superstring-inspired E_6 theories corresponds to the $S_{0,L}$ state [16], while the anti-$\hat{S}_{1/2}$ of Table 2.1 can represent the light iso-doublet

of leptoquarks arising in a model which attempts to reconcile $SU(5)$ GUTs with the experimental limits on the stability of the proton and the observed Weinberg angle $\sin^2\theta_W$ [14, 24]. A weak-isospin singlet vector leptoquark of hypercharge 2/3, corresponding to the leptoquark state V_0, appears in the Pati-Salam GUT model [15], while *all fourteen* states of Table 2.1 appear in a GUT theory based on the $SU(15)$ gauge group [25].

As briefly discussed in section 2.1.4, leptoquark searches can have implications for experimental constraints of R-parity violating supersymmetry models. The $\tilde{u}$-like and the $\tilde{d}$-like squarks, for instance, can have leptoquark couplings similar to those of the $\hat{S}_{1/2}$ and S_0 scalar leptoquarks. The $\tilde{u}_L$ may couple to an $e^+ + d$ pair via a Yukawa coupling λ'_{111} in a way, similar to the coupling of the first-generation $\hat{S}_{1/2,L}$ leptoquark, while the same coupling determines the processes $\tilde{d}_R \to e^- + u$ and $\tilde{d}_R \to \nu_e + d$, represented by the $S_{0,L}$ with charge 1/3. For leptoquarks from GUT models, the branching ratios $\beta = BF(LQ \to l + q)$ are, by construction, 1, 1/2, or 0. In the case of R-parity violating SUSY, however, it might be reasonable to assume, contrary to assumption (III), that leptoquarks (squarks) couple to other (unspecified) new fields, leaving β a free parameter of the search analysis [20].

2.3 Leptoquark Production and Decay

In $p\bar{p}$ collisions, leptoquarks can be produced either singly or in pairs. The cross-section for single production, however, relies on the size of the unknown Yukawa coupling λ_{lq} of the leptoquark and is therefore model dependent (see Feynman graph in Figure 2.2). Pair production, on the other hand, proceeds through QCD interactions and thus depends only on the leptoquark spin and on the fact that it is a colour-triplet field. The lowest-order Feynman diagrams for leptoquark pair-production and decay are shown in the Figures 2.3 and 2.4. Unless the Yukawa couplings, which are governed by the electroweak interactions, are rather large (e.g. of the order of the electromagnetic strength or stronger), the pair production mechanism will be dominant [26]. The important result is that the pair production of both scalar and vector leptoquarks in hadron collisions is not dependent on the electroweak properties of the leptoquark itself, as opposed to the production in lepton-proton colliders such as HERA. Of course, the reverse is true as well, meaning that the production properties cannot be used to probe the detailed structure of the leptoquark type. Furthermore, pair production allows the search for all three generations of leptoquarks at hadron colliders, while ep colliders (such as HERA) or e^+e^- colliders (such as LEP) are mainly sensitive to first-generation leptoquarks involving electrons ans/or electron-neutrinos.

Michael Kraemer et al. [27] have provided a tool to calculate the leading order and next-to-leading order cross-sections for the pair production of scalar leptoquarks of arbitrary mass. These results are used when translating the cross-section limits, determined
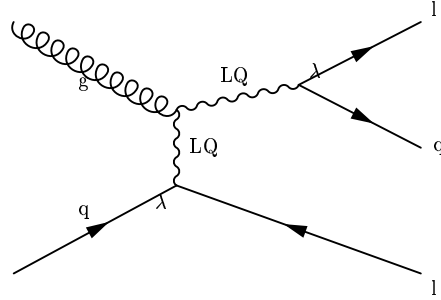
Figure 2.2: Example of single-leptoquark production (*t*-channel) in $p\bar{p}$ collisions.

in this analysis, into lower limits to the mass of scalar leptoquarks. These cross-sections were obtained using the parton density function CTEQ4M provided by [28]. In order to account for the correct centre-of-mass energy, $\sqrt{s} = 1.96\,\text{TeV}$, the calculations described in reference [27] are repeated using the updated parameters for the TeVatron Run II. This calculation includes the Feynman-graphs in Figure 2.3 a)-e) as well as the additional gluon-quark subprocesses shown in Figure 2.4. The resulting cross-sections are shown in Figure 2.5, together with the pair-production cross-sections for vector-leptoquarks with *Yang-Mills* and *Minimal-Vector* couplings.

2.4   Summary of Experimental Results

This section will give a brief overview of a few experimental results from leptoquarks searches and indirect measurements. For a detailed summary of experimental limits from leptoquark searches, the reader is referred to [20, 29].

Although direct searches for leptoquarks were also performed for e^+e^- collisions, the stringent limits come from $p\bar{p}$ and $e^{\pm}p$ collider experiments. A summary of the results for direct searches is given in Tables 2.2-2.5. The advantage of leptoquark searches in hadron collisions is that the pair production cross-section is independent of the a priori unknown leptoquark-lepton-quark coupling λ_{lq}. Searches in lepton-proton collider experiments can only determine a lower mass bound for leptoquarks for a given coupling λ_{lq}. On the other hand, the pair-production of vector leptoquarks in proton-antiproton collisions depends on anomalous couplings to gauge bosons, and the limits are usually calculated for *Yang-Mills* or *Minimal Vector* models.

Figure 2.6 shows the exclusion limitsfor scalar first-generation leptoquarks in the $\lambda_{lq} - M_{LQ_1}$ plane from various $p\bar{p}$, $e^{\pm}p$, and e^+e^- collider experiments.

Direct limits for scalar first-generation leptoquarks			
β	Lower mass limit [GeV] for		Channel/Assumptions
	any λ_{lq}	$\lambda_{lq} \geq 0.1$	$\lambda_{lq} \geq 0.3$	
1	242	-	-	$p\bar{p} \to eqeq + X$
	-	282	298	$e^+u \to LQ^{F=0} \to eq$
	-	246	270	$e^+d \to LQ^{F=0} \to eq$
	-	276	296	$e^-u \to LQ^{F=2} \to eq$
	-	249	278	$e^-d \to LQ^{F=2} \to eq$
1/2	204	-	-	$p\bar{p} \to eq\nu q(eqeq;\nu q\nu q) + X$
	-	275	292	$e^+u \to LQ^{F=0} \to eq$
	-	235	265	$e^+d \to LQ^{F=0} \to eq, \nu q$
	-	271	294	$e^-u \to LQ^{F=2} \to eq, \nu q$
	-	231	271	$e^-d \to LQ^{F=2} \to eq$
0	98	-	-	$p\bar{p} \to \nu q\nu q$
	-	237	262	$e^+d \to LQ^{F=0} \to \nu q$
	-	268	293	$e^-u \to LQ^{F=2} \to \nu q$

Table 2.2: Collider constraints on scalar first-generation leptoquarks [20, 29]. The lower mass limits are calculated at 95 % confidence level. $\beta = BF(LQ \to eq)$ is the branching fraction of leptoquarks into a charged lepton and a quark. For $\beta = 1/2$ limits, when both eq and νq decays are used, $\beta + BF(LQ \to \nu q) = 1$ is assumed. The searches were either performed for $p\bar{p}$ (independent of LQ-lepton-quark coupling λ_{lq}) or $e^{\pm}p$ collisions. The results are quoted from [20, 29] and references therein.

Direct limits for first-generation vector-leptoquarks from $e^{\pm}p$ collisions			
β	Lower mass limit [GeV] for		Channel/Assumptions
	$\lambda_{lq} \geq 0.1$	$\lambda_{lq} \geq 0.3$	
1	272	283	$e^+u \to LQ^{F=0} \to eq$
	264	292	$e^+d \to LQ^{F=0} \to eq$
	275	295	$e^-u \to LQ^{F=2} \to eq$
	246	277	$e^-d \to LQ^{F=2} \to eq$
1/2	266	281	$e^+u \to LQ^{F=0} \to \nu q$
	260	290	$e^+d \to LQ^{F=0} \to eq, \nu q$
	276	295	$e^-u \to LQ^{F=2} \to eq, \nu q$
	230	271	$e^-d \to LQ^{F=2} \to eq$
0	268	300	$e^+d \to LQ^{F=0} \to \nu q$
	280	295	$e^+u \to LQ^{F=2} \to \nu q$

Direct limits for first-generation vector-leptoquarks from $p\bar{p}$ collisions			
β	Lower mass limit [GeV] for $LQ \leftrightarrow$ boson couplings:		Channel/Assumptions
	Min. Vec.	Yang-Mills	
1	292	345	$p\bar{p} \to eqeq + X$
1/2	282	337	$p\bar{p} \to eqeq\nu q(eqeq, \nu q \nu q) + X$
0	238	298	$p\bar{p} \to \nu q \nu q + X$

Table 2.3: Collider constraints on first-generation vector leptoquarks [20, 29].

Direct limits for second-generation leptoquarks				
β	Lower mass limit [GeV] for			Channel/Assumptions
	Scalars	Vector LQ coupling		
		Min. Vec.	Yang-Mills	
1	202	275	325	$p\bar{p} \to \mu q \mu q + X$
1/2	180	260	310	$p\bar{p} \to \mu q \nu q(\mu q \mu q; \nu q \nu q) + X$
0	113	171	222	$p\bar{p} \to \nu c \nu c + X$
	98	238	298	$p\bar{p} \to \nu q \nu q + X$

Table 2.4: Collider constraints on scalar and vector second-generation leptoquarks from direct searches in $p\bar{p}$ collisions [20, 29].

Direct limits for third-generation leptoquarks			
β	Lower mass limit [GeV] for		Channel/Assumptions
	Scalars	Vector LQ coupling	
		Min. Vec.	Yang-Mills	
1	99	170	225	$p\bar{p} \to \tau q \tau q + X$
0	148	199	250	$p\bar{p} \to \tau q \tau q + X$
	94	148 *	216	$p\bar{p} \to \nu b \nu b + X,\ b \to \mu + X$

Table 2.5: Collider constraints on scalar and vector third-generation leptoquarks from direct searches in $p\bar{p}$ collisions [20, 29].
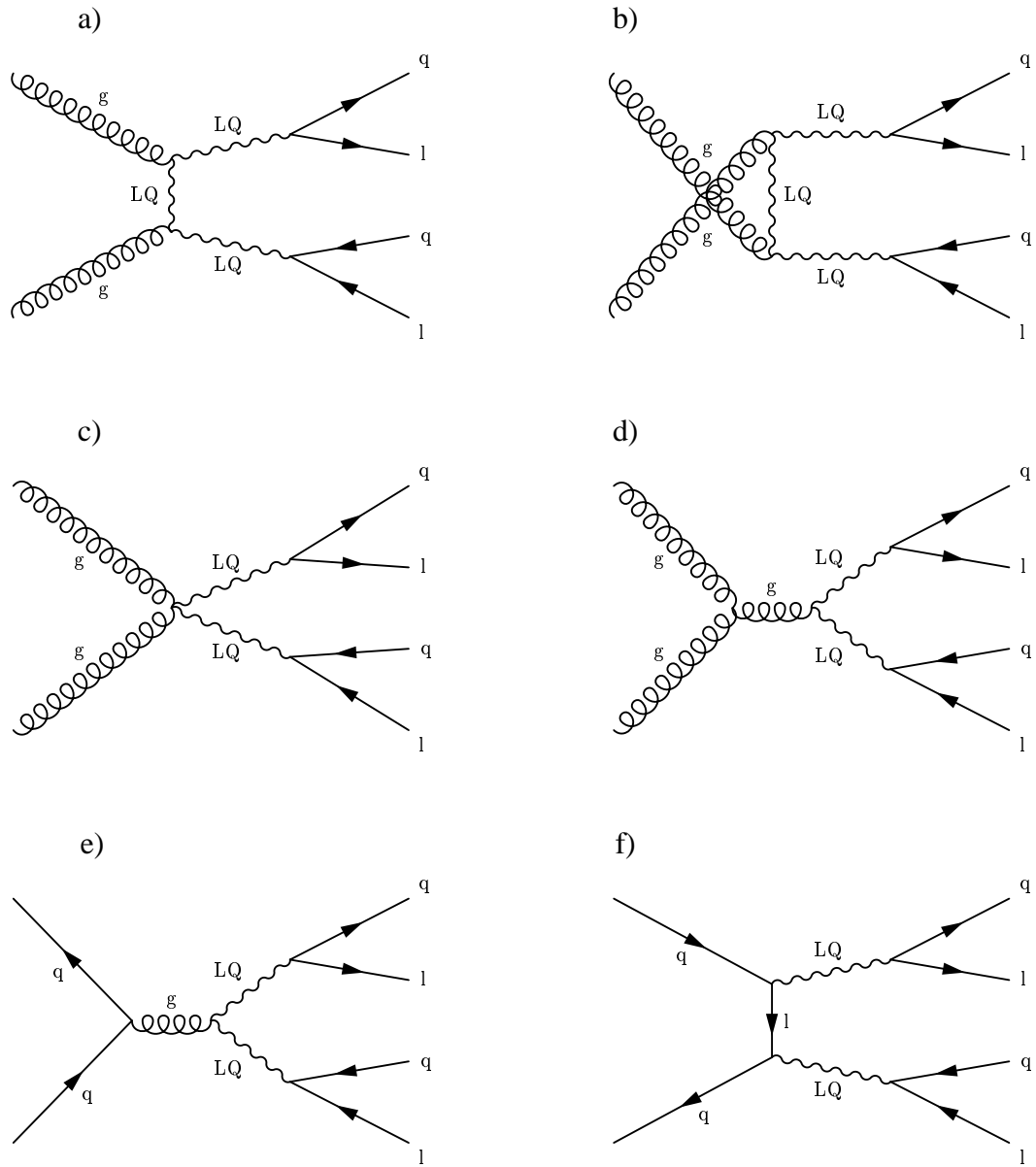
Figure 2.3: Lowest-order pair production and decay of leptoquarks in $p\bar{p}$ collisions: a)-d) gluon-gluon "fusion", e) $q\bar{q}$ annihilation, and f) pair-production through *LQ-l-q* vertices.
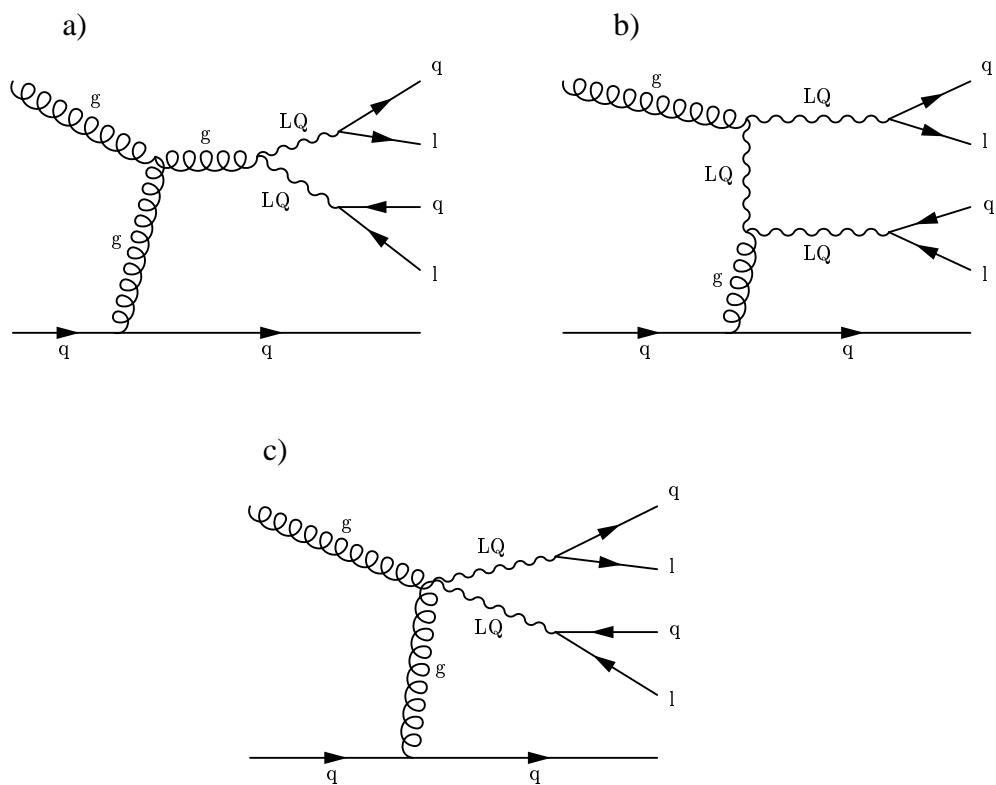
Figure 2.4: Feynman-diagrams for leptoquark production and decay in gluon-quark subprocesses, which are also included in the calculation of the cross-section for two scalar leptoquarks by [27].
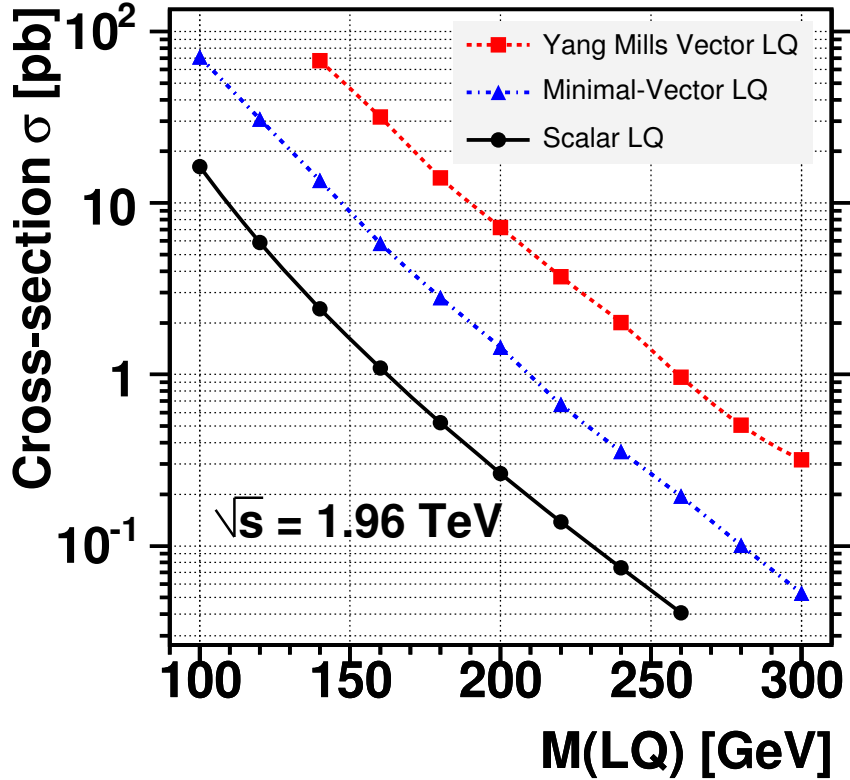
Figure 2.5:   Leptoquark pair-production cross-sections as a function of the leptoquark mass $M(LQ)$ in $p\bar{p}$ collisions at the centre-of-mass energy of $\sqrt{s} = 1.96\,\text{TeV}$. The black filled circles denote the next-to-leading order cross-section for scalar leptoquarks [27]. The red squares and the blue triangles show the cross-sections for spin-1 vector leptoquarks with *Yang-Mills* and *Minimal-Vector* couplings, respectively. The cross-sections for the vector leptoquarks, however, have been determined to leading order for the TeVatron Run I energy $\sqrt{s} = 1.8\,\text{TeV}$ [23] and then scaled by the factor $\sigma^S_{\text{NLO}}(1.96\,\text{TeV})/\sigma^S_{\text{NLO}}(1.8\,\text{TeV})$ obtained for scalar leptoquarks, in order to account for the increased collision energy at TeVatron Run II. Therefore, the curves for the vector-LQ cross-sections only show an estimate of what can be expected for $p\bar{p}$ collisions at the TeVatron Run II.
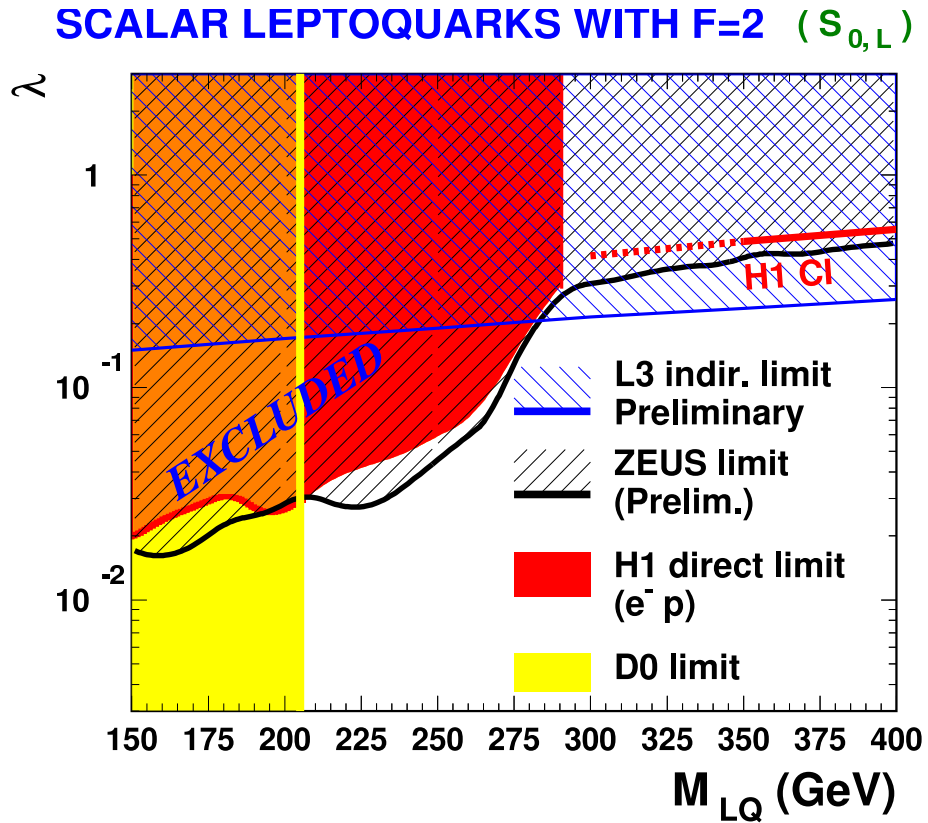
Figure 2.6: 95 % confidence level exclusion limits from direct searches for scalar first-generation leptoquarks. The figure shows the limits from $p\bar{p}$ collisions (DØ Run I) which are independent of the Yukawa coupling λ_{lq}, and from ep collisions (ZEUS and H1), as well as indirect limits from L3. [20, 29]

3 The TeVatron and the DØ Detector

The DØ detector is one of two collider experiments at the TeVatron accelerator at the *Fermi National Accelerator Laboratory* (*Fermilab*) which is located about 50 km west of Chicago, U.S.A. During the first running period of the TeVatron accelerator, between 1991 and 1995, the production of top-antitop ($t\bar{t}$) events was observed for the first time in proton-antiproton ($p\bar{p}$) collisions [30].

After a break of about five years, during which the accelerator and the experiments have been radically upgraded, the second phase of data taking, called Run II, started in 2001 and is planned to continue until at least 2008. Figure 3.1 shows an aerial view of the accelerator complex at Fermilab.

3.1 The TeVatron

Today, the TeVatron accelerator, operated at a centre-of-mass energy of $\sqrt{s} \approx 1.96\,\text{TeV}$, is the most energetic particle collider in the world. The main ring has a circumference of about 6 km. The accelerated protons collide with antiprotons, moving in the opposite direction in the synchrotron ring. The collisions take place in the two interaction regions of high luminosity which are surrounded by the CDF and DØ detectors.

3.1.1 The TeVatron Accelerator Complex

In general, collision experiments take place in three different steps: the initial production and injection of the particles, the following chain of successive acceleration and finally the collision itself. The TeVatron ring is the last part of a cascade of pre-accelerators at Fermilab as schematically illustrated in Figure 3.2. For a detailed description of the accelerator chain of the TeVatron, the reader is referred to [31, 32].

The proton beam begins as negatively charged hydrogen ions (H^-) which pass through a Cockcroft-Walton accelerator and then a linear accelerator of approximately 150 m length. Having reached energies of 400 MeV, the electrons are stripped off the hydrogen ions during their passage through a carbon fibre foil. The next level is the *Booster*

Figure 3.1: Aerial view of the TeVatron accelerator complex at Fermilab near Chicago. The foreground shows the *Main Injector* while the main TeVatron accelerator with its two experiments CDF and DØ is the ring of 6 km circumference, visible in the background.

synchrotron in which the protons ($H^+ \equiv p$) are accelerated to 8 GeV. The *Main Injector* delivers protons at an energy of 150 GeV to the TeVatron. Finally, the proton bunches are accelerated in the TeVatron ring to 0.98 TeV.

The protons from the *Main Injector* are also used to produce the antiprotons: Bunches of 120 GeV protons are aimed every 2.4 s at a fixed target made of nickel and copper. The collision energy is chosen such that the energy spectrum of the emerging antiprotons ($\bar{p}$) has its maximum at about 8 GeV. On average, around 50 000 protons are necessary to produce one antiproton in the required energy range. The TeVatron complex is designed in a way that new antiprotons can be produced in parallel to collisions taking place in the main TeVatron ring.

Using a complex system of lithium apertures and magnetic lenses, the antiprotons are
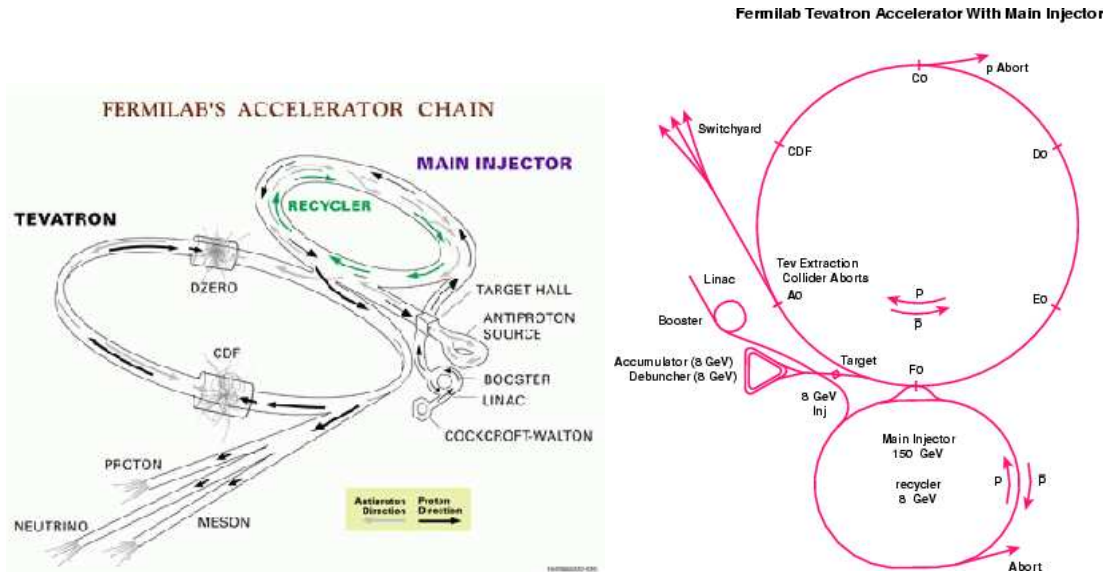
Figure 3.2: Schematic pictures of the TeVatron accelerator complex at Fermilab.

collected and guided into the *Debuncher* storage ring where they are focused into a coherent 8 GeV beam before being transferred into yet another storage ring, the *Accumulator*. This ring distributes the coherent $\bar{p}$ beam into bunches. Once a sufficient amount of particles is collected in the *Accumulator*, the bunches are transferred to the *Main Injector*, which delivers the antiprotons, after accelerating them to 150 GeV, to the main TeVatron ring where they move in the opposite direction to that of the protons.

The *Recycler* is located next to the *Main Injector* in the same tunnel. Originally, the *Recycler* was planned to be operational during the last phase of TeVatron data taking, Run IIb, starting in 2004/2005. The *Recycler* would allow the "recycling" of the antiprotons from the TeVatron after a collision cycle and the stock piling and cooling of high-intensity bunches of antiprotons. Before being transferred into the *Recycler*, the particles would be decelerated by the TeVatron to 150 GeV and then by the *Main Injector* to 8 GeV. The major technical obstacle to recycling, however, is the removal of the protons prior to the deceleration and the extraction of the antiprotons. This must be accomplished quickly (so as not to significantly add to the shot setup time[1]) and reliably, without risking TeVatron quenches[2] or significant radiation dose for the detectors. Since the difference in integrated

---

[1]The shot setup time is the time between two fillings, i.e. the time needed for the refill of the TeVatron with proton and antiproton bunches and their acceleration until new collisions can be recorded in the detectors.

[2]When part of the particle beam in the TeVatron gets lost and hits one of the magnets, the local heating of the superconducting magnet can result in the loss of superconductivity. This effect is called "quenching" of the magnet and leads to an immediate loss of the whole beam due to the breakdown of the magnet.

luminosity with and without recycling is estimated to only 10 %, based on new efficiency estimates and accounting for the current performance of the TeVatron, the plan to recycle antiprotons has been dropped or at least postponed. The ring will be used as an added stage for accumulating antiprotons form the antiproton source. [32]

Table 3.1 summarises the main characteristics of the TeVatron during the different Run II phases as compared to the performance of Run I. The longitudinal size of the proton and antiproton bunches has been decreased from 60 cm in Run I to about 37 cm in Run II [31].

	Run I	Run II					
Period (or starting date)	1992-96	current	12/04	2/05	9/05	1/07	12/07
Beam energy [GeV]	900	980					
Numbers of bunches $p \times \bar{p}$	6×6	36×36					
Number of protons / bunch ($\times 10^{11}$)	2.4	2.4					
Number of antiprotons / bunch ($\times 10^{10}$)	5.5	3.6	4.5	6.8	10.8	13.0	13.0
Average $\bar{p}$ production $\times 10^{10}$ / hour	6	12	15	22	36	40	40
Instantaneous luminosity ($\times 10^{32}\,\mathrm{cm}^2\mathrm{s}^{-1}$)	0.16	0.68	0.90	1.4	2.2	2.9	2.9
Integrated luminosity / week [pb^{-1}]	3.2	11	14	21	31	50	55

Table 3.1: Main (design) characteristics of the TeVatron operation during the different phases of data taking [32].

3.2 The DØ Detector

During Run I, approximately 100 pb^{-1} of $p\bar{p}$ collisions were recorded by each of the two experiments. The increase of luminosity at the upgraded TeVatron will enable the experiments to collect about 40 to 80 times the Run I integrated luminosity. Figure 3.3 shows the integrated luminosity as a function of time since the beginning of Run II. The figure draws attention to the difference in the amounts of integrated luminosity "delivered" to the DØ experiment by the TeVatron and the amount "recorded" by DØ, thus displaying the DØ operating efficiency, which has reached a level around 86 % during the last year.
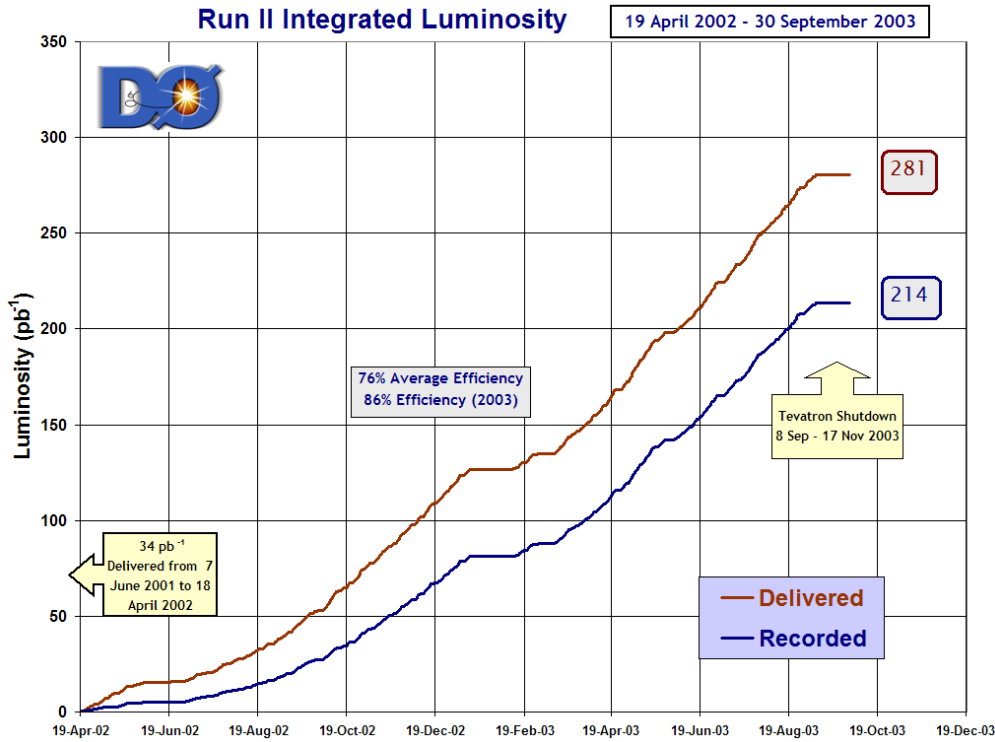
Figure 3.3: Integrated luminosity of $p\bar{p}$ collisions recorded with the DØ detector in Run II until autumn 2003.

The DØ detector was designed to study all the possible interactions taking place in highly energetic $p\bar{p}$ collisions with a geometrical acceptance of nearly the full solid angle of 4π. The detector's purpose is to measure the momenta and energies of particles emerging from the interaction point and to determine their identity, as well as to reconstruct secondary vertices.

A schematic view of the DØ detector, which is extensively described in [33], is shown in Figure 3.4. The apparatus consists of subsystems arranged in concentric cylinders or cuboids around the interaction point. Two end caps of muon detectors are stacked in rectangular layers, covering the two ends of the detector. Devices surrounding the beam pipe in the forward and backward regions measure small angle scattering phenomena.

The Cartesian coordinate frame of DØ is defined with its origin at the nominal interaction point and the z axis coinciding with the proton beam. The x axis aims at the centre of the TeVatron ring and the y axis points upward. The polar and azimuthal angles of the Cartesian frame are θ and ϕ, respectively. In this analysis, the polar direction of particles
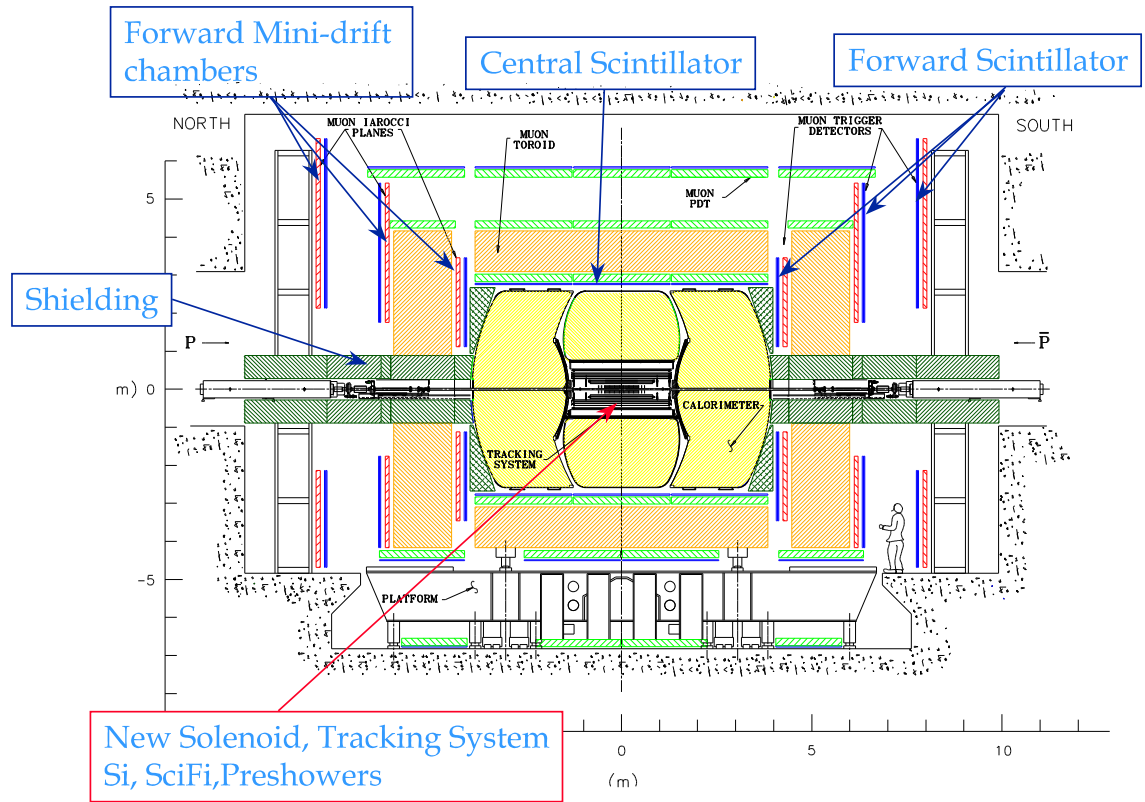
Figure 3.4: Schematic view of the DØ detector as seen from the side. The highlighted components are the subsystems which have been upgraded or rebuilt for Run II.

is often related to η, the pseudo-rapidity, which is defined as

$$\eta = -\ln\left(\tan\frac{\theta}{2}\right). \tag{3.1}$$

3.2.1   The Tracking System

Starting with the innermost apparatus, the silicon vertex detector (SMT) and the central fibre tracker (CFT) reconstruct the trajectories of charged particles from the $p\bar{p}$ collision (cf. Figure 3.5).

The association of a central track to an electromagnetic cluster in the calorimeter allows the distinction of electrons from photons. In the search for a pair of second-generation leptoquarks, which decay into two highly energetic muons and two quarks, the central tracking system is an essential component, since it allows the precise measurement of muon momenta.
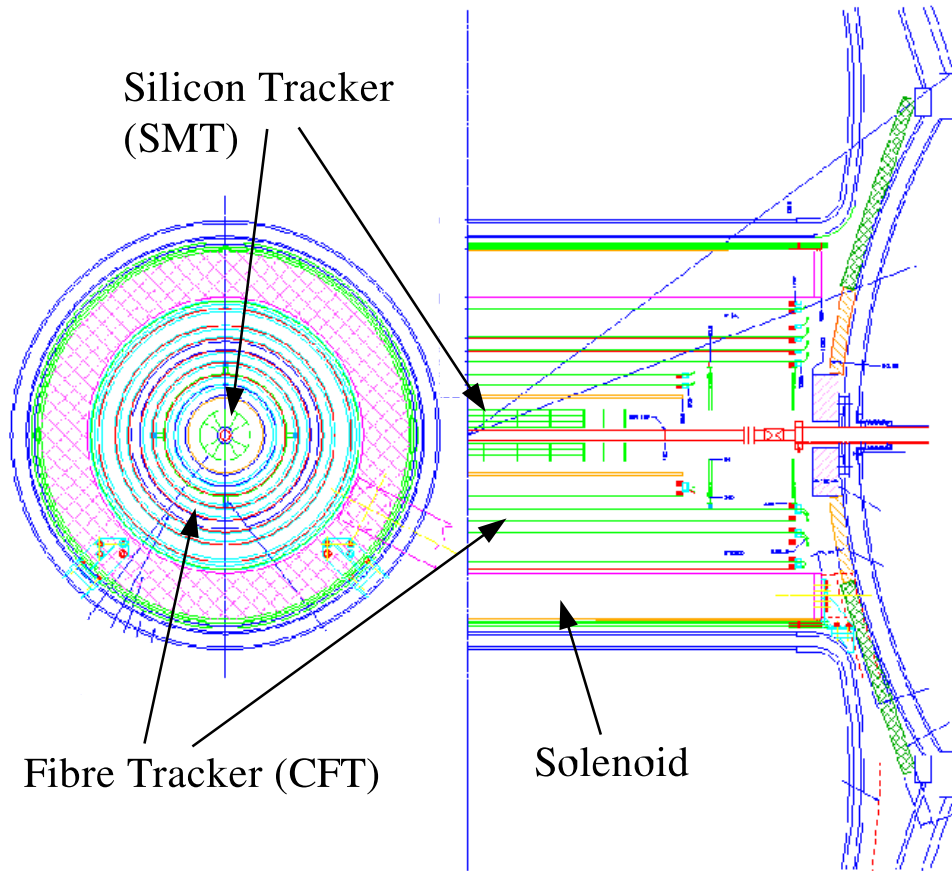
Figure 3.5: The DØ tracking system as seen from the beam direction (left) and from the side (right).

The whole tracking system, consisting of the SMT and the CFT is embedded in a solenoidal magnetic field of approximately 2 T.

The Vertex Detector

The innermost part of the tracking system is built of multiple layers of silicon detectors surrounding the beam pipe. A schematic view of the SMT is shown in Figure 3.6. For a detailed description of the SMT, the reader is referred to [34]. The SMT is made up of six, approximately cylindrical, layers of silicon detectors, covering $|\eta| < 1.7$ with respect to the nominal interaction point, and a structure of 16 silicon disks, perpendicular to the beam direction at varying values of z. The disks cover tracks with small angles in θ. The total coverage in η of the SMT is $|\eta| < 3$ (i.e. $6^o < \theta < 174^o$). The silicon vertex detector with around 790 000 read-out channels is designed to resist the radiation dose of about 1 Mrad, corresponding to an integrated luminosity of approximately $2\,\text{fb}^{-1}$.
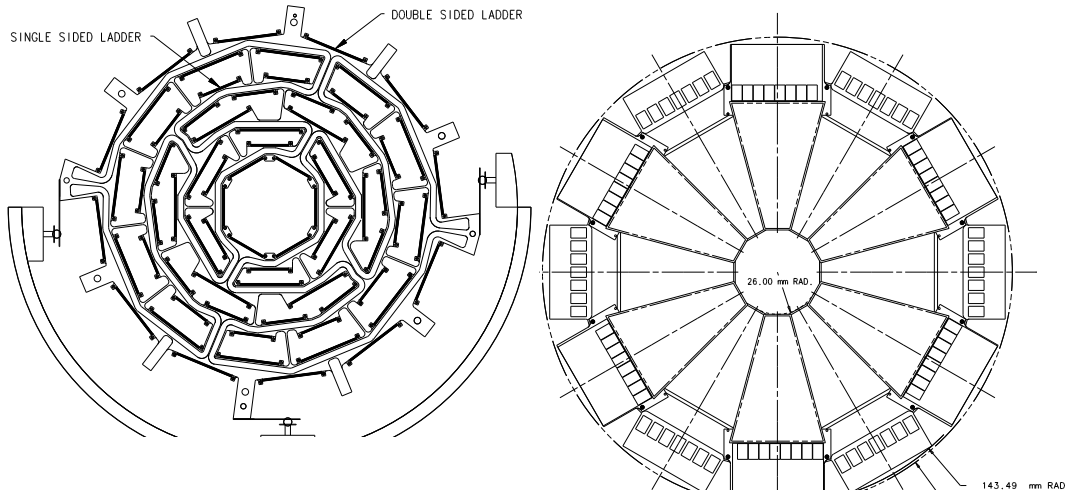
Figure 3.6: The Silicon vertex detector as seen from the direction of the beam pipe: the different layers of the SMT parallel to z (left) and one of the disks perpendicular to the beam direction (right).

The resolutions for the reconstruction of primary and secondary vertices perpendicular to the z axis range between $15\,\mu$m and $50\,\mu$m both for $t\bar{t}$ and $b\bar{b}$ events (depending on η). The z resolution for secondary vertices is around $80\,\mu m$ [36, 35].

The Central Fibre Tracking Detector

The central fibre tracker of the Run II DØ detector surrounds the silicon vertex detector in eight concentric cylinders and consists of $\approx 77\,000$ scintillating fibres ($\text{Ø}\approx 0.8\,$mm) at a distance from the z-axis of between $20\,$cm and $51\,$cm. Each layer is composed of fibres that are aligned parallel to the z direction and an additional sub-layer of fibres which are tilted by $\pm 2^{\text{o}}$ to provide stereo information of the tracks along z. The geometrical acceptance of the CFT reaches out into the forward direction up to $|\eta| \approx 1.5$.

For the read-out of the scintillating light, the fibres are optically connected to photo-detectors which yield a gain of more than $40\,000$ with an efficiency of about 0.7. The photo-detectors are cryogenically operated silicon avalanche devices which have a working temperature of about $10\,$K [37].

The central tracking system, i.e. the SMT and CFT together, are designed to provide a momentum resolution of $\Delta p_t / p_t^2 = 0.002\,\text{GeV}^{-1}$ for highly-energetic charged particles [35].

3.2.2   The Calorimeter

One of the strengths of the DØ detector is its calorimeter system due to its fine granularity and excellent coverage and uniformity. This detector delivers the signals for the jet reconstruction used in this analysis. Figure 3.7 shows a schematic view of the DØ calorimeter. A detailed description can be found in [33, 38].

END CALORIMETER
Outer Hadronic
(Coarse)
Middle Hadronic
(Fine & Coarse)

Inner Hadronic
(Fine & Coarse)

Electromagnetic

CENTRAL CALORIMETER
Electromagnetic
Fine Hadronic
Coarse Hadronic

1m
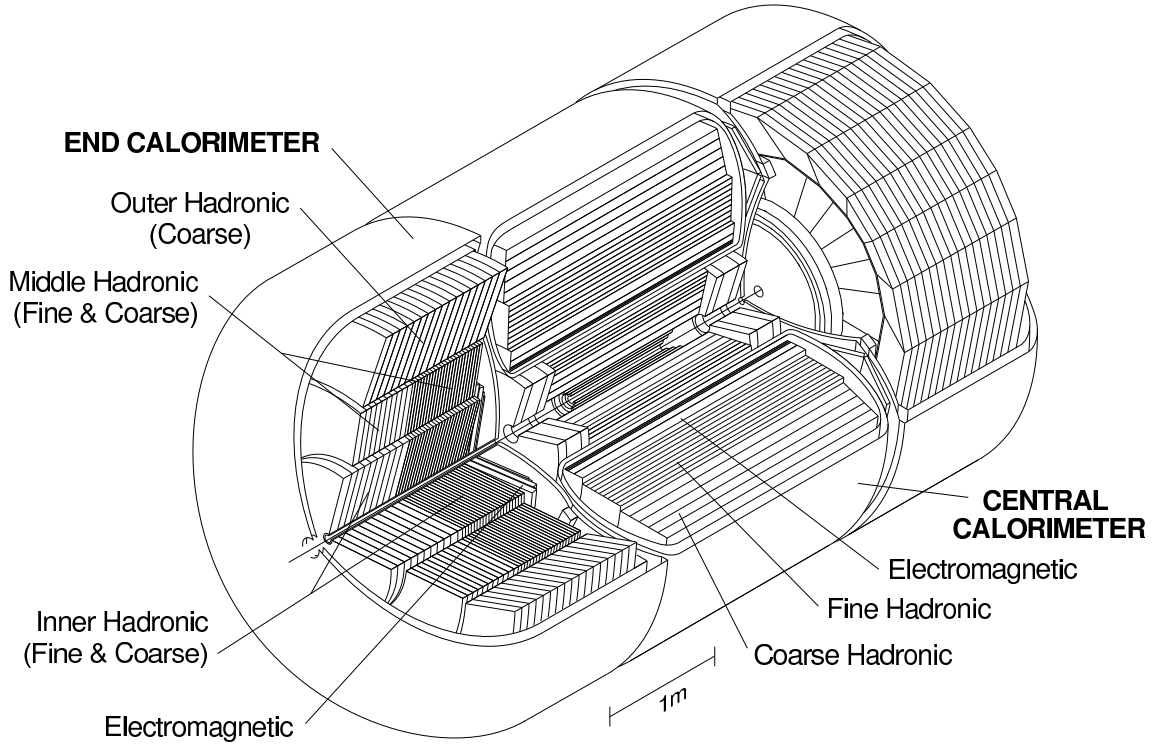
Figure 3.7: The DØ liquid-argon calorimeter.

The calorimeter is comprised of successive layers of passive uranium and active liquid argon. The central part of the calorimeter, located around the preshower detectors and the magnetic solenoid, occupies the space between 75 - 222 cm in radial direction from the centre of the beam pipe, and is approximately 236 cm long. Together with the forward calorimeter systems, a coverage of $|\eta| < 4.0$ is obtained. The identification of electrons/photons and jets is accomplished by a detailed three-dimensional image of the shower shape both in r and η-ϕ of the cell signals.

The cell structure of the calorimeter with its cell granularity of about 0.1×0.1 in η and ϕ provides the angular resolution for the centre of electro-magnetic showers from electrons of $\Delta\phi \times \Delta\eta \approx 0.05 \times 0.05$ [38].

The energy resolution σ_E/E for highly energetic electrons in $Z \to e^+e^-$ events ranges between $(3.47 \pm 0.03)\%$ and $(2.38 \pm 0.03)\%$ for the central and the forward part of the calorimeter, respectively [39]. The definition of jets and their detection efficiency will be descussed in a later chapter (cf. section 6.3.2).

Intercryostat Detector

The *Intercryostat Detector* (ICD) improves the energy resolution in the intermediate regions of the calorimeters where the energy measurement is degraded due to read-out cells without absorber material. The active material of the ICD is designed to allow normal operation when placed within the magnetic field: 384 scintillator tiles distributed over 16 layers of the region between $|\eta| \approx 1.1$ and 1.4 yield a segmentation of 0.1 by 0.1 in η and ϕ. The signal is carried to photo-multipliers (PMT) through wave-length shifting and clear fibres, such that about ten photo-electrons can be detected per single m.i.p.[3]. LED systems are used to calibrate the PMTs [38].

The Preshower Detectors

The central and forward preshower detectors (CPS and FPS, respectively), which are mounted to the outside of the magnetic solenoid, serve to enhance the electron and photon identification by providing an additional calorimetric measurement. Their spatial resolution of 1-2 mm transverse to the particle direction helps to distinguish electron, photon and pion showers and even allows a precise extrapolation of electro-magnetic showers back to the interaction region in order to identify displaced photons [40]. The CPS and the FPS together cover a region up to $|\eta| \approx 2.5$. The preshower detectors are made of flat lead absorbers and multiple layers of scintillator strips. The read-out is similar to that of the central fibre tracker [38].

3.2.3   The Muon System

The muon system provides the third important ingredient to the search for leptoquarks of the second generation, since it is not only essential for the identification of the muons, but is used also used as the main ingredient for triggering the candidate events. Figure 3.4 shows the layout of the muon system within the DØ detector, Figure 3.8 shows the section of the end cap of the muon system as seen from the side. The reader is referred to [41] for a detailed description of the muon system.

---

[3]m.i.p. $\equiv$ minimum ionising particle.
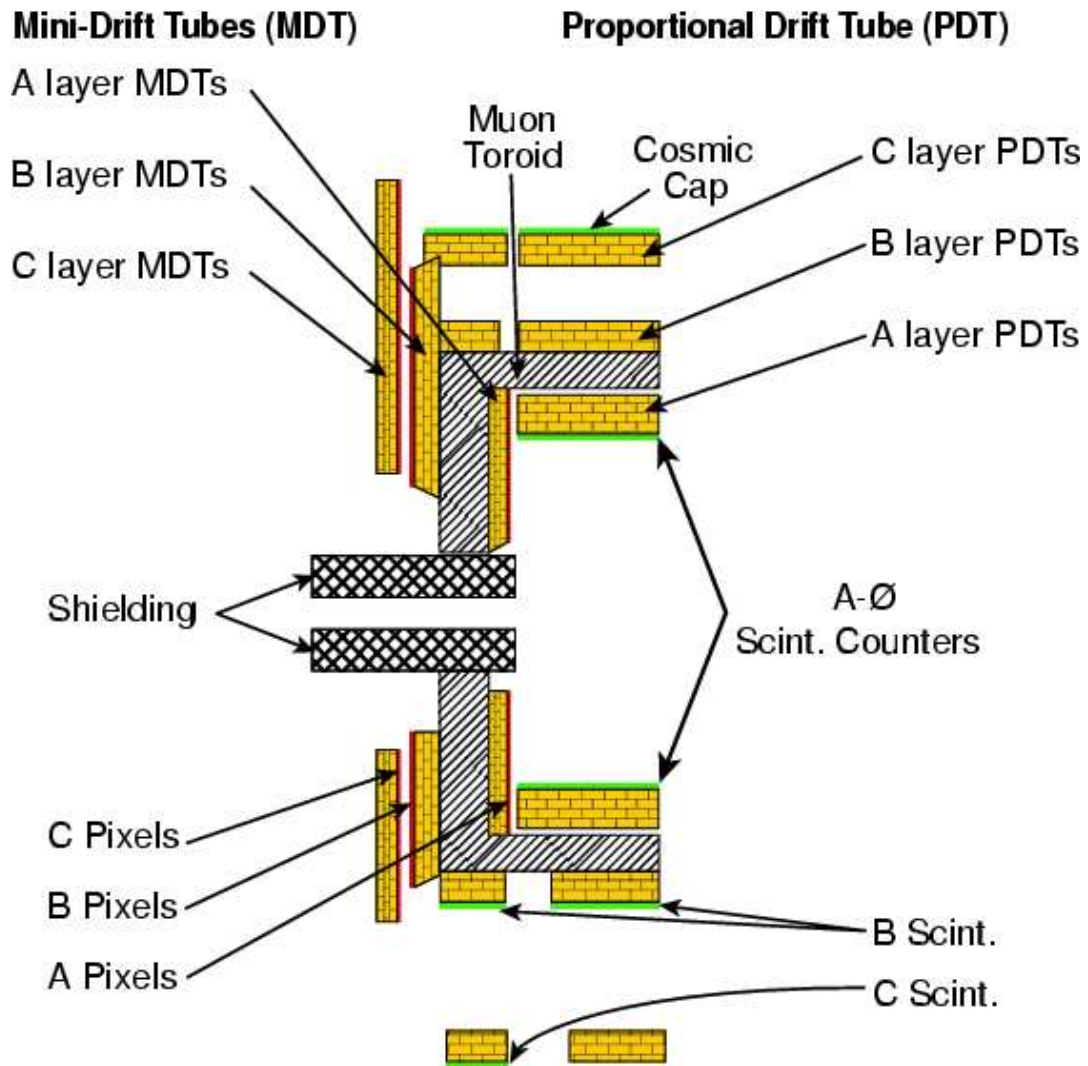
Figure 3.8: Schematic view of the DØ muon system as seen from the side.

The Central Muon Detectors

The muon system surrounds all the other components of the DØ detector in a cuboidal shape of three multi-layers. The 94 proportional-drift chambers of the central muon system (covering $|\eta| < 1$) were already used during Run I. The innermost layer (layer A) is located between the calorimeter cryostat and the 2 T muon-toroid magnet and consists of four planes (decks) of drift tubes on the top and the sides of the detector and three planes at the bottom due to space constraints. The B and the C layer, outside the iron toroid, each have three layers of drift tubes.

The cells are rectangular aluminium tubes with dimensions 5.7 cm by 10 cm and provide a drift-distance resolution of approximately 1 mm. The tubes with their anode wires are oriented parallel to the magnetic field of the toroid (i.e. orthogonal to the beam direction).

In addition to the drift tubes, layers of scintillators, called *Cosmic Cap*, on the top and the upper sides of the central muon detector were used in Run I to help reject cosmic rays. The coverage was completed for Run II and additional counters were installed at the bottom of the detector. A new layer of scintillator counters, the $A\phi$-counters, was added between the calorimeter and the A-layer drift chambers. These counters with their ϕ segmentation of 4.5° are used for muon triggering and the rejection of out-of-time scattered particles and cosmic muons. Furthermore, these counters improve the ϕ determination of the muons [41].

The Forward Muon Detectors

The three layers of the muon-system end caps have been completely rebuilt for Run II. They are made up of mini-drift tubes (MDT) and pixel scintillators. Analogously to the central muon system, the innermost layer (A) is placed in front of the magnetic muon toroid, while the layers B and C are located behind the magnetic iron. See Figures 3.8 to 3.10 for the layout of the forward muon system.

The A-layer of the forward muon system is located before the forward muon toroid which provides a magnetic field of approximately 1.9 T. This layer consists of four planes (decks) of mini-drift tubes with a cross-section of $1 \, \text{cm} \times 1 \, \text{cm}$ which are arranged octant-wise parallel to either the x or y axis (cf. Figure 3.9). Each octant has for each plane between 300 and 400 tubes, varying from layer to layer. The tube length in each octant increases with increasing distance from the beam pipe. The drift chambers of layers B and C, located after the muon toroid, are constructed similarly, but with only three planes of drift tubes per layer. The drift-distance resolution of the MDTs is about 0.7 mm [41, 42].

In addition to the drift tubes, each of the three layers is covered with a pixel array of scintillation counters. These counters, which cover approximately the same area as
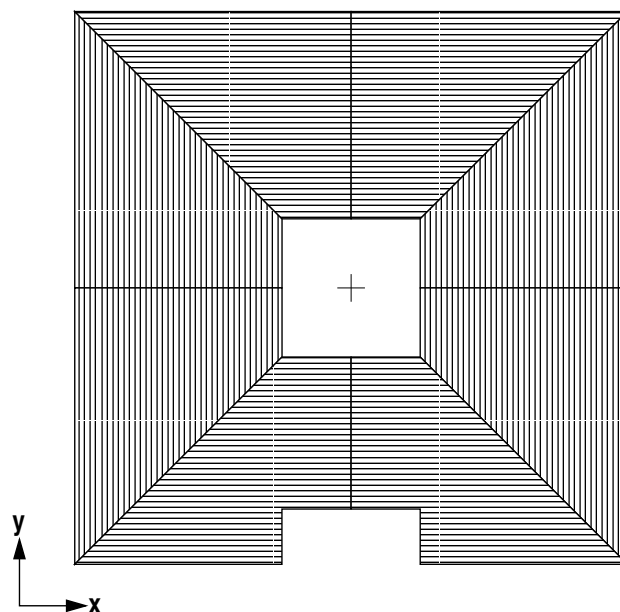
Figure 3.9: Schematic picture of a layer of the mini-drift tubes. The layers B and C look similar to layer A, except that they are bigger and composed of more drift tubes in order to cover the same range $1 < |\eta| < 2$ at a farther distance z from the interaction point.
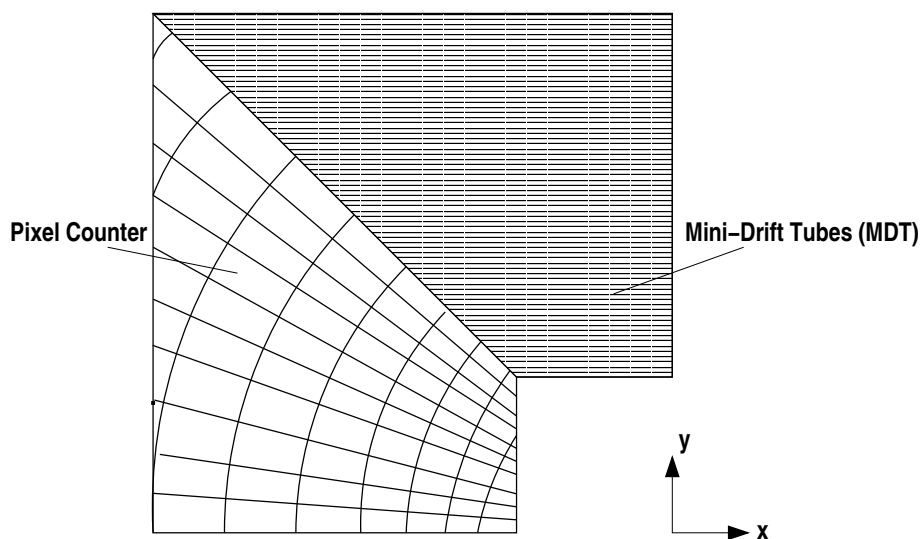
Figure 3.10: Schematic drawing of one quadrant of one layer of the forward-muon spectrometer. This picture shows the layout of the scintillation counters (pixels) for one octant as well as the orientation of the mini-drift tubes in the neighbouring octant.

the MDTs, are used for triggering and cosmic vetoes. Furthermore, they improve the direction measurement along the drift wires. The typical size of a pixel is $20\,\text{cm} \times 30\,\text{cm}$. The size of the Bicron 404A scintillators varies such that the segmentation in η and ϕ of each pixel is about $0.1 \times 4.5^{\text{o}}$, respectively [41, 42].

Performance of the Muon System

The momentum resolution of the muon system has been studied using reconstructed muons for which a central track from the SMT and CFT was associated. The momentum resolution for muons as measured by the muon system, $\sigma(p_t)/p_t$, varies between 0.1 for low-momentum muons and 0.5 for muons with $p_t > 50\,\text{GeV}$ [43].

The momentum resolution of the central tracking system is better than the measurement from the muon system only. The resolution for muons with a transverse momentum of $100\,\text{GeV}$ is approximately $15\,\%$ when a matching central track is identified [41].
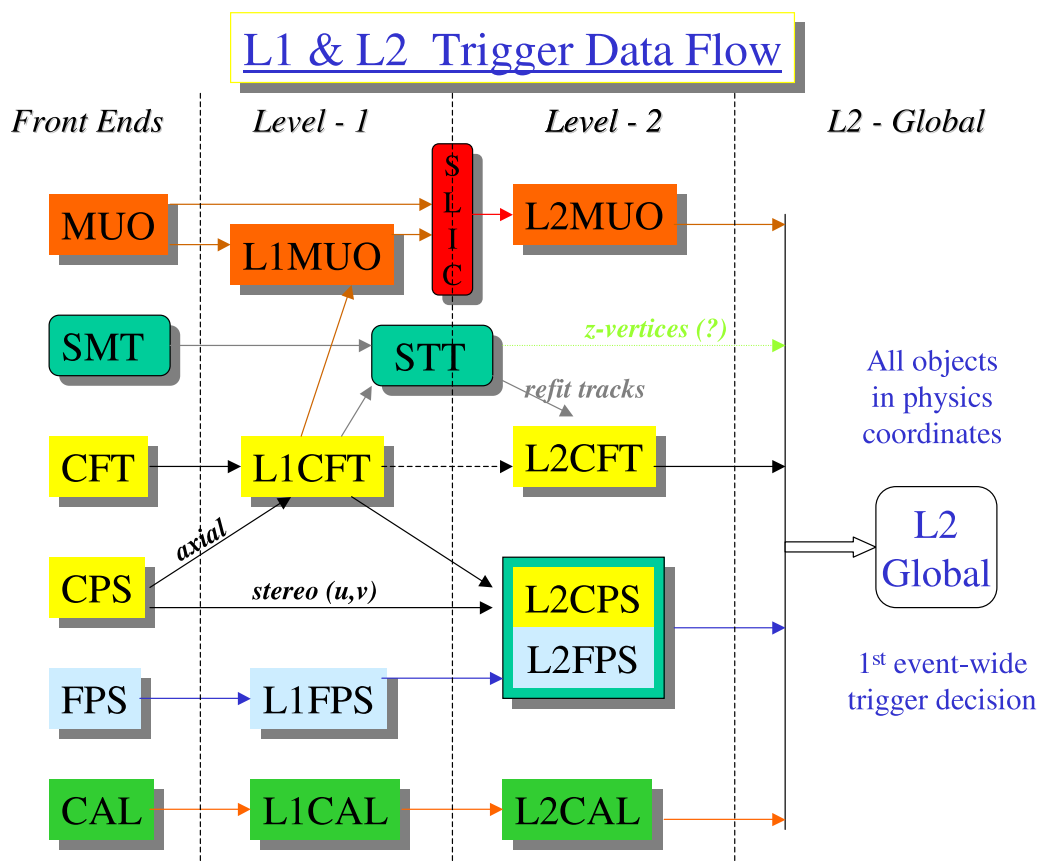
4 The Level-2 Trigger System of the Forward Muon Spectrometer

The trigger system of the DØ experiment consists of three successive levels of rejection. The second level, the Level-2 trigger, is the first which forms trigger decisions based on physics objects from *all* detector systems. This trigger level is designed to reduce the incoming event rate of up to 10 kHz by a factor of ten, before a further rejection in the third trigger level takes place in order to reduce the event rate to a level that can be recorded [44].

Figure 4.1 shows a schematic picture of the trigger structure and the data flow of the first two trigger levels. Herein, the left column represents the different detector systems and their read-out electronics: the muon system (MUO) with the drift tubes and scintillation counters, the silicon tracker (SMT), the central fibre tracker (CFT), the central and forward preshower detectors (CPS & FPS) and the calorimeter (CAL). The second (third) column of boxes shows the separate Level-1 (Level-2 pre-processor) systems, while the thin arrows indicate the data flow. As can be seen from these arrows, the muon-related part of the Level-2 trigger system (L2-Muon) is somewhat special: it not only receives the L1-Muon objects, it also acquires all of the hit information from all muon front-ends, and thus is the most complex L2 system with more than 150 different input channels. In fact, L2-Muon has a whole additional trigger level on its own, analogously called the "Level-1.5" trigger, which performs the muon-track finding in a parallelised fashion on 80 identical processors. The last column of Figure 4.1 with only one box represents the global-L2 system. This system is responsible for collecting all the different objects—i.e. muons, electrons/photons, jets, central tracks, missing-E_t—from the separate and independent L2 pre-processors before shaping the trigger decision at Level 2.

In the Level-2 trigger, muon tracks are reconstructed using the binary hit information of the drift tubes and the scintillator pixels to estimate the momenta and the directions of the muons. In order to be able to cope with the amount of hits to be processed in the available time budget of $\approx 30\,\mu s$ on average, the track finding is performed on fast pre-processors (25 independent DSPs) for different layers and regions of the detector in parallel. The properties of the muon segments in each of the different sectors/layers is then

Figure 4.1: Scheme of the Level-1 and Level-2 trigger system [45] with its data flow. See text for more details.

passed on to an ALPHA-processor[1] to be combined to L2-Muon objects with momentum, timing and direction information.

In early 2002, the forward muon algorithms were the first L2 algorithms to be used for online triggering. Since then, the performance of the algorithms has been studied in detail and their efficiencies have been optimised to run at nearly 100 %. Many DØ physics analyses, basically every analysis relying on muon triggers, is dependent on the Level-2 muon trigger system.

This chapter describes the layout of the L2-Muon system. The hardware will be introduced and the algorithms used in L2 to identify muons and to measure their properties will be discussed in detail.

4.1   The Hardware of the Level-2 Muon Trigger

The digitised and packed hit information from the different muon detectors (drift tubes and scintillator counters, and also the L1-muon objects) are sent to the L2-Muon system.

Analog Cable Input Converters (CICs) are used to convert and restore the inputs from the detector electronics (each on a separate coaxial cable) into proper physical formats after the signals have travelled for nearly 100 m to reach L2-Muon, located outside the DØ collision hall. After the signals are reshaped and reformatted by the CICs, the 150 different channels are distributed using the 160 MBit/s serial Hotlink [46] to the SLIC boards (SLIC = Second Level Input Computer). Since some SLICs depend on the same inputs, specially designed Serial Fanout boards (SFO) are installed for these channels before the SLIC in order to duplicate the Hotlink [46] signals.

The tracking of the muons in the Level-2 system takes place in the first L2-Muon sub-level on eighty 160 MHz *Texas Instruments* DSPs which are located in groups of five on the SLIC boards. There are eleven SLIC boards for the central muon system and five for the forward system. Both systems, for the forward and central regions, require each 1 SLIC for the translation of Level-1 muons. The remaining 10 (for central) and 4 (for forward) SLICS are responsible for the muon-track finding in Level 2. Each of the first four DSPs on each of the SLIC boards, the so-called worker-DSPs, is responsible for the track finding or the translation of Level-1 signals, while the fifth DSP chip administrates the worker-DSPs, collects the identified muon-objects and sends them to the next L2-Muon sub-level. This administrator-DSP is also in charge of error handling and collecting/sending the monitoring information for the whole SLIC, including timing, error

---

[1]In fact, during the shutdown period in autumn 2003, all ALPHA processors of the whole Level-2 trigger system have been successively replaced by the next generation of processors, the faster BETA processors. In order to avoid confusion, henceforth the processors are generically given the name ALPHA.

counting and others. The algorithms, the data routing within the SLIC board, the monitoring and the error handling are all implemented in the C programming language (compiled by specially designated DSP compilers).

Although they are fast, a noteworthy property of the DSP chips used at DØ is, that their performance is limited to integer manipulations only: this means, that the DSPs receive the inputs (i.e. the muon hits and their parameters) as integers, that all the algorithms on the DSPs can only perform integer manipulations and the output needs to be encoded as integers. Unfortunately, relatively little memory for the whole executable is available on the chip. The memory available on each of the processors is 64 kB for the executable and 64 kB additional memory for the storage of variables, structures and arrays. An additional 128 kB off-chip memory can be used for look-up tables used by the algorithms. These look-up tables are arrays containing the necessary information of valid muon tracks and their properties encoded as integers. The limited memory for the program constrains the algorithm code not only to be fast in order to cope with the high luminosity but also to be sufficiently compact.

The SLIC output, i.e. basically the identified muon segments, is sent via yet another serial Hotlink [46] to a high-bandwidth 320 MB/s 128-bit bus, the so-called Magic Bus transceiver (MBT). The MBT is connected to the next level of L2-Muon preprocessing, the ALPHA processors, one ALPHA board for the forward, one for the central muon system.

The global-L2 processor, on yet another ALPHA board, receives the further processed and compressed data from the L2-Muon ALPHA systems and forms the Level-2 trigger decisions.

4.2   The Tracking Algorithms

The algorithms for identifying and measuring the muons in Level-2 are a rather complex system of both parallel and successively running algorithms on all the three systems: the SLICS, the L2-Muon ALPHAs and finally the L2-Global ALPHA. This section describes the different steps of muon identification in all of the three sub-levels of Level-2. While the rough structure of the track finding in the central and forward detectors is similar, the muon detectors are different. This difference is almost only visible in the first sub-level, the SLIC level, of the track finding, for which the format of the inputs and the algorithms are quite special. The output format of the SLICS, the identified muon segments in the corresponding detector regions, on the other hand, is the same, such that the structure of the forward and central algorithms on the L2-Muon ALPHAs is essentially the same. After a brief introduction of the software framework which is used to efficiently structure

the DSP software for both, the online triggering as well as the simulation of the SLIC-level, this chapter mainly focuses on the muon identification for the forward system. For a detailed description of the central L2-Muon algorithms, the reader is referred to [47].

4.2.1 The SLIC Software Framework

In order to coordinate all the different algorithms for each of the 16 SLICs with their 80 processors in total, the whole SLIC/DSP software is located in one single software package[2].

All the algorithms and all the different unpacking routines for the different inputs are located here. The source code for the algorithms as well as the unpacking routines is identical for the DSPs as well as for the simulation of the trigger offline. The setup of each of the 16 SLICs is controlled by scripts (so-called RCP files, RCP $\equiv$ Run Control Parameter) which setup the whole system through the following parameters:

- An identification number unique for each SLIC.

- The SLIC board's physical position within the L2-Muon crate.

- For each of it's inputs, the SLIC is told:

    - the input channel (to which of the twelve physical input channels of the SLIC the cable is connected),

    - the nature of the input (e.g. forward muon scintillator or central drift tubes),

    - the *module-ID*, an identifier, unique to each of the approximately 150 inputs to the L2-Muon system.

Furthermore, this script contains for each of the SLIC's four worker-DSP chips the following information:

- Which physical region of the detector is being processed,

- which input channels of the SLIC should this DSP "listen" to and which unpacking routine should be linked and called for each individual input,

- which algorithm should be run on each DSP,

- which look-up table should be loaded into the off-chip memory of the DSP during the booting process.

---

[2]The name of this DØ-software package is `l2slic`. Instructions on how is is used in the simulation are posted at
`http://www.nevis.columbia.edu/~christos/Research_dir/D0_files/l2mu_sim_instruct.html`.

This detailed information is used to include only those routines, which are necessary, in the executable for a specific DSP, i.e. the DSP for the forward A-layer in the upper left octant of the north side of the detector only has knowledge of the forward layer-A algorithm and those unpacking routines needed for the inputs belonging to this detector region.

4.2.2 Track Finding in the Forward System

The DSP algorithms (SLIC level) are characterised by the detector region and the input or sub-detector plane and make use of the detector symmetry to run the same basic code. The output of the SLIC level are A-layer stubs (i.e. segments formed of multiple hits in the scintillator counters and drift tubes of only the innermost layer of muon detectors), BC-layer stubs, and L1-stubs. The matching of A-layer with the BC-layer stubs of one and the same muon is not done in this sub-level of L2-Muon, but in the ALPHA-processing stage which will be described in section 4.2.4.

For the forward detectors, there are three different algorithms running on the worker-DSPs located on the five SLIC boards:

- The first kind of algorithm receives the output from the Level-1 muon system and translates it into the common output to be used on the ALPHAs. All the four algorithms of this kind, one for each quarter of the detector, are run on the four worker-DSPs of the same SLIC board. Although this algorithm is written and tested, the commissioning is not fully accomplished and therefore, these algorithms have yet to run online.

- Another kind of algorithm runs on the first two of the four remaining SLIC boards of the forward system. It is responsible for finding segments of muon hits in the first layer (layer A) of the muon system. Each of these eight DSPs with identical A-layer algorithm only searches for muon traces in a quadrant of either the north or south part of the DØ end-cap.

- On the second two worker-DSPs of each of the four forward-SLICs, the third type of algorithm searches for muon segments in the second and third layer (layers B and C) of the forward muon system. These BC-layer algorithms already match, if possible, the muon traces from the two layers B and C before the segments are sent out.

- The last algorithm to run on the fifth DSP of each SLIC contains the administrator code. This algorithm is responsible for the error handling and counting. It also collects the timing needed for the different sub-processes of the SLIC system and it collects the segments found by its worker-DSPs and sends them out to the next

level. The administrator algorithms are identical for all SLICs in the forward and central system of Level-2.

While the algorithms themselves running on the independent DSPs may be identical, the difference comes from the content of the look-up tables, stored in the on-board memory of each DSP and used for the segment finding and the look-up of the segment properties, i.e. the direction and the quality of the object found. The creation of these look-up tables is done offline and will be described in section 4.2.3.

This section now describes the two main types of forward algorithms, the A-layer and the BC-layer algorithms, in detail.

The BC-Layer Algorithm

All eight DSPs responsible for finding tracks in the layers B and C of one of the four quadrants of the two sides of the forward muon system basically run the same program. The software is written such, that the DSP calls the algorithm code, once all the hits of one event are received and unpacked into integer arrays of structures which successively store all the drift tube and scintillator hits of the detector region of interest. When the algorithm has completed the segment finding and when the segments are sent on to the administrator-DSP, the DSP resets all hits and the unpacker routines are called again, and the DSP is ready to process the hits of the following event.

A detailed description of the algorithm for the forward BC-layers can be found in the appendix A.1. In brief, the algorithm looks, after having checked and unpacked the incoming drift tube (MDT) and scintillator hits (pixels), for valid combinations of hits that could originate from a muon transversing the two muon layers on its way from the interaction point. The valid hit patterns are studied and optimised using a full Monte-Carlo simulation of single-muon events.

The muon objects (stubs) found by this forward algorithm are classified with respect to the number of hits and the quality of the matching between the two layers B and C: A stub found by a DSP in the forward muon system for the detector layers B and C is classified according to Table 4.1 [48]. Stubs consisting of hits in only one of the two layers get the lowest quality, while stubs consisting of drift tube hits in both layer B and C get highest quality if an additional pixel hit could be associated.

For all stubs found (up to a maximum of two stubs per octant and event), the following properties are sent out to the next sub-level of L2-Muon:

- the timing from the best matching pixel hit in layer B,

- the timing from the best matching pixel hit in layer C,

Quality	Requirement
BCQual = 1	$N_{\text{plane}}^{\text{B}-\text{MDT}} \geq 2$ or $N_{\text{plane}}^{\text{C}-\text{MDT}} \geq 2$ (stub consists only of hits in one of the two layers)
BCQual = 2	$N_{\text{plane}}^{\text{B}-\text{MDT}} \geq 2$ and $N_{\text{plane}}^{\text{C}-\text{MDT}} \geq 2$ (matching MDT hits in at least 2 different planes in each layer B and C)
BCQual = 3	$N_{\text{plane}}^{\text{B}-\text{MDT}} \geq 2$ and $N_{\text{plane}}^{\text{C}-\text{MDT}} \geq 2$ and ≥ 1 associated pixel hit in one or more of the two layers.

Table 4.1: Quality assignment of BC-forward stubs. $N_{\text{plane}}^{\text{B}-\text{MDT}}$ ($N_{\text{plane}}^{\text{C}-\text{MDT}}$) is the number of planes in layer B (C) contributing an MDT-hit to the stub.

- the angle ϕ, looked up from the best matching pixel of the two layers B and C (if no pixel hit could be associated with a valid drift-tube sequence, the azimuthal coordinate ϕ is set to the middle of the corresponding octant),

- the pseudo-rapidity η (w.r.t. the nominal interaction point and the beam pipe), determined from straight projection of the BC-stub back into the middle of the magnetic toroid between the layers A and B (see Figure 4.2),

- the *deflection* of the BC-line from the straight line as defined by η,

- and the quality assignment of the stub as described in Table 4.1.

Using the determined η and the *deflection*, the sign of the charge and the momentum of the muon can later be estimated.

Since the ALPHA algorithm simply matches the first BC-stub to the first A-stub which line up in a given geometric window, the algorithms are designed such that they send out their stubs in order of decreasing quality.

The A-Layer Algorithm

As opposed to the BC-layer algorithm, the algorithm for finding muon stubs in the inner-most muon detectors of the forward system is not responsible for matching objects from one layer to another. On the other hand, layer A has one additional plane of MDT tubes and the occupancy of the A-layer is somewhat higher than in layers B and C which are further shielded by the magnetic toroid.

A-stubs with hits in at least three of the four MDT planes are found by comparing the hits with valid hit patterns stored in the look-up tables. Since the look-up tables are produced through a full Monte-Carlo simulation, only stubs which are consistent with coming from the interaction region are selected. Stubs with associated hits in only two of the MDT planes are only accepted if the two planes lacking a matching hit do not contain any hits at all in the vicinity of the considered 2-hit stub. This veto is designed to reduce the background from clusters of noise hits and from stubs not pointing toward the interaction region. In addition, such a 2-hit stub must have a matching hit in the scintillator detector of layer A in order to be considered valid.

The muon objects (stubs) found by this forward algorithm are classified with respect to the number of associated hits: A stub found by a DSP in the forward muon system for the detector layer A is classified according to Table 4.2 [48]. Stubs consisting of MDT hits in only two of the four planes get the lowest quality as long as a scintillator hit is additionally matched. Medium quality is reserved for A-stubs with at least three MDT hits. A tight A-stub is a medium stub with a matching scintillator hit in layer A.

Quality	Requirement
AQual = 1	$N_{\text{plane}}^{\text{A−MDT}} = 2 \, and \, N_{\text{Pixel}} \geq 1$
AQual = 2	$N_{\text{plane}}^{\text{A−MDT}} \geq 3$
AQual = 3	$N_{\text{plane}}^{\text{A−MDT}} \geq 3$ and $N_{\text{Pixel}} \geq 1$

Table 4.2: Quality assignment of A-forward stubs.

4.2.3 The Look-up Tables

The look-up tables for the forward DSP algorithms are simple `ASCII` files filled with integer numbers (of size 4 bytes, 2 bytes or 1 byte) corresponding to the huge arrays needed for the track finding and the determination of the stub parameters. Since there is only limited space in the off-chip memory available for the look-up table (128 kB maximum), not every single combination of e.g. three MDT hits in a layer of the B+C system (i.e. about $2 \, \text{layers} \times 350^3$ tubes combinations) can be stored in the look-up table. Therefore, the requirements (A.1) and (A.2) (see appendix A.1) are used to largely decrease the number of hit combinations stored in the look-up table for the forward-BC algorithm. The values stored (e.g. η, ϕ for a given combination or the projection into the other layer) are encoded into integers (often with only 1 byte of memory). The lookup tables are loaded into the off-chip memory of the DSPs during the boot process.

The look-up tables for the forward-DSP algorithms are produced from a full Monte-Carlo simulation of the DØ detector using single-muon events with the following properties:

- $0.8 < |\eta| < 2.2$,

- $1 \, \text{GeV} < p_T < 12 \, \text{GeV}$,

- spread of the "interaction point" along the direction of the beam pipe as expected for DØ collisions: $\sigma_z(\text{I.P.}) = 30 \, \text{cm}$.

In a specially designated software package, three million simulated single-muon events are passed through a full simulation of the DØ detector which incorporates the latest knowledge of the geometry of the muon system. In order to have all MDT tubes more or less evenly illuminated, the distribution of single muon events is not flat in η but follows the second-order polynomial $|\eta_\mu| = \eta_{min} + (\eta_{max} - \eta_{min} + 0.5) \cdot rnd - 0.5 \cdot rnd^2$, where *rnd* are uniform random numbers between 0 and 1, $\eta_{min} = 0.8$, and $\eta_{max} = 2.2$.

For the BC-algorithms of the forward muon system, all single muon events enter the determination of the look-up tables if at least two out of the three planes of MDT tubes in each layer of the considered octant have at least one hit.

For all events which enter the look-up table for a specific octant, the "centre-of-gravity" of the hit pattern within each layer B and C is stored. This "centre-of-gravity" value is the identifier of the tube in the middle plane of each layer, which corresponds best to the projection of all hits into the middle layer as seen from a muon coming from the nominal interaction point. Then, for every two and three-hit combination of layer B (i.e. 1 hit per plane, while only one out of the three layers is allowed not to have a hit), the "centre-of-gravity" position of the corresponding hit pattern in layer C is recorded and vice versa. When all events are processed, the table-maker algorithm determines,

for each hit combination, the range of all possible hit patterns in the other layer. The average of these two numbers is then stored in the look-up table as the most likely projection of a given combination into the other layer, while the allowed deviation becomes half the distance between the two most extreme values. Then, the associated scintillator hits in the forward pixel detectors of layers B and C are observed: For each of the pixels, a maximum and minimum number of tubes which could be associated with the pixel is stored in the look-up table. This information allows the DSP algorithms to associate tube-hits (stubs) with scintillator hits. Finally, for each possible value of ϕ within a given octant, determined by the pixel hits, and for each possible B+C combination of "centre-of-gravity" values in the two layers, the deflection with respect to the straight line through the nominal interaction point and the projection of the B-C trajectory into the middle of the magnetic toroid (see figure 4.2) are stored in yet another array, as well as ϕ and the corresponding pseudo-rapidity η from the direction of the muon before the deflection.
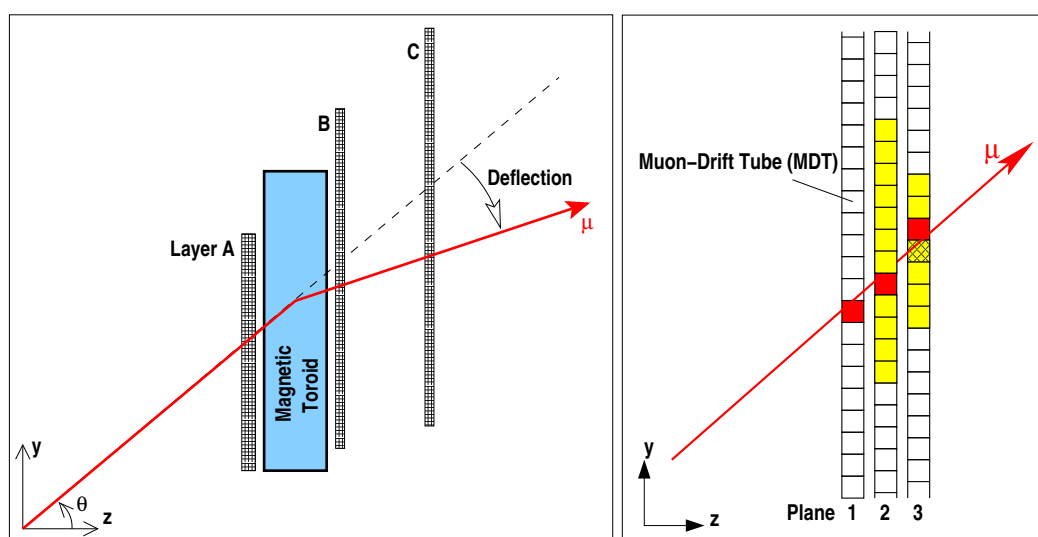
Figure 4.2: Left: Illustration of the typical path of a muon through the three layers of the forward muon system as seen from the side. The interaction point is in the origin of the coordinate system. In this particular case, where the muon crosses the top octants of the muon system, the muon drift tubes in the layers A, B and C as well as the magnetic field within the muon toroid are parallel to the *x* axis. The deflection angle from a given direction θ is a measure of the transverse momentum of the muon. The right illustration zooms in on the passage of the muon through an individual layer B (similar in C) of the forward-muon spectrometer. This schematic picture shows a three-hit candidate (the drift-tube hits are marked with red). Based on the hit in the first plane, the hit in the second plane has to be in the allowed range, represented in yellow. The valid hit range (yellow) in plane 3 is determined by the projection of the first two hits into the last plane (hashed MDT). For a detailed description of the definition of valid hits, the reader is referred to Appendix A.1.

4.2.4 Definition of Level-2 Muon Objects

The forward-ALPHA processor of the Level-2 Muon system receives all muon objects from the forward-SLICs in order of decreasing quality. After the forward-ALPHA processor has collected all the stubs from the layer-A and layer-BC algorithms, it matches each A-stub with the first BC-stub that fulfils the requirements

$$\Delta\phi \leq \pi/4 \ \text{ and } \ \Delta\eta \leq 0.3. \tag{4.1}$$

The quality of the L2-Muon objects is defined as:

- *loose*: `AQual` + `BCQual` ≥ 2

- *medium*: `AQual` ≥ 1 and `BCQual` ≥ 1

- *tight*: `AQual` + `BCQual` ≥ 4

After the matching of the stubs, the ALPHA algorithm uses another set of look-up tables, produced from Monte-Carlo simulations, to determine $\frac{Q \cdot \text{sign}(\text{Toroid})}{p_T}$ of the muon objects from the η and the *deflection* of the muons after the toroid.

The matching in the mixed-region between forward and central (around $|\eta| \approx 1$) is performed by the global-L2 algorithm from *loose* forward and central stubs using the requirement (4.1).

The following chapter, which will focus on the efficiency of the Level-2 muon trigger will refer to *loose* and *medium* L2 muons as they have been defined in this section.

5 Performance of the L2-Muon Trigger

The muon-related component of the DØ Level-2 trigger is not only the most complex system of Level-2, but was also the first to be used online (in December 2001) and the first trigger system that used the signals from the muon drift tubes to estimate the muon momenta and to trigger highly energetic muons at DØ in Run II. Today, there is hardly a single analysis with muons at DØ Run II, which does not, in one way or another, depend on data triggered also by the Level-2 muon system.

The different muon triggers in the DØ trigger menu, which is currently chosen for data taking, mainly require *medium* L2-muons without any explicit momentum cut or with a Level-2 transverse-momentum cut at $p_T^{L2} > 3\,\text{GeV}$ or $5\,\text{GeV}$ in order to increase the trigger rejection with respect to the first trigger level.

This section discusses the performance of the Level-2 muon system, mainly its efficiency, studied with data taken between June and September 2003.

The Figure 5.1 shows the spatial distribution of *medium* L2-Muon objects for high-p_T di-muon events. The "dip" in the azimuthal distribution at $\phi \approx 4.5$ reflects the degraded geometrical acceptance of the muon system in the central bottom part of the detector (cf. section 3.2.3). The dip at $\phi \approx 1.5$ comes from the specific selection of the high-p_T di-muon sample dominated by $Z/\gamma^* \to \mu\mu$ events, in which the two muons tend to emerge in opposite directions. Since the efficiency of the muon identification and triggering is decreased in the bottom region, the di-muon sample will also include fewer muons in the top part of the detector.

5.1 Efficiency

In order to determine the efficiency of the Level-2 muon trigger with respect to offline reconstructed muons, the data sample consists of events which fulfil the following trigger requirements:

- **At Level 1**: two scintillator muons found, each consisting of a coincidence of two scintillator hits before and after the muon toroid.

48
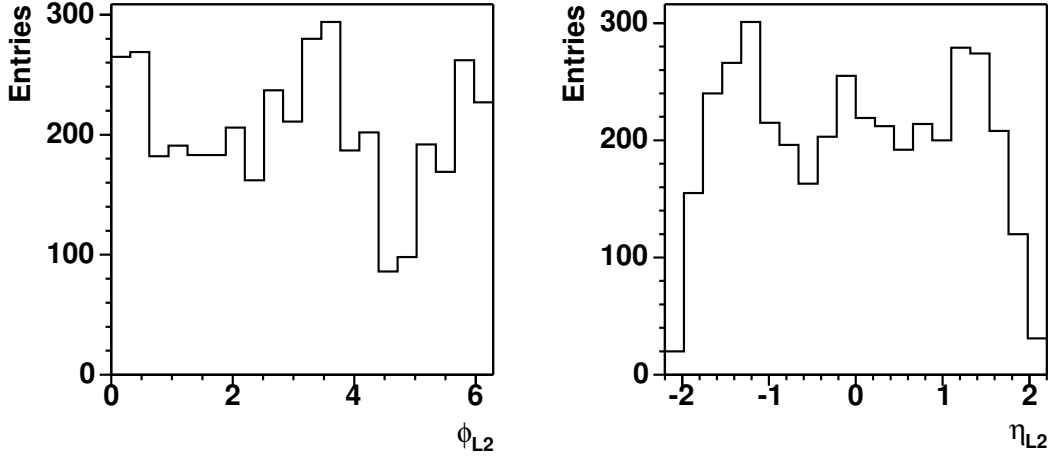
Figure 5.1: Distribution of all medium Level-2 Muons in a high-p_T di-muon sample as a function of ϕ (left) and η (right).

- **At Level-2**: one *medium* Level-2 muon found.

The events are reconstructed and all events with at least two medium[1] muons with a matching central track are considered if the two highest-p_T muons are separated by at least 1.0 rad in ϕ. The highest (second-highest) p_T muon must have a transverse momentum of at least 10 GeV (2 GeV). Furthermore, both muons must be isolated using the same criterion used in the analysis presented in chapter 6.4.3 (see equation (6.8)). This is necessary in order to reduce the probability for a false track-to-muon matching. Additionally, the central track associated with each muon must contain at least one hit in the silicon detectors (SMT).

Figure 5.2 shows the efficiencies for different Level-2 muon objects as a function of reconstructed muon-p_T for all muons of the data sample, for which the other muon could already be associated with a *medium* muon at Level-2. Herein, a L2-muon is identified with a reconstructed muon if $|\Delta\phi(\mu, L2)| < 0.7$ and $|\Delta\eta(\mu, L2)| < 1$. If no L2-muon is found within this geometrical window, the level-2 muon system is considered to have failed to identify this muon. Furthermore, only those of the two highest-p_T muons of each event are considered for which the other muon in the same event has an associated *medium* L2-muon. This way, the analysis is not biased by the trigger, which already contains the requirement of at least one *medium* muon at Level-2.

---

[1]Note that the quality assignment for reconstructed muons (i.e. "loose", "medium", and "tight") are different from those in Level-2 or other trigger levels, despite the same nomenclature. In this particular case, the attribute "medium" refers to reconstructed muons as will be described in a later chapter (cf. section 6.3.1).
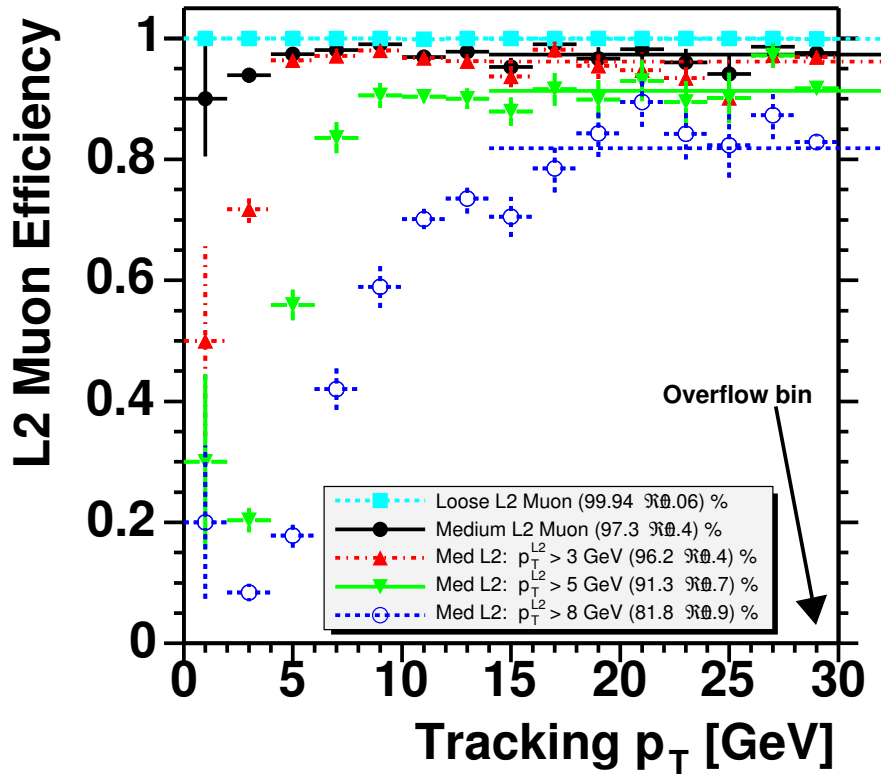
Figure 5.2: Level-2 Muon efficiency per single reconstructed muon as a function of the transverse momentum, measured by the central tracking system. The efficiency decreases with increased tightness and p_T cut on the Level-2 muon objects as is indicated by the horizontal line. These lines show the total efficiency for reconstructed tracks above $p_T = 14$ GeV. Only statistical errors are shown.

As can be seen in Figure 5.2, the efficiency with respect to high-momentum reconstructed muons ($p_T > 14\,\mathrm{GeV}$) is nearly 100% for *loose* L2-muons and about (97.5 ± 0.2)% for *medium* L2-muons without any cut on the L2-measured momentum. The associated single-muon efficiency for *medium* muons with cuts at different values of L2-p_T are also shown in Figure 5.2. The efficiency curves for the different cuts on Level-2 transverse momentum clearly show the shift of the trigger turn on to higher momenta.

The errors on the efficiencies presented in this chapter are the binomial errors from the statistical uncertainties only, systematic errors on the efficiencies have not been estimated. The statistical errors are determined assuming binomial statistics following the formula

$$\sigma_{\mathrm{eff}} = \sqrt{\frac{\varepsilon(1-\varepsilon)}{N_{\mathrm{tot}}}}, \tag{5.1}$$

where ε is the efficiency $\varepsilon = N(\text{L2 triggered})/N_{\mathrm{tot}}$ and N_{tot} is the total number of reconstructed muons entering the considered sample. As a consequence of equation 5.1, the determined errors are slightly underestimated for efficiencies close to 100% (or 0%) if N_{tot} is a small number. For a correct determination of the statistical error with small values of N_{tot}, the Poisson fluctuations of N_{tot} needed to be taken into account. For sufficiently large N_{tot} (and for efficiencies sufficiently smaller than 1 and greater than 0), as it is the case for the studies presented here, the discrepancy between the correct statistical error and equation 5.1 can be neglected.

Figures 5.3 and 5.4 show the efficiency for finding reconstructed muons in Level-2 as a function of ϕ and η. The four curves show the efficiency for *medium* L2-muons without and with various cuts on the L2-measured momenta of *medium* L2-muons. In these plots the efficiency without transverse-momentum cut in Level-2 is calculated from all reconstructed muons, while the determination of the efficiency for *medium*-L2 muons with a p_T^{L2} cut is determined from reconstructed muons which are associated to central tracks with $p_T > 10\,\mathrm{GeV}$ or $p_T > 12\,\mathrm{GeV}$ (see legends to Figures 5.3 and 5.4).

Figures 5.3 and 5.4 indicate that the variations of the efficiency in the forward system for *medium* muons is reasonably flat in ϕ. However, the efficiency fluctuations, in particular visible in the asymmetry between $\eta = \pm 1$ when applying momentum cuts at Level-2, cannot simply be explained by statistics. These effects become even larger with increased momentum cuts in Level-2. It is expected that these rather large fluctuations originate from an unoptimised description of the detector geometry in the Monte-Carlo simulation, which is used to fill the look-up tables used for the determination of the deflection of the muons in the magnetic field of the toroid. In fact, recent studies have revealed that these effects originate from a wrongly implemented geometry of the central muon system. After the shifts of the order of up to a few centimetres have been corrected in the DØ-detector simulation, the L2-Muon efficiency was shown to be fully recovered in the central region. During the shutdown period in autumn 2003, the look-up tables for the central L2-Muon system have been updated, taking advantage of the latest geometry surveys.
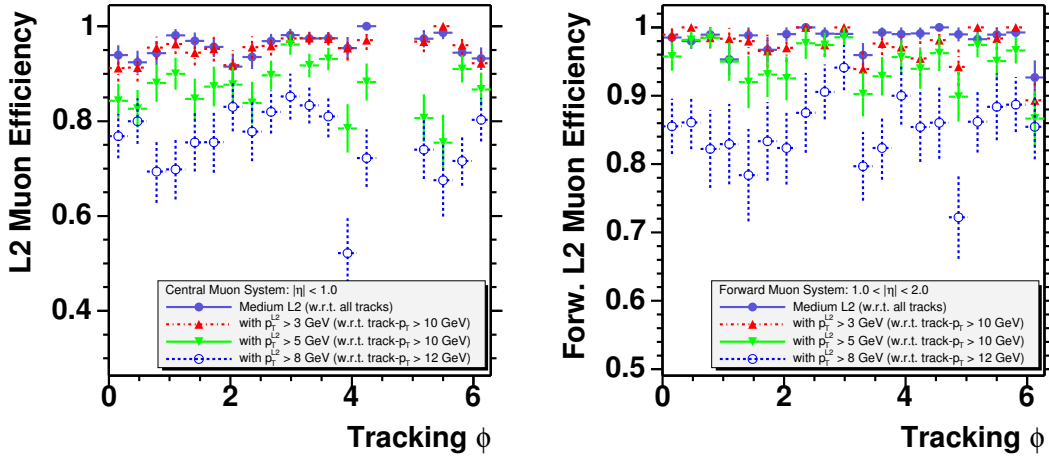
Figure 5.3: Single-muon efficiency of the Level-2 muon trigger for different L2-muon qualities as a function of ϕ for the central muon system (left) and the forward muon spectrometer (right). The filled blue circles denote the efficiency of associating a medium L2-muon to any track of the high-p_T di-muon sample defined in section 5, while the green open triangles, the filled red triangles and the open blue circles are the efficiency for a medium Level-2 muon with a cut at $p_T^{L2} > 3\,\text{GeV}$, $p_T^{L2} > 5\,\text{GeV}$ and $p_T^{L2} > 8\,\text{GeV}$, respectively. The latter three efficiencies are determined from a sample of reconstructed muons with transverse momentum that is significantly larger than the cut value at Level-2.
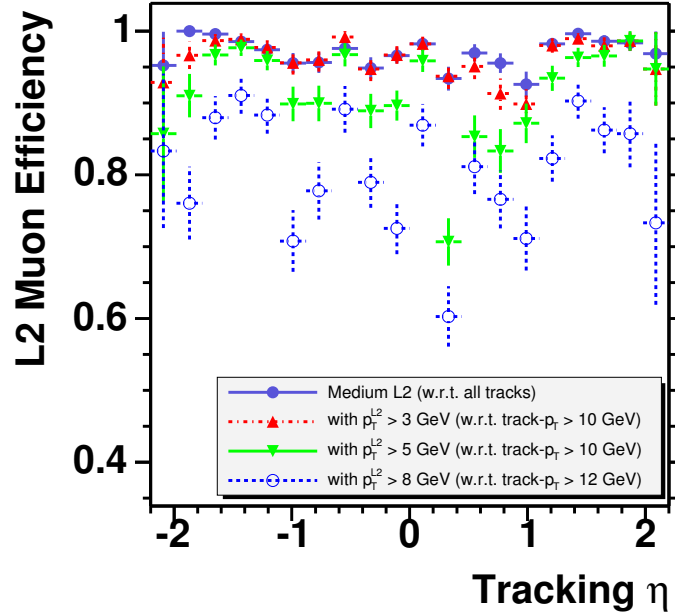
Figure 5.4: Single-muon efficiency of the Level-2 muon trigger for different L2-muon qualities as a function of η. See caption to Figure 5.3 for more details.

Figure 5.5 shows the angular distribution of all those reconstructed muons for which no *medium* Level-2 muon could be associated. Table 5.1 summarises the different efficiencies for high-momentum muons of commonly used Level-2 objects. The errors shown are statistical errors only. Systematic errors, which are not considered in this study, mainly arise from the definition of the base sample, i.e. the trigger, the muon identification and reconstruction as well as the cuts on the muon momenta, which select the physics processes entering this sample. Since the efficiencies for the forward and central muon system are different and since the detector is not fully symmetric with respect to rotations around the beam axis, the calculated efficiency will depend on the specific physics sample for which the efficiency is averaged over ranges of ϕ, η and/or p_T. On the other hand, the independent and therefore unbiased efficiency $\varepsilon = \varepsilon(\phi, \eta, p_T)$ cannot easily be determined due to lack of statistics.

5.2 Rejection

The rejection of a trigger is defined as the ratio of input over accept rate of a specific trigger requirement. In the case of the Level-2 muon system, the input rate is the output rate of the specific Level-1 trigger. At the DØ experiment, there are many different trigger

L2-Muon Object/Cut	Efficiency for $p_T > 14\,\text{GeV}$ Muons
Loose	0.9994 ± 0.0006
Medium w/o any p_T^{L2} cut	0.973 ± 0.004
Medium with cut at $p_T^{L2} > 3\,\text{GeV}$	0.962 ± 0.004
Medium with cut at $p_T^{L2} > 5\,\text{GeV}$	0.913 ± 0.007
Medium with cut at $p_T^{L2} > 8\,\text{GeV}$	0.818 ± 0.009

Table 5.1: L2-Muon efficiency for identifying a single muon with $p_T > 14\,\text{GeV}$ in Level-2 for varying L2-quality and transverse-momentum cut in Level-2. The errors denote statistical uncertainties only.
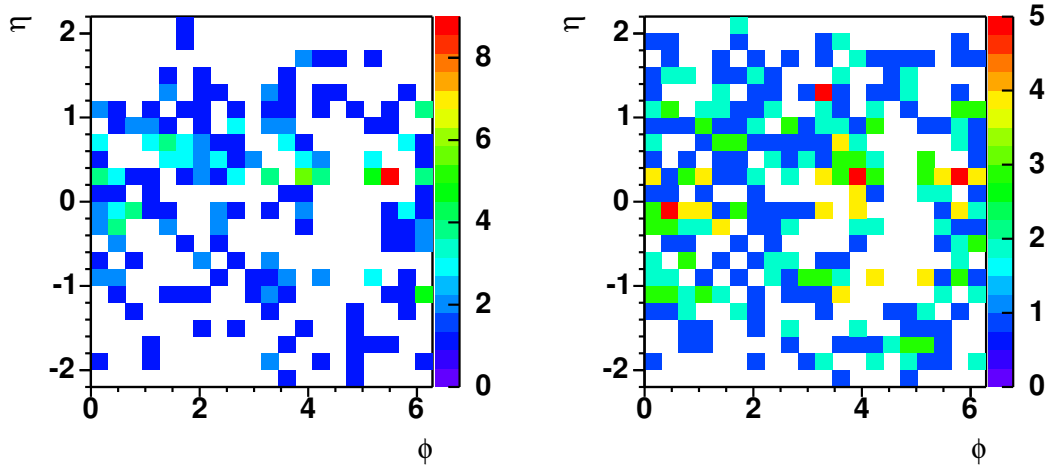
Figure 5.5: Left: all muons with $p_T > 10\,\text{GeV}$ without any associated *medium* Level-2 muon above $p_T^{L2} = 5\,\text{GeV}$. Right: all muons with $p_T > 12\,\text{GeV}$ without any associated *medium* Level-2 muon above $p_T^{L2} = 8\,\text{GeV}$.

combinations used during data taking. A specific trigger consists of a well defined trigger condition at any of the three trigger levels. In this section, the rejection of the Level-2 muon system is demonstrated for a few (by far not all) different trigger requirements at Level-2 with respect to different muon triggers at Level-1.

The single-muon Level-2 rejection of events triggered at Level-1 with the requirement of one or more scintillator muons varies between about 1.7 (for ≥ 1 *loose* L2-muons) and 16 (for ≥ 1 *medium* L2-muons with a Level-2 transverse momentum greater than $5\,\mathrm{GeV}$) [48]. A selection of the rejection factors for different single- and di-muon triggers is given in Table 5.2. These rejection factors originate from studies of a current trigger list which is used for a luminosity of approximately $4.0 \cdot 10^{31}\,\mathrm{cm^2 s^{-1}}$ [49].

	Level 1 trigger	Level-2 trigger	Rejection
1)	≥ 1 tight scint. muon, all-η	≥ 1 loose muon	1.6
2)	≥ 1 tight scint. muon, all-η	≥ 1 medium muon	3.2
3)	≥ 1 tight scint. muon, all-η	≥ 1 medium muon, $p_T^{L2} > 3\,\mathrm{GeV}$	4.3
4)	≥ 1 tight scint. muon, all-η	≥ 1 medium muon, $p_T^{L2} > 5\,\mathrm{GeV}$	10
5)	≥ 1 tight scint. muon, all-η + ≥ 1 loose wire muon	≥ 1 medium muon, $p_T^{L2} > 3\,\mathrm{GeV}$	1.7
6)	≥ 2 tight scint. muons, all-η	≥ 1 medium muon,	2.6
7)	≥ 2 tight scint. muons, all-η	≥ 1 medium $+1$ loose muons, separated by $\Delta\phi < 13.5^\mathrm{o}$ and $\Delta\eta < 0.15$	4.8
7)	≥ 2 tight scint. muons, all-η	≥ 2 medium muons	16.5
8)	≥ 1 tight scint. muons, $|\eta| < 1.5$ + ≥ 1 track with $p_t > 10\,\mathrm{GeV}$	≥ 1 loose muons	2.0
10)	≥ 1 tight scint. muons, $|\eta| < 1.5$ + ≥ 1 track with $p_t > 10\,\mathrm{GeV}$	≥ 1 medium muon, $p_T^{L2} > 5\,\mathrm{GeV}$	3.8

Table 5.2: Rejection of the Level-2 muon system for various Level-1 and Level-2 trigger definitions [49]. The rejection is defined as the ratio of Level-1 output to Level-2 accept rate. The rejection of Level-2 is given with respect to either tight scintillator muons (based on scintillator coincidences in at least two of the three layers of the muon system) or loose wire muons (based on multiple-hit clusters in one or more layers of the muon drift tubes) at the first trigger level. The trigger combinations 6) and 7) are used for the search for second-generation leptoquarks, i.e. all events which are triggered by at least one of the triggers 6) or 7) enter the preselection which will be described in the following chapter.

6 Data Sample, Triggers and Event Reconstruction

With the highest energetic proton-antiproton collisions, provided by the TeVatron accelerator, CDF and DØ are currently the experiments most sensitive to the direct detection of leptoquarks of the second generation.

In this chapter, the data sample, recorded with the DØ detector in 2002 and 2003, will be described as well as the Monte-Carlo simulations of both background and scalar leptoquark signal. The di-muon triggers of DØ, which define the basic event sample, will be introduced, and the trigger and reconstruction efficiencies for high-momentum di-muon + di-jet events will be discussed.

6.1 The DØ Data

The search for scalar second-generation leptoquarks is performed on a sample of proton-antiproton collisions recorded at DØ between August 2002 and June 2003.

Only events passing the di-muon triggers "`2MU_A_L2M0`" and "`2MU_A_L2ETAPHI`", are considered. At the first trigger level, these di-muon triggers require two *tight* muons, formed from a coincidence of scintillator hits in two layers of the DØ muon system, which consists of up to three layers (cf. section 3.2.3). In addition, at least one *medium* muon in the Level-2 trigger must be identified, consisting of a reconstructed track, based on hits in the proportional wire counters inside and outside the magnetic toroid. "`2MU_A_L2ETAPHI`" requires a second Level-2 muon of at least *loose* quality, separated from the first by at least 13.5° in ϕ and 0.15 in η.

6.2 The Monte-Carlo Samples

In order to compare the recorded data to simulated events, Monte Carlo (MC) samples for signal and background (see Table 6.1) have been produced with the `PYTHIA` event generator (version 6.202 [50]). On average, 1.1 (Poisson distributed) minimum-bias events were

added to each simulated event. `CTEQ4L` [28] has been used as the leading-order parton density function (PDF) for the leading-order simulation of both background and signal with PYTHIA. All simulated events are passed through a full GEANT [51] simulation of the DØ detector and are then reconstructed in the same way as the data. The cross-sections shown in Table 6.1 are the leading-order calculations from `PYTHIA`.

Process	$\sigma \times BF$ [pb]	Generated events
$Z/\gamma^* \to \mu\mu$ (+ jets), $15\,\text{GeV} < M_{Z/\gamma^*} < 60\,\text{GeV}$	543	19 250
$Z/\gamma^* \to \mu\mu$ (+ jets), $60\,\text{GeV} < M_{Z/\gamma^*} < 130\,\text{GeV}$	182	310 500
$Z/\gamma^* \to \mu\mu$ (+ jets), $130\,\text{GeV} < M_{Z/\gamma^*} < 250\,\text{GeV}$	1.3	10 000
$Z/\gamma^* \to \mu\mu$ (+ jets), $250\,\text{GeV} < M_{Z/\gamma^*} < 500\,\text{GeV}$	0.11	18 500
$Z/\gamma^* \to \mu\mu$ (+ jets), $M_{Z/\gamma^*} > 500\,\text{GeV}$	0.005	9 500
$t\bar{t} \to WW + ... \to \mu\nu\mu\nu + ...$	0.07	9 500
$WW \to \mu\nu\mu\nu$ (+ jets)	0.009	45 500
Scalar $LQ_2\overline{LQ_2} \to \mu j \mu j$, $M_{LQ_2} = 140\,\text{GeV}$	1.7	8 500
Scalar $LQ_2\overline{LQ_2} \to \mu j \mu j$, $M_{LQ_2} = 160\,\text{GeV}$	0.8	6 750
Scalar $LQ_2\overline{LQ_2} \to \mu j \mu j$, $M_{LQ_2} = 180\,\text{GeV}$	0.4	7 750
Scalar $LQ_2\overline{LQ_2} \to \mu j \mu j$, $M_{LQ_2} = 200\,\text{GeV}$	0.2	8 000
Scalar $LQ_2\overline{LQ_2} \to \mu j \mu j$, $M_{LQ_2} = 220\,\text{GeV}$	0.1	7 250
Scalar $LQ_2\overline{LQ_2} \to \mu j \mu j$, $M_{LQ_2} = 240\,\text{GeV}$	0.06	8 250
Scalar $LQ_2\overline{LQ_2} \to \mu j \mu j$, $M_{LQ_2} = 260\,\text{GeV}$	0.03	8 500

Table 6.1: Monte-Carlo samples used in this analysis. The values for the cross-section (σ) $\times$ branching fraction (BF) shown in this table are obtained from `PYTHIA` [50] using `CTEQ4L` [28]. The signal samples consist of the scalar-leptoquark pair production in $p\bar{p}$ collisions at the TeVatron, decaying into two muons (μ) and two jets (j).

The cross-sections for the leptoquark pair production used in this analysis, however, are not the cross-sections calculated by the PYTHIA event generator, but those from calculations with a tool provided by Krämer et al. [27] as described in section 2.3. For the determination of these cross-sections, the parton density functions `CTEQ4L` and `CTEQ4M` were used for the leading-order and next-to-leading order calculations, respectively.

The dominant background in searches for leptoquarks in the di-muon + di-jet ($\mu j + \mu j$) channel are Drell-Yan (DY) $p\bar{p} \to Z/\gamma^* + X \to \mu\mu + X$ processes, where X stands for any combination of additional jets (or leptons). In addition, small contributions can be expected from $W^+W^- + X \to \mu\nu\mu\nu + X$ and top-antitop production. These are the three Standard-Model background processes which are included in this analysis.

Additional background coming from QCD processes and W+jets (with ≥ 1 fake muons) events is generally low due to the excellent shielding of the DØ muon detectors. It

is further reduced by muon-isolation requirements. The QCD background, dominated by $b\bar{b}$ events, is minimised by requiring two highly energetic, isolated muons and a large invariant di-muon mass, and by requiring opposite charges of the two reconstructed muons. These processes are estimated to contribute less than 1 % to the observed rate at high di-muon masses [52] where the search for leptoquarks takes place and can, therefore, be neglected.

Requiring a large di-muon mass also rejects nearly all contributions from $Z/\gamma^* + X \rightarrow \tau\tau + X \rightarrow \mu\nu_\tau\mu\nu_\tau + X$ events which are therefore ignored in this analysis.

6.3 Event Reconstruction

The jets and muons in the data and the Monte-Carlo simulation are reconstructed with the latest DØ reconstruction software. These reconstruction algorithms provide the latest detector geometry corrections in order to obtain optimised resolutions and efficiencies for muons and jets. This section describes the muon and jet identification and reconstruction, and it introduces corrections to the simulated muons and jets to improve their agreement with the DØ data.

6.3.1 Muon Reconstruction

Only muons of at least *loose*[1] quality, reconstructed from hits in the scintillation counters and the proportional drift tubes before and after the shielding toroid, are taken into account, provided the simultaneous "global fit" of the muon tracks in the muon chambers with a track in the central tracking system converges. When two or more muons are required in an event, at least one of the two most energetic muon tracks needs to have at least one hit in the silicon detectors ($N(SMT) \geq 1$). This cut removes badly reconstructed di-muon tracks and tracks with large closest distance from the nominal interaction point (e.g. from cosmic muons). Tracks with "axial only" information (i.e. without stereo hits in the central fibre tracker) are not considered. If at least two muon scintillators are hit, loose cuts on the timing differences remove out-of-time muons (cosmics).

The momentum information of the muons is taken from the central tracks associated with the muons. In order to account for a worse muon-momentum resolution in data as compared to the simulation, the reconstructed muon momenta for Monte-Carlo events are smeared using

$$\frac{1}{p_T(\text{MC})} \rightarrow \frac{C}{p_T(\text{MC})} + \sigma_{\text{smear}} \cdot R_{\text{Gauss}}, \qquad (6.1)$$

---

[1]A loose muon fulfils at least two of the following three criteria: 1. at least one hit in the A-layer scintillators and at least two hits in the A-layer drift tubes; 2. at least two hits in the BC-layer drift tubes; 3. at least one BC scintillator hit. If 3. is not fulfilled, at least one scintillator hit must be present in layer A.

where R_{Gauss} is a random Gaussian distribution with zero mean and width $\sigma(R_{\text{Gauss}}) = 1$. C and σ_{smear} are parameters which have been optimised to describe the $Z \to \mu\mu$ resonance in the di-muon mass spectrum in the data. While C is compatible with unity, a value of $\sigma_{\text{smear}} = 0.002\,\text{GeV}^{-1}$ was chosen. This smearing of the simulated muon momenta accounts for the overestimated position resolution of the tracking system, while the angular resolution of the muons is assumed to be correctly simulated. Only muons within the geometrical window of $|\eta| < 1.9$ are accepted.

6.3.2 Jet Reconstruction

Jet Definition

Calorimeter jets are reconstructed from the energy depositions in the calorimeter cells with a cone algorithm and a cone size of $R = \sqrt{\Delta\phi^2 + \Delta\eta^2} = 0.5$. The jets are required to pass the following quality criteria:

- $N_{90} > 1$
  (N_{90} is the number of calorimeter towers containing together 90 % of the energy of a jet).

- $0.05 < \texttt{EMfrac} < 0.95$
  (`EMfrac` is the fraction of the jet energy deposited in the *electro-magnetic* part of the calorimeter).

- $\text{CHF} < 0.4$
  (CHF is the fraction of energy deposited in the coarse hadronic layer of the calorimeter).

- Hot fraction < 10.0
  (ratio of energy of highest energy to next-to-highest energy calorimeter tower).

- $\text{CHF} < 0.15$ or $f_{90} < 0.5$
  ($f_{90} = N_{90}/n_{\text{itm}}$, where n_{itm} is the total number of towers in a jet).

- The jet should be well contained in the calorimeter: $|\eta| < 2.4$.

Jet-Energy Scale Correction

The energy of the jets is corrected to account for fragmentation energy outside the jet cone, calorimeter noise and underlying event energy within the jet cone . The jet energies are studied in γ+jet(s) events: The electromagnetic shower from the highly-energetic photon is well contained within a few calorimeter cells and therefore allows a precise

measurement of the energy of the photon[2], recoiling from the jet. Transverse-momentum conservation then allows the correction of the 0.5-cone jet energy. [53]

The jet-energy correction, however, was determined for a different (i.e. older) reconstruction version than used in this analysis. Therefore, small changes of the jet-energy scales can arise due to the different treatment of the Intercryostat region (cf. section 3.2.2) and modified calorimeter thresholds.

Since the update of the jet-energy-scale correction for the latest reconstruction version has not been available at the time this document was composed, the analysis presented here uses the available—though older—jet corrections. In order to study the influence and potential bias from using a different jet-reconstruction, a small event sample (both data and $Z \to \mu\mu$ Monte-Carlo) was reconstructed with both the old and the current (new) reconstruction software. If jets, identified in both reconstruction versions, agree in direction by $\Delta R = \sqrt{\Delta\phi^2 + \Delta\eta^2} < 0.3$, the relative difference $\Delta E_T / E_T$ of the resulting transverse jet-energy is determined. Figure 6.1 shows the result versus η, separately for data and Monte Carlo for all jets exceeding a transverse energy of 15 GeV. From these distributions, one can clearly see that there are no significant differences in the central region ($|\eta| < 1$), while the jet-energies for jets in the direction of the Intercryostat detectors (ICD) at $|\eta| \approx 1.4$ are up to 10 % larger in the new reconstruction version. On the other hand, one can also see that the difference is similar for data and Monte-Carlo, so that a significant bias from the different jet energies in the different reconstruction versions can be neglected. However, the distributions shown in Figure 6.1 are averaged from all jets (above $E_T^{new} > 15$ GeV), independent of their energy.

A closer look reveals that the relative difference between the jet energies from the different reconstruction versions in the ICD regions depends on the transverse jet-energy, as can be seen in Figure 6.2 where the profile is shown for three different bins of $E_T \equiv E_T^{new}$. In particular, these distributions show a difference between the data and the simulation of up to 5 % for transverse energies below 25 GeV. However, these differences are much smaller than the associated errors on the jet-energy corrections, for which a systematic error will be determined later, and can, therefore, be ignored. Note that in the search for second-generation leptoquarks presented in this document, only jets above 25 GeV are considered, as will be described in the preselection in section 7.2.2.

6.3.3   Simple Correction of Mismeasured Muon Momenta

As described in section 6.3.1, the muon momenta are determined from the curvature of the central tracks in the magnetic field of the solenoid. A detailed study of the di-muon mass spectrum of $Z/\gamma^* \to \mu\mu$ Monte-Carlo events has shown, however, that for a fraction

---

[2]The photon-energy depositions in the calorimeter are similar to those from electrons. Therefore, the photon-energy measurement can be calibrated with the use of $Z \to ee$ events.

of DY $Z/\gamma^* \rightarrow \mu\mu$ events a di-muon mass is reconstructed above the Z resonance, in the region used for searching for leptoquarks. This is due to the overestimation of at least one muon's transverse momentum [54]. Although there is no reason to believe that this effect is different for data and Monte Carlo, this effect leads to relatively large weights at high di-muon masses for $Z/\gamma^* \rightarrow \mu\mu$ Monte-Carlo events generated at $M_{Z/\gamma^*}^{gen} \approx M_Z$, due to the high cross-section and the limited Monte-Carlo statistics. This can be understood from the following example: The Monte-Carlo statistics for masses around the Z-resonance correspond to around ten times the statistics of the data sample. Therefore, if we neglect efficiencies for the moment, each Monte-Carlo event of this sample contributes to 0.1, which is much larger than the contribution of a single event from a Monte-Carlo event at higher masses $M_{Z/\gamma^*}^{gen} > M_Z$ (see Table 6.1). Since the number of events at very high di-muon masses is relatively small, a few $Z/\gamma^* \rightarrow \mu\mu$ events with overestimated muon-momenta (and therefore overestimated di-muon mass) dominate the uncertainty from limited Monte-Carlo statistics and also lead to rather fluctuating distributions when requiring high di-muon masses.

In order to reduce the contribution from events with overestimated di-muon masses, yet another definition of the di-muon mass, $M'(\mu\mu)$, is introduced, which is based on the fact that no or only little missing transverse energy is expected in DY Z/γ^* background and signal events. The missing transverse energy ($\not{E}_T$) of each event is estimated from the momenta of all muons and jets (with $E_T^{jet} > 20\,\text{GeV}$) within an event. Then the transverse momentum of the highest-p_T muon, which is assumed to be the wrongly measured muon, is scaled such that the missing transverse energy vanishes. It turns out that, using this approach, indeed most of the overestimated di-muon masses in simulated events get a corrected di-muon mass $M'(\mu\mu)$ which is in better agreement with the mass M_{Z/γ^*}^{gen} at which they were generated [54].

In the following, whenever the di-muon mass is referred to $M(\mu\mu)$, no matter whether in distributions or when applying cuts on $M(\mu\mu)$, the di-muon mass is taken as the minimum of the originally reconstructed and the corrected di-muon mass:

$$M(\mu\mu) \rightarrow \min\left(M(\mu\mu), M'(\mu\mu)\right). \tag{6.2}$$

The effect of this simple correction is shown in Figure 6.3: Using $\min\left(M(\mu\mu), M'(\mu\mu)\right)$ instead of the uncorrected di-muon mass shifts the di-muon mass to lower values, and, most importantly, removes most of the events, for which the di-muon mass is overestimated by more than 50%. As can be seen in Figure 6.3, the mass resolution of the Z resonance is degraded by the use of the corrected muon momenta. This effect is expected, since the missing transverse energy has only been estimated from a sum over all four-momenta of all muons and jets above a certain threshold. Neglecting jets with a transverse energy below 20 GeV in this $\not{E}_T$-estimate, for instance, worsens the mass resolution when the muon momenta are corrected. This is true, however, for both the simulation and the

data, and since the search for second-generation leptoquarks is performed at very high di-muon masses, the benefit from a reduction of the Standard-Model background at high di-muon masses outweighs the degraded muon-momentum resolution.

6.4   Trigger and Reconstruction Efficiencies

As will be described in the following chapter, the luminosity of the data sample, $L = \int \mathcal{L} dt$, is determined by a fit of the di-muon mass spectrum of the Drell-Yan (DY) Z/γ^* Monte-Carlo events to the data. This "effective" integrated luminosity, $\tilde{L}' = L \cdot c'$, where $c' = \frac{\varepsilon_{\text{data}}}{\varepsilon_{\text{MC}}}$ contains the difference of the reconstruction efficiencies for high-p_T di-muons as well as the trigger efficiency[3], is sufficient for calculating upper cross-section limits, provided the two muons from the leptoquark decays have similar properties, or—in other words—provided that this correction factor c' is independent of η, ϕ and p_T of the muons. The *absolute value* of the different efficiencies, however, does not influence the limit calculations.

In good approximation, the correction factor c' can be factorised as follows:

$$c' = \varepsilon_{\text{trigger}} \cdot \left(\frac{\varepsilon_{\text{data}}^{\text{loose di}-\mu}}{\varepsilon_{\text{MC}}^{\text{loose di}-\mu}} \right) \cdot \left(\frac{\varepsilon_{\text{data}}^{\text{tracking}}}{\varepsilon_{\text{MC}}^{\text{tracking}}} \right)^2 \cdot \left(\frac{\varepsilon_{\text{data}}^{\text{isolation}}}{\varepsilon_{\text{MC}}^{\text{isolation}}} \right)^2. \tag{6.3}$$

The η, ϕ and p_T dependence of each of the different efficiencies shown in equation (6.3) will be discussed in this section. The difference of the geometrical acceptance of the DØ detector and its simulation enters by the factors associated with the muon reconstruction (for *loose* muons) and the tracking.

6.4.1   Tracking Efficiency

The tracking efficiency is studied with a sample of triggered di-muon events for which two isolated medium muons with $p_T^{\text{local}} > 7 \, \text{GeV}$ are required. Note that this momentum, p_T^{local}, does not rely on any central-track information but is determined from the signals in the muon system only, based on the deflection within the magnetic field of the muon toroids. One of the two muons is required to be associated with a central track with $p_T > 20 \, \text{GeV}$ while the transverse momentum of the second muon, as measured by the local muon system only, is required to be at least $15 \, \text{GeV}$. Furthermore, the two muons are required to be separated in ϕ by $\Delta\phi > 2.4$. It has been shown that cuts like these, by requiring a track for one of the two muons only, still select a reasonably pure sample of $Z \rightarrow \mu\mu$ events [57].

---

[3]No trigger simulation for Monte-Carlo events is used in this analysis.

For all events fulfilling these requirements, the fraction of events for which the second muon can be matched to a central track (with $N(SMT) \geq 1$),

$$\varepsilon^{\text{tracking}} = \frac{N(\mu \text{ with track match})}{N(\mu)}, \tag{6.4}$$

is calculated and studied with respect to p_T^{local}, ϕ and η of the test muon (see Figure 6.4). While the ϕ and p_T dependences of the tracking efficiency prove to be reasonably flat, the lower left plot of Figure 6.4 shows that the efficiency of associating a track with a high-p_T muon is *not* flat in η and even the ratio $\varepsilon_{\text{data}}^{\text{tracking}}/\varepsilon_{\text{MC}}^{\text{tracking}}$ of the efficiencies for data and Monte Carlo depends on the muon direction. This ratio, parameterised by a fifth-order polynomial, is shown in the lower right plot of Figure 6.4.

In order to correct for the η-dependence of the ratio of tracking efficiency in data and Monte-Carlo, all simulated di-muon events in this analysis are weighted with the factor

$$W(\eta_1, \eta_2) = \frac{\varepsilon_{\text{data}}^{\text{tracking}}}{\varepsilon_{\text{MC}}^{\text{tracking}}}(\eta_1) \cdot \frac{\varepsilon_{\text{data}}^{\text{tracking}}}{\varepsilon_{\text{MC}}^{\text{tracking}}}(\eta_2), \tag{6.5}$$

obtained from the fit shown in Figure 6.4. Herein, η_1 and η_2 denote the directions of the two muons.

Note that, since the difference of the tracking efficiency between data and Monte Carlo was corrected, the correction factor c' in equation (6.3) for the effective integrated luminosity, $\tilde{L} = L \cdot c$, changes to

$$c \equiv c' \cdot \left(\frac{\varepsilon_{\text{data}}^{\text{tracking}}}{\varepsilon_{\text{MC}}^{\text{tracking}}}\right)^{-2} = \varepsilon_{\text{trigger}} \cdot \left(\frac{\varepsilon_{\text{data}}^{\text{loose di}-\mu}}{\varepsilon_{\text{MC}}^{\text{loose di}-\mu}}\right) \cdot \left(\frac{\varepsilon_{\text{data}}^{\text{isolation}}}{\varepsilon_{\text{MC}}^{\text{isolation}}}\right)^{2}. \tag{6.6}$$

6.4.2 Trigger and Muon Identification

Since the triggers used in this analysis had varying prescales and efficiencies throughout the period of data taking, the absolute value of the efficiency of the triggers is not determined in this study. These triggers heavily rely on the muon system and its efficiency. Therefore, the efficiency of triggering *and* reconstructing a high-p_T di-muon pair in data, divided by the efficiency of reconstructing the two loose muons in the simulation, i.e. the first two factors of the right hand side in equation (6.6) is examined. This factor,

$$\varepsilon_{\text{trigger}} \cdot \left(\frac{\varepsilon_{\text{data}}^{\text{loose di}-\mu}}{\varepsilon_{\text{MC}}^{\text{loose di}-\mu}}\right), \tag{6.7}$$

is sufficiently flat in η, ϕ and p_T. As discussed above, the absolute values of the efficiencies do not directly enter this analysis, and the trigger and reconstruction efficiencies

need not to be unfolded. The factor defined in equation (6.7) is studied by comparing the η and ϕ distributions of triggered and reconstructed isolated di-muon pairs (dominated by $Z \rightarrow \mu\mu$ events) to DY-Z/γ^* events simulated with PYTHIA. A muon has to be reconstructed as *loose* with a central-track match of $p_T > 15\,\text{GeV}$. In order to exclude effects from tracking, the Monte-Carlo events are weighted with the tracking factor (6.5) derived from the tracking efficiencies. Figure 6.5 shows the η (upper left) and ϕ (upper right) distributions for di-muon pairs. The "bottom hole" in ϕ is excluded in the η-distribution, while the ϕ-distribution in the right plot is shown for di-muon pairs in the $|\eta| < 1$ range only, in order to enhance the "bottom-hole" effect of the central muon detectors. The "bottom hole" in ϕ is mirrored at $\phi \approx 1.5$ due to the back-to-back nature of di-muon events from DY-Z/γ^* processes[4]. The Monte-Carlo distributions are normalised to the total number of data entries in the histograms. The lower histograms, showing the ratio of data over background, indicate the flatness of the muon triggers and reconstruction with respect to the Monte Carlo simulation. Fluctuations from one bin to another are not expected to give rise to any bias to the analysis, since they average out due to the η and ϕ distributions of the physics processes being sufficiently flat.

6.4.3 Isolation Efficiency

The last efficiency to be studied for its "flatness" is that of the isolation cut which is applied to the high-momentum muons in this analysis. The isolation is defined as follows:

$$E^{\text{Cal}}_{0.4\text{Cone}} - E^{\text{Cal}}_{0.1\text{Cone}} < 2.5\,\text{GeV}, \tag{6.8}$$

where $E^{\text{Cal}}_{X\text{Cone}}$ is the calorimeter energy in a cone of size $\Delta R_{\mu j} = \sqrt{\Delta\phi^2_{\mu j} + \Delta\eta^2_{\mu j}} = X$ around the muon [58].

The isolation efficiency is studied with a sample of di-muon triggered events for which two track-matched *medium*[5] muons with a minimum transverse-momentum of $15\,\text{GeV}$ are required. In order to obtain a pure sample of $Z \rightarrow \mu\mu$ events, the two muons are required to be separated by $\Delta\phi > 2.4$ and their invariant di-muon mass should lie in the mass window $60\,\text{GeV} < \text{M}(\mu\mu) < 120\,\text{GeV}$. Only one muon needs to be isolated, while the isolation of the second muon is investigated. As can be seen in Figure 6.6, the isolation criterion for $Z \rightarrow \mu\mu$ events is consistent with the Monte-Carlo simulation: Herein, the lines indicate first-order polynomial fits to the data and Monte-Carlo isolation efficiencies (see caption

---

[4]This "mirroring" effect of the "bottom hole" inefficiency is enhanced in comparison to Figure 5.1 due to the more stringent requirements on the di-muon sample. Furthermore, Figure 6.5 shows the ϕ distribution for the central muon system only (i.e. $|\eta| < 1$).

[5]Medium muons fulfil the following criteria based on signals in the muon detectors: 1. at least two hits in the A-layer drift-chambers; 2. a matching A-layer scintillator hit; 3. at least two wires hit in the BC-layers; 4. at least one matching scintillator hit in the BC-layers.

to Figure 6.6). The fit results for data and Monte Carlo are in accordance within their statistical uncertainties.

The slope in the p_T dependence of this isolation efficiency originates from the fact that a certain hadronic activity is expected even for $Z \rightarrow \mu\mu$ events in $p\bar{p}$ collisions. This means that a certain fraction of "good" muons from $Z \rightarrow \mu\mu$ events will be rejected when they are close to a jet. This, however, is more likely to happen for the lower-momentum muon of a $Z + \text{jet}(s) \rightarrow \mu\mu + \text{jet}(s)$ event, which can be understood from the following kinematic argument: In the rest frame of the decaying Z boson, the two muons have the same absolute value of their momenta. But if the Z boson is recoiling from a jet, a muon pointing into the "jet hemisphere" (i.e. "backward" with respect to the flight direction of the Z boson) has lower momentum than the muon travelling in the direction of the boosted Z boson. This effect is visible in form of a slight slope for both Monte Carlo and data in the upper right plot of Figure 6.6.

The different sources of inefficiency, included in the definition of the effective integrated luminosity (see equations (6.3) and (6.6)), were discussed in this section. In summary, leaving the tracking efficiency aside, all these factors were shown to lead to no significant bias of a high-momentum di-muon analysis, since the ratios of the efficiencies as determined in the data and the simulation are sufficiently flat in η, ϕ and p_T of the muons. Since this is not the case for the tracking efficiency, the Monte-Carlo weight in equation (6.5) was introduced to compensate for the difference between the tracking efficiencies in data and Monte-Carlo.
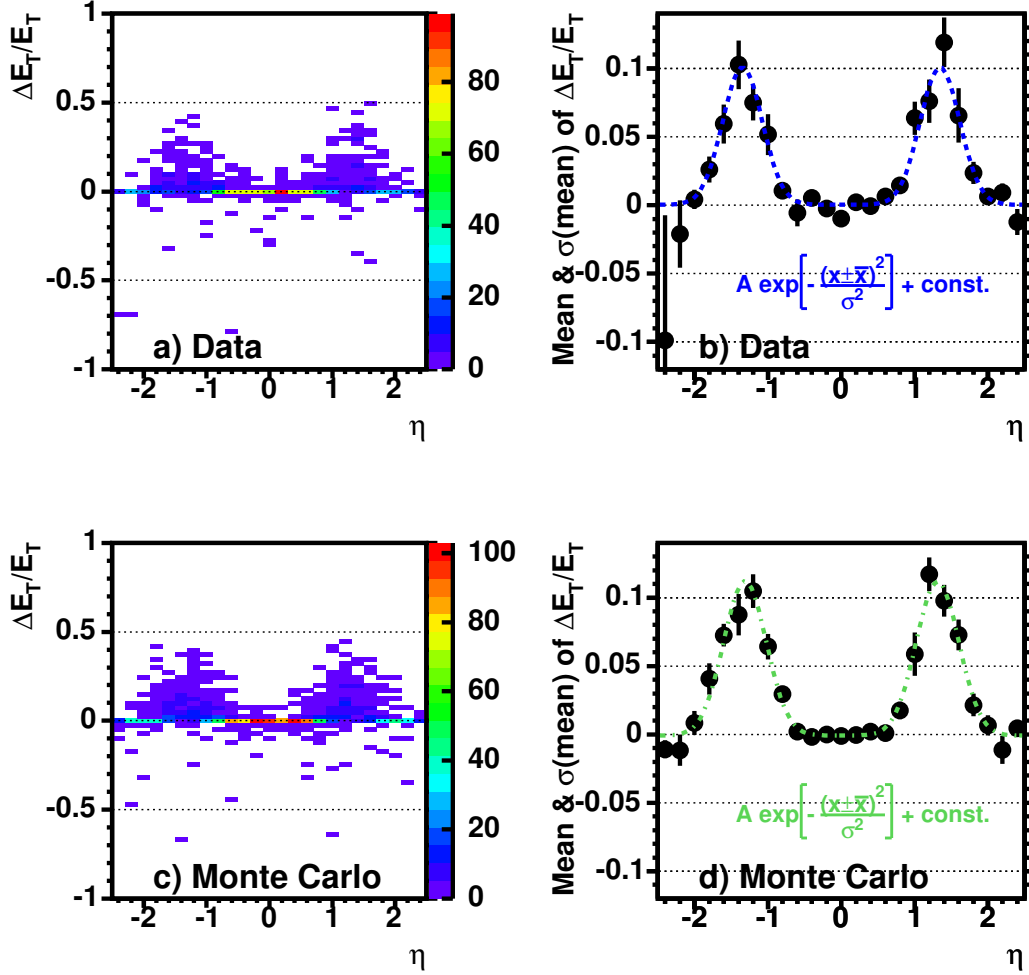
Figure 6.1:   Comparison of jet-energies from *old* and *new* jet-reconstruction for data (top) and Drell-Yan $Z/\gamma^* \rightarrow \mu\mu$ simulation (bottom). In the left histograms, the distribution of $\Delta E_T/E_T = (E_T^{new} - E_T^{old})/E_T^{new}$ is shown versus η. The histograms on the right show the corresponding profile plots, with the dots marking the mean value and the "error bars" denoting the r.m.s. spread of the mean of $\Delta E_T/E_T$ within each bin of η. All jets which have been reconstructed with both, the old and the new reconstruction software, are considered if their transverse energy exceeds $E_T^{new} = 15\,\text{GeV}$. In order to guide the eye, the dashed lines in plot b) and d) show the result of a Gaussian fit with a constant offset. Herein, the same Gaussian (with width σ, height A and mean $\pm\bar{x}$) is simultaneously fitted to the ICD regions at $|\eta| \approx \pm 1.2$ on both sides of the detector.
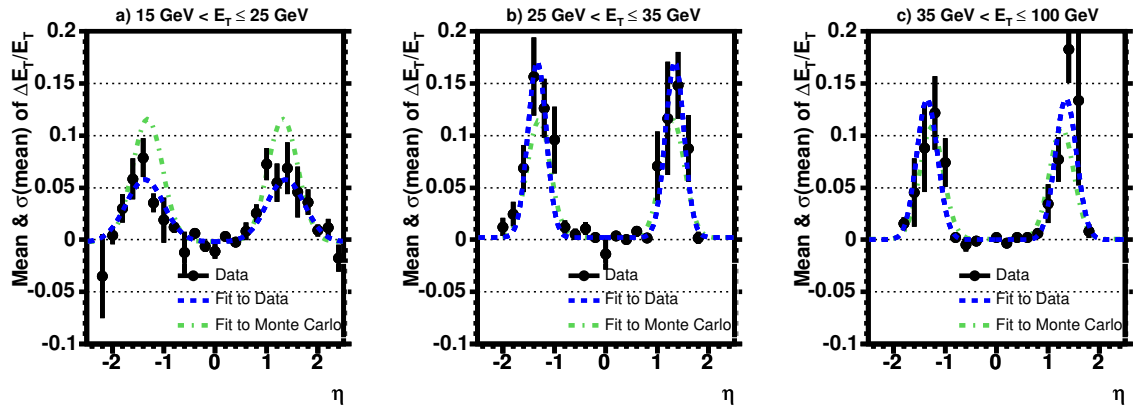
Figure 6.2: Mean and spread the mean of $\Delta E_T/E_T$ of all jets as described in Figure 6.1, but for different ranges of the transverse jet-energy E_T^{new}. Note that only jets with a transverse energy larger than 25 GeV (i.e. jets in the middle and right plot) enter the search for second-generation leptoquarks as will be described in section 7.2.1.
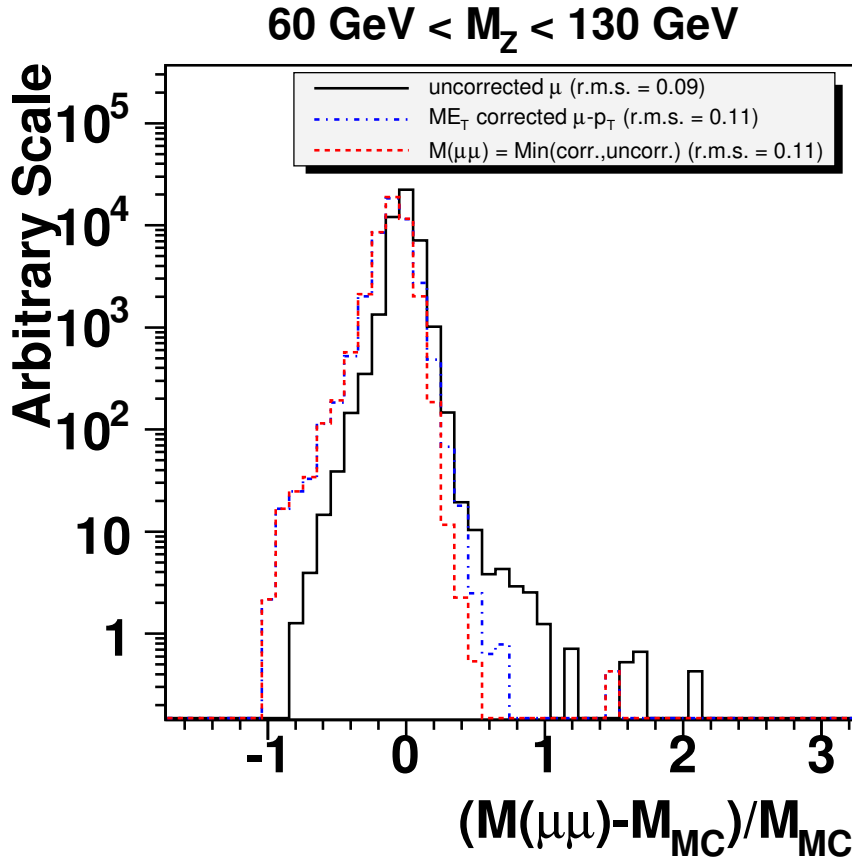
Figure 6.3: Di-muon mass resolution, $(M(\mu\mu) - M^{gen}_{Z/\gamma*})/M^{gen}_{Z/\gamma*}$, for Drell-Yan $Z/\gamma^* \to \mu\mu$ Monte-Carlo events, generated at masses in the range $60\,\mathrm{GeV} < \mathrm{M}^{gen}_{Z/\gamma*} < 130\,\mathrm{GeV}$: The solid black line shows the uncorrected di-muon mass-resolution, the green dash-dotted line represents the corresponding distribution when the highest-p_T muon is corrected for the reconstructed missing transverse energy $\not{E}_T$, and the red dashed line denotes the resolution for $\min(M(\mu\mu), M'(\mu\mu))$, the minimum of the latter two masses.
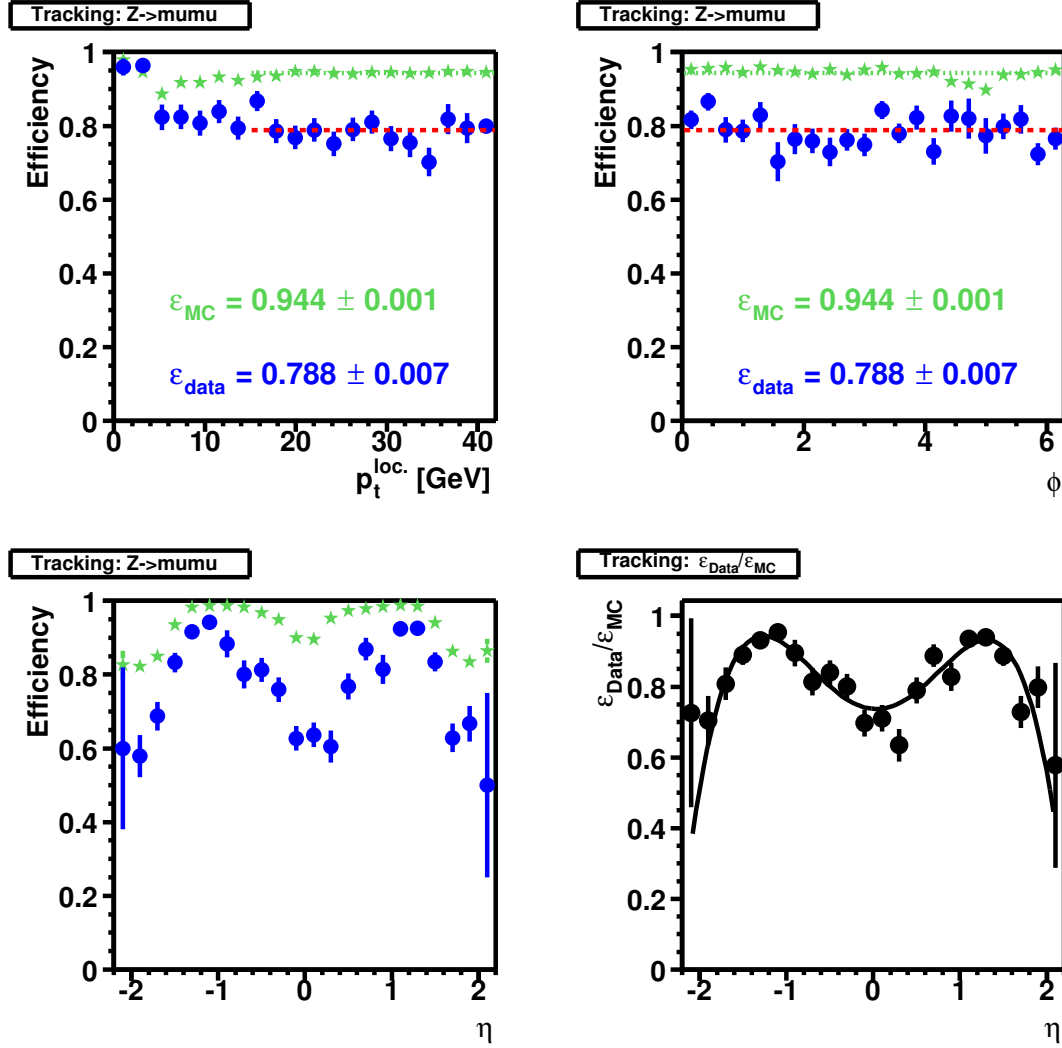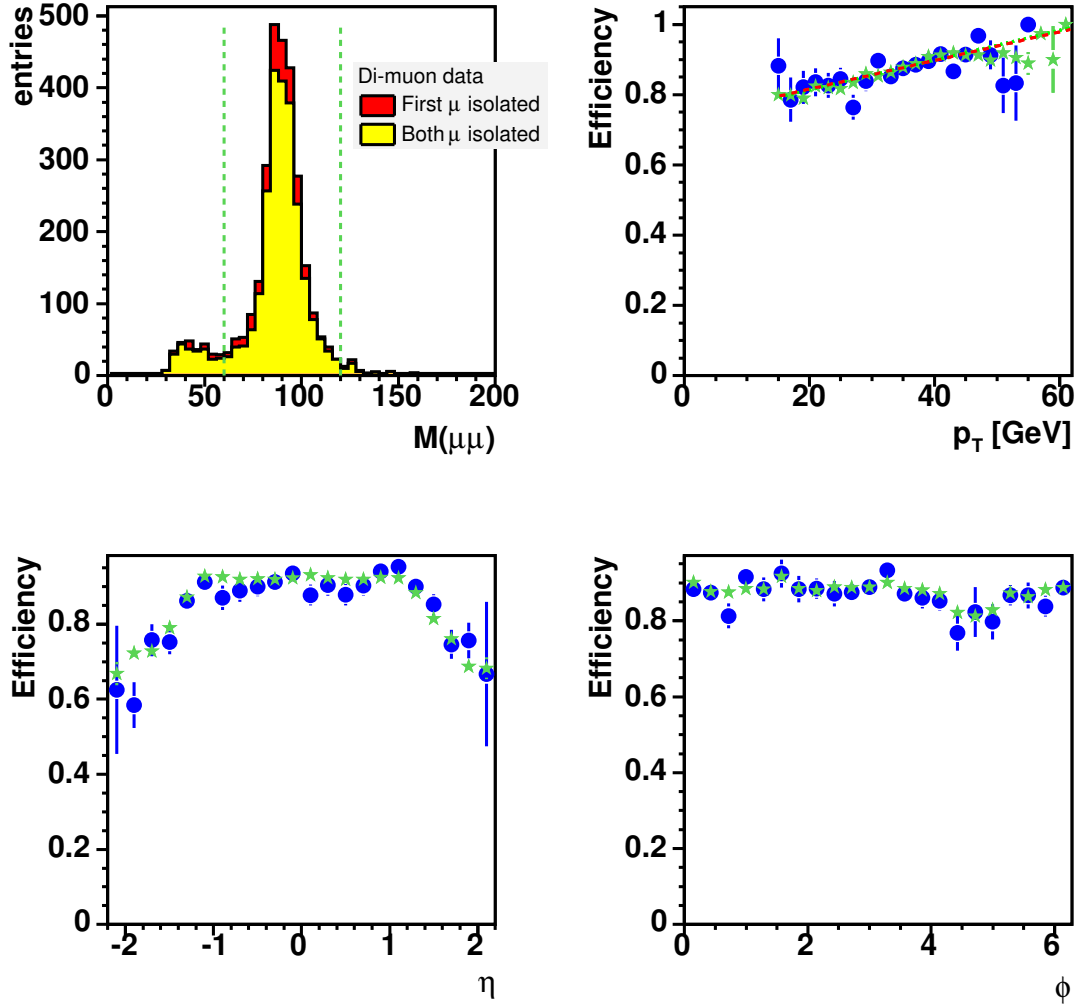
Figure 6.4: Tracking efficiency with respect to p_T^{local}, ϕ and η for data (blue circles) and Monte Carlo (green stars). The lower right diagram shows the ratio of the efficiencies in data and Monte-Carlo with respect to η. The solid line represents the result of a fifth-order polynomial fit, used to compensate for the difference between the data and the simulation.
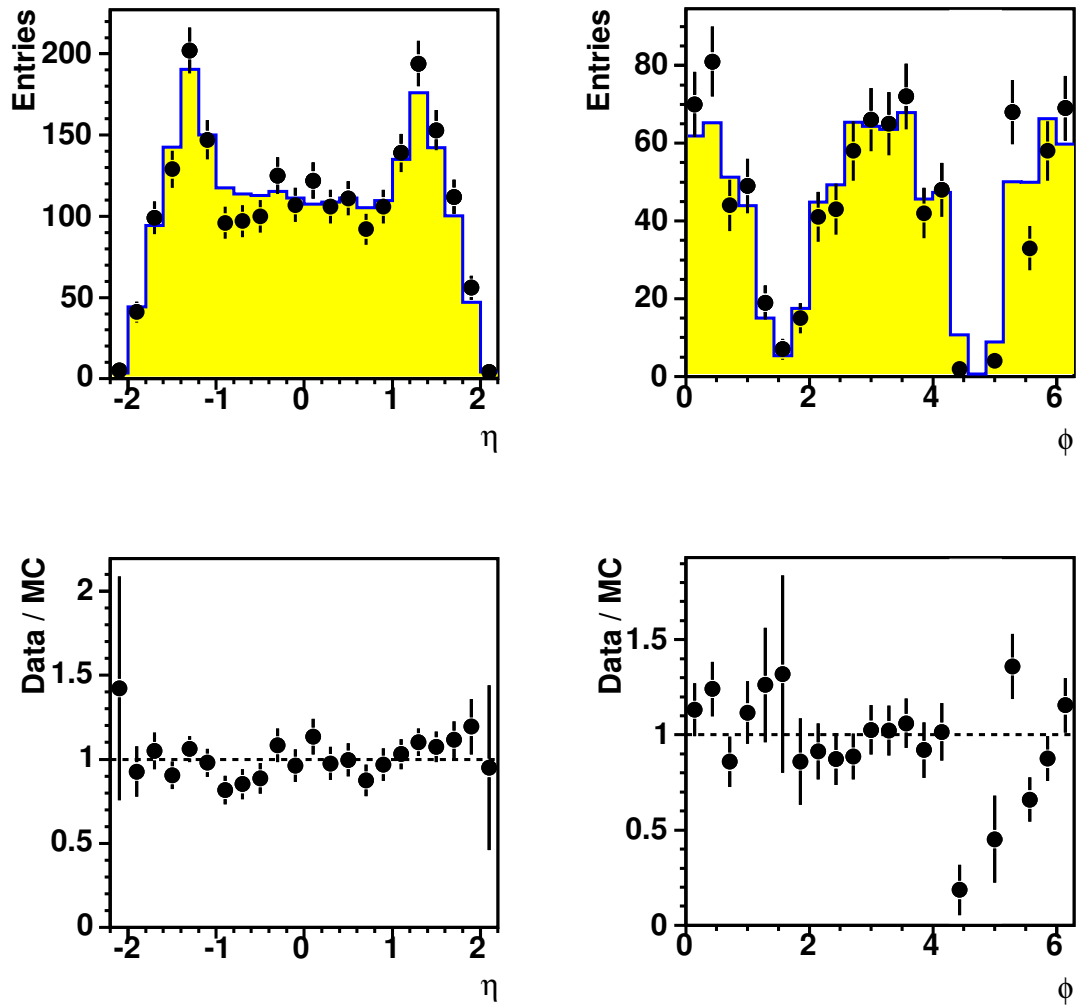
Figure 6.5: Triggered and reconstructed di-muon events as compared to reconstructed Monte-Carlo DY-Z/γ^* events for di-muon pairs outside the central "bottom-hole" (upper left) and for central-only di-muons (upper right). The lower plots show the corresponding ratio of data over Monte Carlo in these regions.

Figure 6.6: Isolation efficiency with respect to p_T, η and ϕ of the muons for data (blue circles) and Monte-Carlo (green stars). The lines in the upper right plot show a linear fit to the p_T distribution of the isolation efficiency with the following parameters: $\varepsilon_{isol.} = (0.0041 \pm 0.0008)\,\mathrm{GeV}^{-1} \cdot p_T + (0.75 \pm 0.03)$ for data (red) and $\varepsilon_{isol.} = (0.0042 \pm 0.0002)\,\mathrm{GeV}^{-1} \cdot p_T + (0.73 \pm 0.01)$ for Monte Carlo (green).

7 Search for Second-Generation Leptoquarks in $\mu\mu+$jets Events

The previous chapter described the basic ingredients for analyses involving highly energetic muons and jets at the DØ experiment: the data and Monte-Carlo samples, the muon and jet reconstruction, and the necessary corrections to the simulated events in order to obtain an accurate description of the data. Using these tools, this chapter describes the search for second-generation leptoquarks in $\mu j + \mu j$ events, starting with an estimate of the integrated luminosity of the data sample. Then the jet properties of Drell-Yan $p\bar{p} \to Z/\gamma^* + X \to \mu\mu + X$ events are reviewed and an event selection is described which provides the best separation of leptoquark signal and Standard-Model background events. Finally, the signal efficiency and systematic effects are discussed.

7.1 Di-Muon Events: Luminosity

7.1.1 Estimate of the Integrated Luminosity

Using a sample of isolated high-p_T di-muon events, the overall product $\tilde{L} = L \cdot c$ (where L is the integrated luminosity and c is given by equation (6.6)) is determined by a comparison of data with Drell-Yan $Z/\gamma^* \to \mu^+\mu^-$ events from Monte-Carlo simulation.

For this comparison, the following cuts are applied:

- Two muons of *loose* quality are required with $p_T^\mu > 15\,\text{GeV}$ and opposite charge, as measured by the curvature of the associated central-track match.

- At least one of these two muons must have one or more SMT hits associated to its central track.

- Both muons must be isolated as defined in equation (6.8).

- The invariant di-muon mass must exceed $30\,\text{GeV}$.

The Standard-Model background, dominated by Drell-Yan $Z/\gamma^* \rightarrow \mu\mu$ production, is normalised to the data by simply requiring the area in the di-muon mass resonance to be equal for data and Monte Carlo between $M(\mu\mu) = 70$ and $110\,\mathrm{GeV}$. In the following, the resulting normalisation factor for the di-muon spectrum of the background Monte Carlo is referred to as F_{Z/γ^*}.

Figure 7.1 shows the di-muon mass distributions of the data as compared to smeared Monte Carlo.
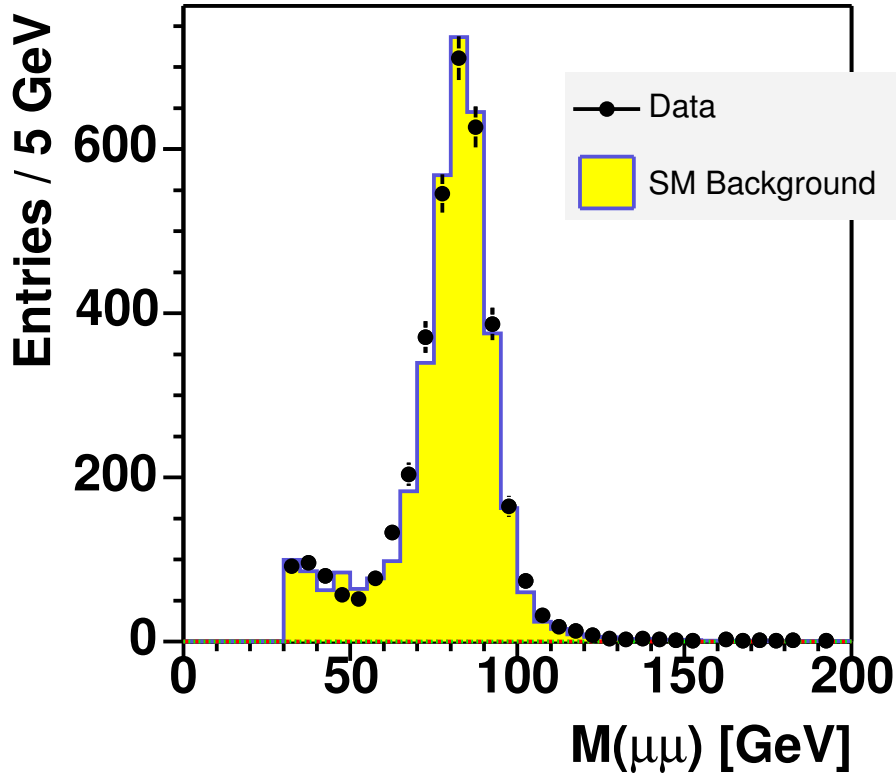
Figure 7.1: Di-muon mass spectrum for data (black dots with error bars) and Z/γ^* Monte Carlo (filled histogram).

During Run I, the DØ experiment measured the cross-section times branching ratio to $\sigma_Z \cdot BF(Z \rightarrow ee) = (218 \pm 11 \pm 12)\,\mathrm{pb}$ [59] [1]. This cross section is multiplied by a

---

[1]A similar measurement was also performed for the di-muon channel, but the uncertainties are much larger than in the di-electron channel in Run I.

correction factor that accounts for the higher centre-of-mass energy $\sqrt{s}$ in Run II:

$$\frac{\sigma_{CompHEP}(\sqrt{s} = 1.96\,\text{TeV})}{\sigma_{CompHEP}(\sqrt{s} = 1.8\,\text{TeV})} = 1.096, \tag{7.1}$$

where $\sigma_{CompHEP}$ is the leading order result for the cross-section as computed with `CompHEP` [60] using the parton density function `CTEQ5M` [61]. The product of luminosity times the ratio of data over Monte-Carlo efficiencies then becomes

$$\tilde{L} = L \cdot c = (N_{Z/\gamma^*}^{gen} \cdot F_{Z/\gamma^*})/\sigma_Z = (97.2 \pm 9.7)\,\text{pb}^{-1}, \tag{7.2}$$

where the factor c (cf. equation (6.6)) accounts for differences in the reconstruction efficiencies between data and Monte Carlo as well as the trigger efficiency, while the tracking efficiencies are already corrected in the Monte Carlo. N_{Z/γ^*}^{gen} is the number of generated Monte-Carlo events.

7.1.2 Systematic Errors of the Luminosity

Table 7.1 summarises the different errors in the measurement of the effective luminosity of the data sample. The different error sources are treated as follows:

- **Limited Monte-Carlo statistics:**
  Since the Monte-Carlo sample used for the determination of the luminosity comprises roughly ten times the statistics of the data sample, the uncertainty from limited Monte-Carlo statistics is small and can be neglected. Table 7.1 shows the statistical uncertainty, determined from the square root of the number of data events in the normalisation window.

- **Cross-section prediction for Drell-Yan $Z/\gamma^* \to \mu\mu$:**
  The relative systematic error on the cross-section for the Standard-Model is taken from the measurement [59].

- **Muon resolution and smearing:**
  The muon resolution is worse in the data compared to the prediction from the full simulation. This effect is corrected by smearing the Monte-Carlo momenta such that they reproduce the width of the Z resonance seen in data (see section 6.3.1). In order to acquire a conservative estimate of the effect from the wrongly estimated/smeared muon-p_T resolution, the smearing factor σ_{smear} in formula (6.1) has been varied by $\pm 1/3 \times \sigma_{smear}$. The result is illustrated in Figure 7.2. The resulting changes in the effective luminosity represent the systematic uncertainty.

- **Correction of the tracking efficiency:**
  As described in section 6.4.1, the tracking efficiency of high-momentum muons is overestimated in the simulation. This effect has been corrected by re-weighting each Monte-Carlo muon with an η-dependent weight. The systematic uncertainty related to the muon tracking was obtained by observing the effect from a $\pm\sigma_{stat}$ variation of the correction parameters, which were acquired from a fit. It is worth noting, that only a wrongly estimated η dependence of equation (6.5) could lead to a bias. The over-all normalisation of this correction does not lead to any bias, since an overestimated tracking efficiency would automatically be compensated in the determination of the effective luminosity.

- **QCD and fake-muon background:**
  The contribution of non-DY backgrounds under the *Z* resonance was estimated to be less than 2 % [52], which is taken as an additional systematic source for this analysis.

- **Arbitrariness of the normalisation window:**
  The corresponding systematic uncertainly was obtained by observing the effect on $\tilde{L}$ when varying the normalisation interval $70\,\mathrm{GeV} \leq M(\mu\mu) < 105\,\mathrm{GeV}$ by $\pm 5\,\mathrm{GeV}$ on both sides.

Source of luminosity uncertainty	Relative error
Statistical error	1.9 %
Prediction of $\sigma(Z \to \mu\mu)$ [59]	7.5 %
Muon resolution	2.4 %
Tracking efficiency correction	5.3 %
QCD + instrumental background	2 %
Arbitrariness of normalisation window	1.4 %
Total	10 %

Table 7.1: Summary of the errors associated with the measurement of the effective luminosity for the data sample used in this analysis. The total error is obtained by adding individual errors in quadrature.

In the following, only events with a di-muon mass greater than 60 GeV are considered. This way, contaminations from QCD processes as well as fake muons are further reduced.
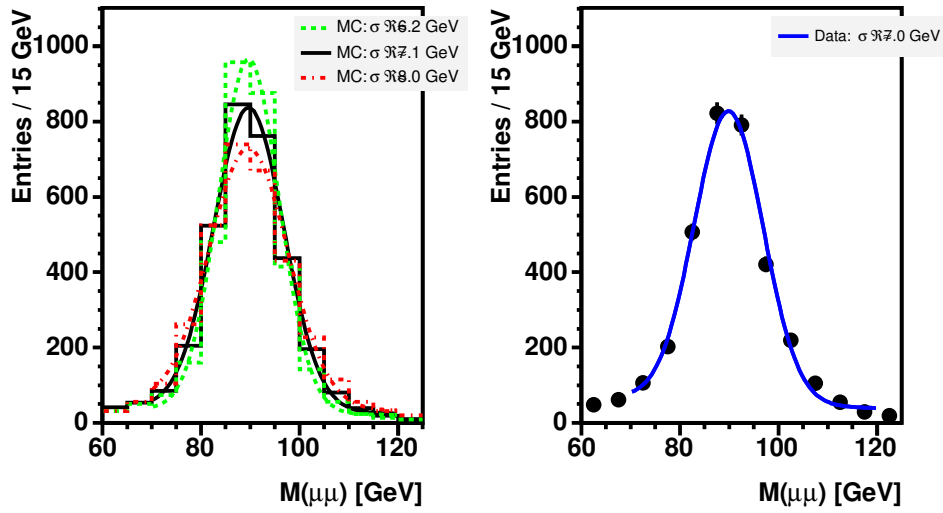
Figure 7.2: Invariant di-muon mass for Monte-Carlo (left) and data (right). The simulated distributions on the left are smeared according to equation (6.1) with different smearing factors: While the black solid line shows the standard smearing value, the green and red dashed curves denote the resulting mass resolution for a relative variation of the default smearing factor by $\pm 1/3$. The Gaussian fits to the histograms illustrate the corresponding changes in the observed width of the Z resonance (see legends).

7.2 The $\mu j + \mu j$ Selection
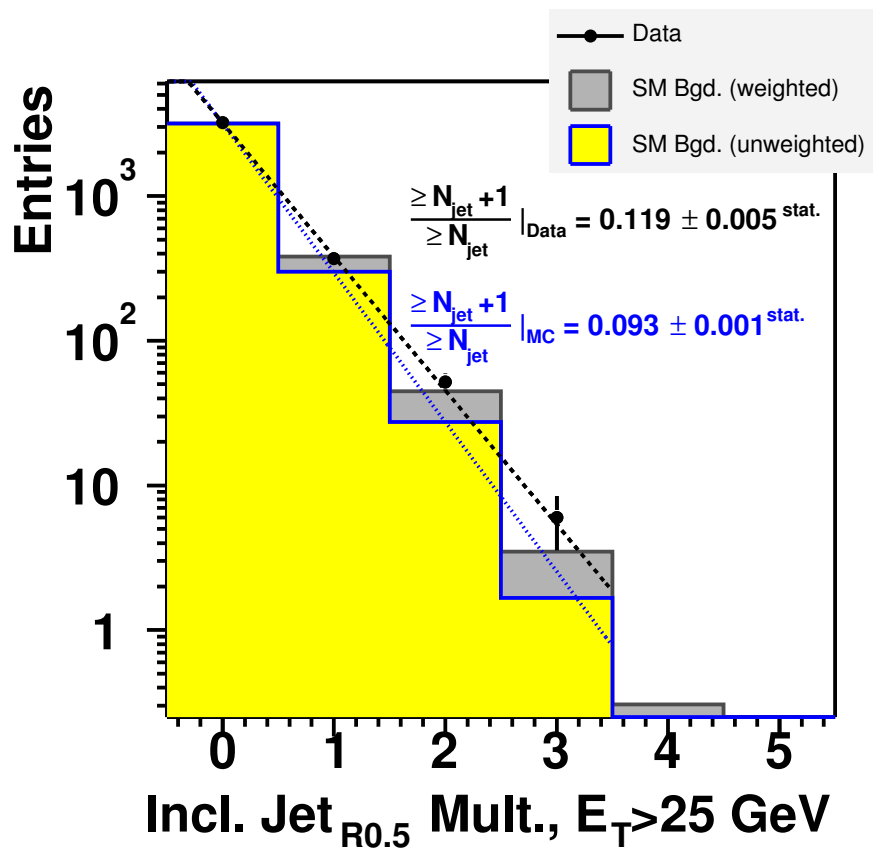
7.2.1 Jets in Drell-Yan Z Events

As described in section 6.3.2, jets in the DØ detector are reconstructed from energy depositions in the calorimeter cells using a 0.5-cone algorithm. The jet-finding algorithm requires at least one tower of calorimeter cells[2] of 8 GeV or more energy deposition as a starting seed for each jet. As a consequence, the detector and the jet reconstruction is inefficient for jets below a certain energy. Recent studies at DØ have shown that, although the plateau of the reconstruction efficiency for 0.5-cone jets is not quite reached at $E_T \approx 20$ GeV, the ratio of the efficiency in data and Monte-Carlo is flat in η and E_T and the efficiencies in data and Monte-Carlo differ by less than 3 % [62]. Since the jets from the heavy leptoquark decays are expected to be highly energetic, a cut on the transverse jet-energy of 25 GeV was chosen, i.e. a reconstructed jet must a transverse energy exceeding 25 GeV in order to be considered.

It is expected that the leading-order simulation of Drell-Yan Z/γ^* processes underestimates the jet multiplicity of the data, as can be seen from Figure 7.3 where the inclusive jet multiplicity for data is compared to the simulation. Similar to previous analyses at DØ Run II [56, 63], it is necessary to apply a correction of the jet multiplicity in Monte-Carlo events generated with PYTHIA.

Figure 7.3 shows the number of events with N_{jet} or more jets with $E_T > 25$ GeV and $|\eta| < 2.4$ for the di-muon data and $Z \to \mu\mu$ Monte Carlo. The straight lines show exponential fits to the data and the unweighted Monte-Carlo spectrum, resulting in the double ratio $\frac{\geq N_{\text{jet}}+1}{\geq N_{\text{jet}}}|_{data} / \frac{\geq N_{\text{jet}}+1}{\geq N_{\text{jet}}}|_{MC} = 1.28 \pm 0.06\,(\text{stat.})$. This result is compatible with earlier measurements of the jet multiplicity in Z events [64].

The simulated Drell-Yan $Z \to \mu\mu$ events are now weighted such that their jet multiplicity reflects the ratio measured in data for di-muon masses in the window $60\,\text{GeV} <$ $\text{M}(\mu\mu) < 105\,\text{GeV}$. This is achieved by counting all jets in a simulated Z-event with $E_T > 25$ GeV and $|\eta| < 2.4$ and by weighting the event with a factor of 1.28 per jet in the following distributions. This correction factor, $1.28 \pm 0.06\,(\text{stat.})$, is determined from the ratios of the exponential fits to data and Monte-Carlo as shown in Figure 7.3. The corresponding systematic uncertainty associated with this re-weighting of DY-Z/γ^* background events is taken from a variation of the weighting factor within one standard deviation of its statistical error.

---

[2]Simply speaking, a succession of calorimeter cells in the same direction (η, ϕ) at different depths of the calorimeter is called *calorimeter tower*.

Figure 7.3: Inclusive number (i.e. $\geq N$) of jets in Drell-Yan $Z \to \mu\mu$ events in the di-muon mass window $60\,\text{GeV} < \text{M}(\mu\mu) < 105\,\text{GeV}$ for 0.5-cone jets with $E_T > 25\,\text{GeV}$ and $|\eta| < 2.4$ for data and Monte-Carlo.

7.2.2 Di-Muon and Di-Jet Events in a Cut-Based Analysis

For the decay of a pair of second-generation leptoquarks into a charged lepton and a quark (i.e. $\beta = BF(LQ_2 \to \mu j) = 1$), one expects two high-$p_T$ muons and two highly energetic jets with no or little missing transverse energy. Therefore, the preselection requires the following cuts in addition to those already imposed on the two muons (cf. section 7.1):

- di-muon mass $M(\mu\mu) > 60$ GeV and

- two or more 0.5-cone jets of $E_T > 25$ GeV and $|\eta| < 2.4$.
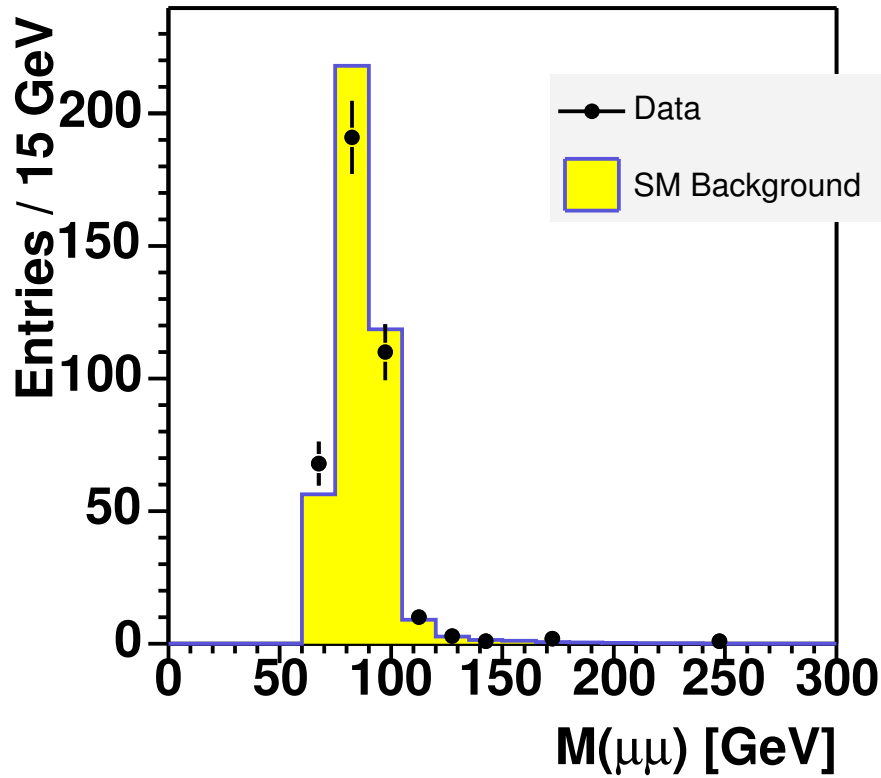
Figure 7.4: Invariant di-muon mass of $\mu\mu + N$jet events ($N \geq 1$) for data and simulated Standard-Model background.

Figure 7.4 and 7.5 show the di-muon mass spectrum for all $\mu\mu + N$jet events with $N \geq 1$ and $N \geq 2$, respectively. In order to further reduce the background contribution, an additional cut on the di-muon mass at $M(\mu\mu) > 105$ GeV is applied. This cut is also needed in order to be statistically independent from the sample which was used to determine the

correction factor for the jet multiplicity in leading-order Monte-Carlo DY-Z/γ^* events. Three events remain in the data after this cut. Appendix C shows the DØ event-displays for these three events.
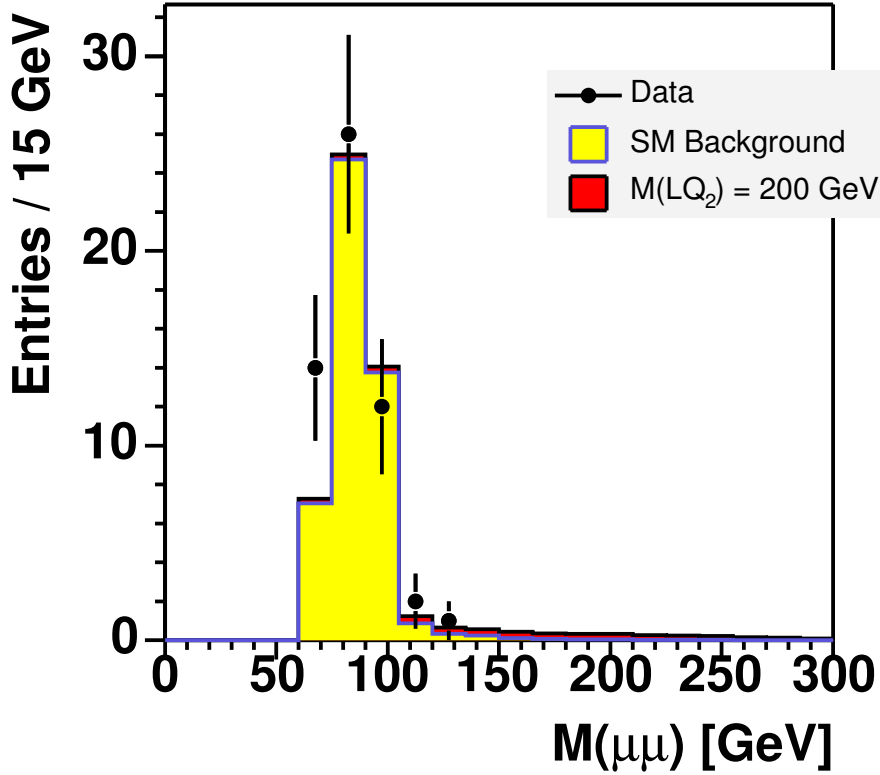
Figure 7.5: Invariant di-muon mass of events with at least two jets ($E_T > 25$ GeV) for data, Standard-Model background and scalar leptoquarks with a mass of $M_{LQ_2} = 200$ GeV.

Cut Optimisation

The previous paragraphs and sections introduced the basic preselection of highly energetic di-muon + di-jet events. In summary, all events are required to have

1. two or more isolated muons with a transverse momentum greater than 15 GeV,

2. two jets with a transverse energy exceeding 25 GeV, and

3. an invariant di-muon mass larger than 105 GeV.

Neglecting the jet masses, $\mu j + \mu j$ events are fully described by twelve parameters—e.g. the two angles and the energy of each of the four objects—if one assumes no more objects in the event. Assuming that there is no missing energy, which is a good approximation for both leptoquark events and DY-Z/γ^* processes, the equation

$$\sum_{\mu j \mu j} \begin{pmatrix} p_x \\ p_y \end{pmatrix} = \begin{pmatrix} 0 \\ 0 \end{pmatrix} \tag{7.3}$$

constrains the transverse momenta of the system, leaving ten parameters in total. Since the physics processes are symmetric with respect to rotations around the beam pipe (i.e. rotating all objects by the same angle ϕ_0), one is left with at maximum nine parameters which can be used to separate signal from background. This does not mean, however, that there exist necessarily nine independent variables which are all powerful in distinguishing signal from background. The boost of the event parallel to the beam pipe, for instance, i.e. the z-component of the momenta of the initial partons, only carries little information to be used to distinguish signal from background.

In order to further separate the signal from the remaining Standard-Model background, a variety of kinematic distributions of the $\mu\mu + jj$ system was studied, of which

- the invariant mass of the $\mu\mu + jj$ system,

- the reconstructed leptoquark mass $M(\mu j)$,

- the scalar sum of the transverse energies of the $\mu\mu + jj$ system, $S_T = \sum_{\mu\mu jj} E_T$,

- the direction $|\eta|$ of the di-muon system,

- the missing transverse energy,

- the relative difference of the transverse jet-energies, $\frac{|E_T^{jet1} - E_T^{jet2}|}{E_T^{jet1} + E_T^{jet2}}$,

- the angle between the planes defined by the two $\mu + j$ systems which minimise the difference in their reconstructed masses,

- the angle between the di-muon and the di-jet planes,

- and, of course, yet again the di-muon mass $M(\mu\mu)$

are a subset. As an example, Figures 7.6 and 7.7 show for the remaining $\mu j + \mu j$ events the scalar sum of the transverse energies of the $\mu j \mu j$-system, $S_T = \sum_{\mu j \mu j} E_T$, the "event mass" $M(\mu j \mu j)$, and the reconstructed μj-mass, respectively. The reconstructed μj-mass, $M(\mu j)$, is the mean of the masses of the two $\mu + j$ systems for the combination which minimises the $M(\mu j)$-difference $\Delta M = |M(\mu_1 j_{1'}) - M(\mu_2 j_{2'})|$.
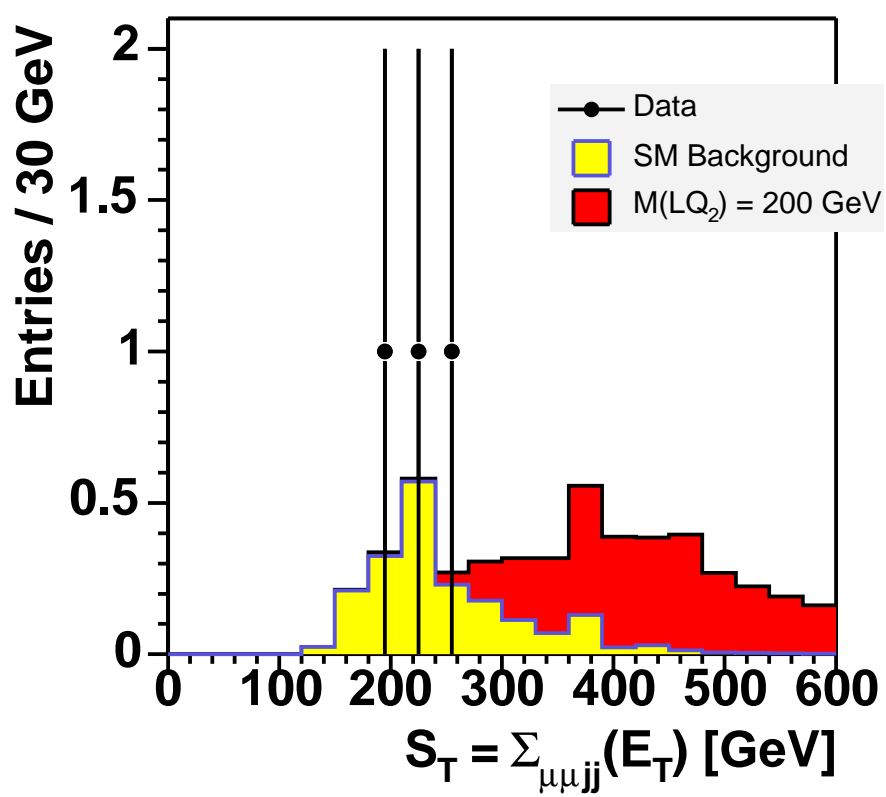
Figure 7.6:   Scalar sum of the transverse energy of the two highest-p_T muons and the two highest-E_T jets.
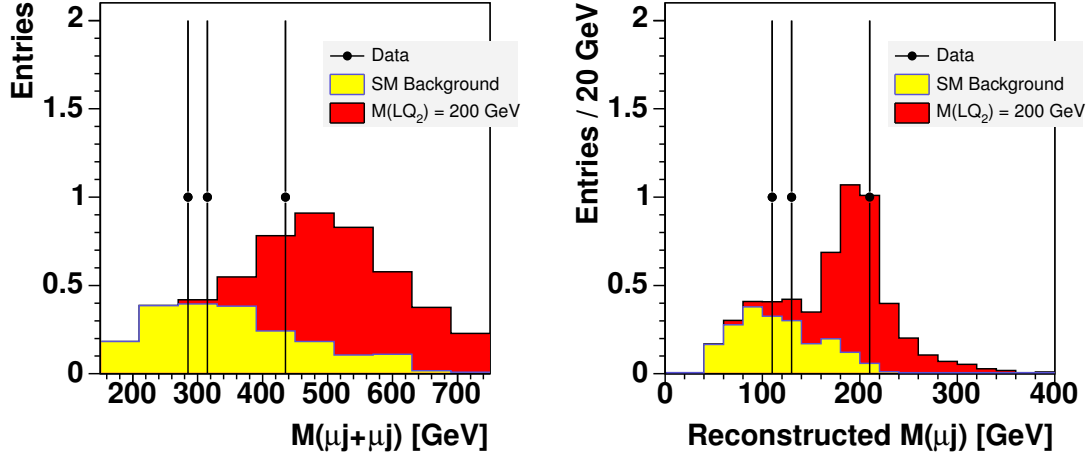
Figure 7.7: Invariant event-mass $M(\mu j + \mu j)$ of the $\mu j + \mu j$ system (left) and reconstructed leptoquark mass $M(\mu j)$ (right): There are two possibilities to combine the two highest-p_T muons with the two highest-E_T jets. Only the combination with the smaller mass difference of the two leptoquark candidates of the event is chosen, and the reconstructed leptoquark mass for this event is the average of the two muon-jet systems.
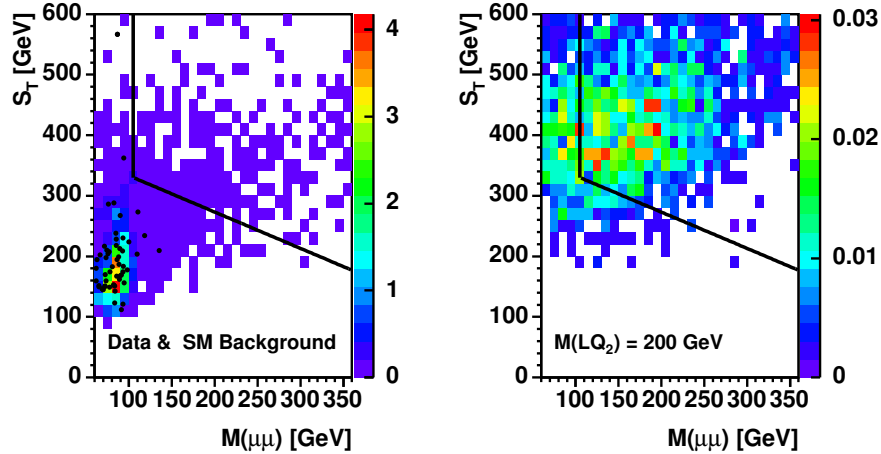
Figure 7.8: S_T, the scalar sum of the transverse energies of the $\mu j + \mu j$ system, versus the di-muon mass. The left picture shows the Standard-Model background (coloured) and the data (black dots) while the right diagram shows the signal distribution for a leptoquark mass of $M(LQ_2) = 200\,$GeV. The black line indicates the final cut: only events to the right of this line pass. The vertical line is defined by $M(\mu\mu) = 105\,$GeV while the sloped line is defined by the point $S_T^{105} = S_T(M(\mu\mu) = 105\,GeV) = 330\,$GeV in the S_T-$M(\mu\mu)$ plane and by the slope $m = -0.6$.

As it turns out, the highest sensitivity for a cut-based analysis is found for a combination of the scalar transverse-energy sum, $S_T = \sum E_T$ (see Figure 7.6), and the di-muon mass $M(\mu\mu)$ (see Figure 7.5). Figure 7.8 shows the S_T distribution versus the di-muon mass for both Standard Model background and leptoquark signal (with a leptoquark mass of $M(LQ_2) = 200\,\text{GeV}$). The black lines in these two-dimensional histograms indicate the optimised cut in the S_T-$M(\mu\mu)$ plane. The vertical part of the cut at $M(\mu\mu) \equiv 105\,\text{GeV}$ is the last cut of the preselection as described above. The slope and the offset (henceforth the offset will be defined as the S_T value S_T^{105} at which the two lines in Figure 7.8 intersect, i.e. at $M(\mu\mu) = 105\,\text{GeV}$) are chosen to give the best separation between signal and background: Events on the upper right sides of the black line are considered signal-like, while events to the left of the line are rejected.

The particular choice of this last cut is based on Monte-Carlo information only. It is obtained by a minimisation of the expected limit σ_exp.

Under the assumption that all data is comprised of Standard-Model processes only (background-only hypothesis), the expected limit is defined as

$$\sigma_\text{exp} = \sum_{n=0}^{N_{max}} P(n|N_{bgd}) \cdot \sigma_{95}(n), \tag{7.4}$$

where $P(n|N_{bgd})$ is the Poisson probability

$$P(n|N_{bgd}) = e^{-N_{bgd}} \frac{N_{bgd}^n}{n!} \tag{7.5}$$

of observing n events. N_{bgd} is the number of expected background events and $\sigma_{95}(n)$ is the 95% confidence level (C.L.) upper cross-section limit for a given set of cuts and for n observed events. The calculation of $\sigma_{95}(n)$ is described in appendix B. In principle, N_{max} is infinity. For this cut optimisation, however, N_{max} is not needed to be larger than ≈ 10 due to the small number of expected background events. In this calculation, N_{max} is chosen such that

$$1 - \sum_{n=0}^{N_{max}} P(n, N_{bgd}) < 0.001, \tag{7.6}$$

thus yielding sufficient accuracy of the order of 0.1%. In order to present meaningful expected limits in this section, both the statistical and the systematic errors associated with the luminosity, the signal efficiency, and N_{bgd} are accounted for, although they will be discussed in a later section of this document. The signal efficiency is taken with respect to the full simulation. Its uncertainty will be described in section 7.2.5.

While the vertical part of the line in Figure 7.8 is fixed by the preselection, there are two free parameters of the second part of the line above $M(\mu\mu) = 105\,\text{GeV}$: the offset S_T^{105} (i.e. the value of S_T at the intersection of the two lines) and the slope m. Figure 7.9

shows the influence of varying the offset with a fixed slope (left) and vice-versa (right) for various leptoquark masses and $\beta = BF(LQ_2 \rightarrow \mu j) = 1$. These curves reveal that for each leptoquark mass there is a different optimal cut (i.e. minimum of the expected limit). However, for reasons of simplicity, one common last cut in the S_T-$M(\mu\mu)$ plane is placed for all potential leptoquark masses: This cut is defined as

$$M(\mu\mu) > 105 \,\mathrm{GeV} \text{ and } S_T > m \cdot (M(\mu\mu) - 105 \,\mathrm{GeV}) + S_T^{105}. \tag{7.7}$$

Herein, $M(\mu\mu)$ and S_T are the values for the di-muon mass and the scalar-energy sum of each event, while $S_T^{105} = 330 \,\mathrm{GeV}$ and $m = -0.6$ denote the optimised offset and the slope of the line-cut, respectively. As can be seen in the right diagram of Figure 7.9, the expected limits for a leptoquark mass of $M(LQ_2) = 200 \,\mathrm{GeV}$ is flat for a broad range of different slopes m. Indeed, the minimum of this curve is at $m = -0.2$ and not at $m = -0.6$, but since this minimum is not pronounced but merely a small fluctuation, and since lighter leptoquarks tend to favour lower values of m, a common slope of the final cut, $m = -0.6$, is chosen. Although the constant $S_T^{105} = 330 \,\mathrm{GeV}$ is optimised for a leptoquark mass of $M(LQ_2) = 200 \,\mathrm{GeV}$, which is the current experimental DØ Run II limit for scalar leptoquarks of the second generation ($\beta = 1$) [6], this still gives a reasonable expected limit for lower leptoquark masses, which is important when placing limits for $\beta < 1$.
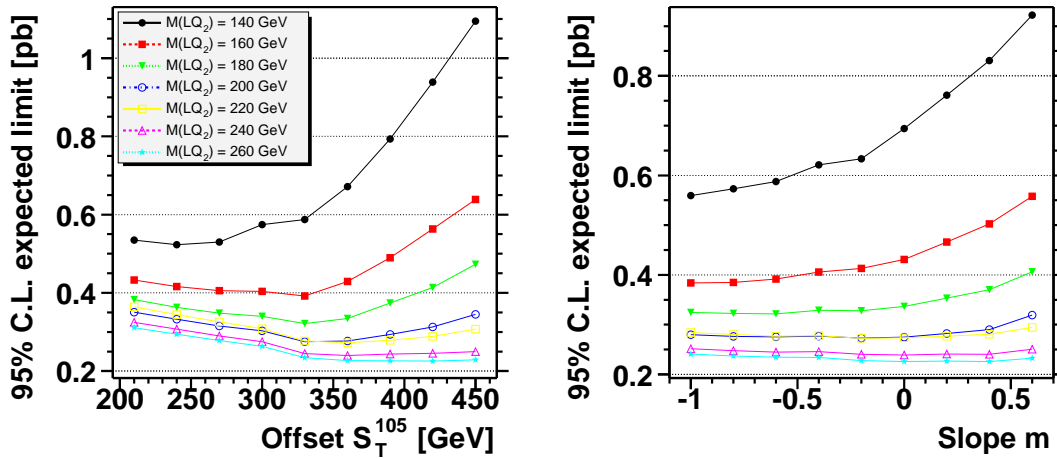
Figure 7.9: Expected limits for various cuts in the S_T-$M(\mu\mu)$ plane. Left: for varying offsets S_T^{105} at the constant slope $m = 0.6$; right: for different slopes m of the cut in the S_T-$M(\mu\mu)$ plane with the constant offset $S_T^{105} = 330 \,\mathrm{GeV}$.

Table 7.3 shows the (expected) numbers of remaining events and the associated statistical errors after each cut in the event selection, presented for data, the SM background, and signal samples. The errors shown in this table are statistical errors only. The number of $\mu j + \mu j$ events in data is in agreement with the expected background from $Z/\gamma^* \rightarrow \mu\mu$

(+jets) processes. A visualisation of the three events surviving the preselection can be found in appendix C.

7.2.3   A Neural Network Analysis

In parallel to the cut-based analysis, described in the previous section, another approach to optimise the separation of signal and background events after the preselection was studied. Based on the preselection of highly energetic $\mu j + \mu j$ events with a di-muon mass greater than 105 GeV, a neural network (NN) is used as a discriminant. The network's output variable reflects a "likelihood" of whether an event is signal- or background-like.

A detailed description of the neural network, which is used in this analysis, can be found in the documentation for the *Multilayer Perceptron* [67]. It was used in several slightly different variations, using different input variables and network parameters, one of which is presented in this section. Table 7.2 summarises the network parameters chosen for this analysis.

Network Parameter	Value
Input Variables	Di-muon mass $M(\mu\mu)$
	Scalar sum S_T
	Event mass $M(\mu j \mu j)$
	Relative μj mass difference $\Delta M(\mu j)/\langle M(\mu j)\rangle$
Number of inner layers	1
Number of inner neurons	2
Signal weight w.r.t. σ	6.0
Learning method	"hybrid"
Training "precision" LTAU	3.0
"Nreset"	50
No. of training epochs	75

Table 7.2: Neural network parameters used for the multilayer perceptron [67]. For the training of the neural network, signal events are given a larger weight ($\times 6$) with respect to the background events from DY-Z/γ^* processes.

The training of the neural network is performed with Monte-Carlo events statistically independent from those used to extract cross-section limits. The "background" events in the training of the network are the simulated DY-Z/γ^* events, i.e. the dominant background. In order to enhance the statistics of the training sample, explicit two-jet events, $Z/\gamma^* + jj \to \mu\mu + jj$, generated with ALPGEN [68], are added. This is motivated by the fact that already the preselection requires two or more jets. The "signal" sample

for the training is comprised of $LQ_2 LQ_2 \rightarrow \mu j + \mu j$ events with a leptoquark mass of $M(LQ_2) = 200\,\text{GeV}$. Again, this signal sample is statistically independent from the sample used for the limit calculation. The majority of these training events was reconstructed with the same reconstruction version as the data, only a small fraction stems from older reconstruction versions. Since DY-Z/γ^* processes are the dominant background, other background processes, such as $t\bar{t}$, are not used for the training of the NN.
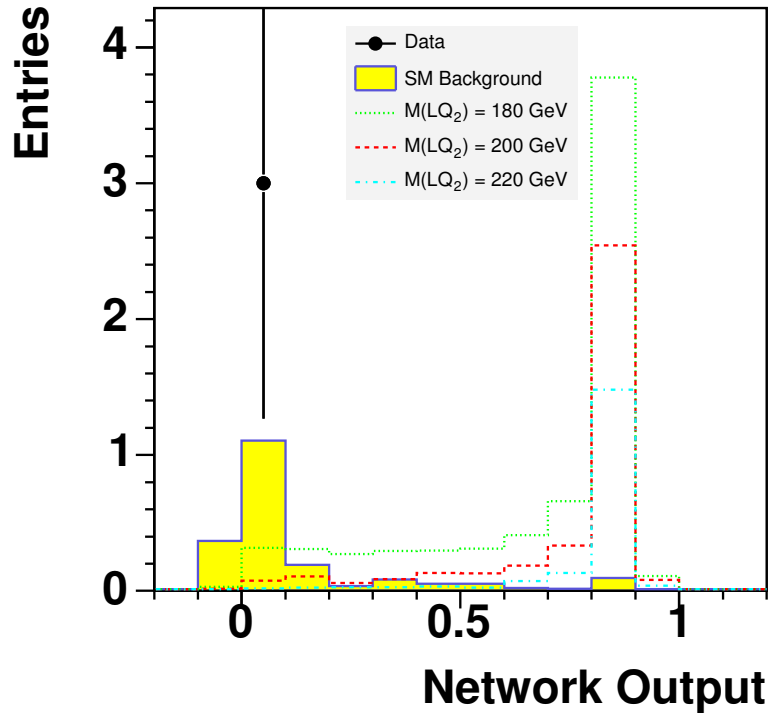
Figure 7.10: Neural network output variable for data (black filled circles) for the expected Standard Model background (filled histograms) and for signal with various leptoquark masses (dashed lines).

Figure 7.10 shows the neural-network output variable for data, SM background and leptoquark signal. As can be seen in Figure 7.11, the resulting separation power of the neural network analysis does not dramatically improve the results from the cut-based analysis. This can be understood from fact that with already quite small numbers of expected background events ($N_{bgd} < 1$, see Table 7.3), the limit mainly depends on the signal efficiency after the last cut. The best-possible last cut can be estimated by assuming 100 % background rejection and an efficiency of 100 % for the events kept in the preselection. The expected cross-section limits from the NN analysis and the two-dimensional final-cut analysis are compared to this hypothetical "best-possible" limit for the given integrated
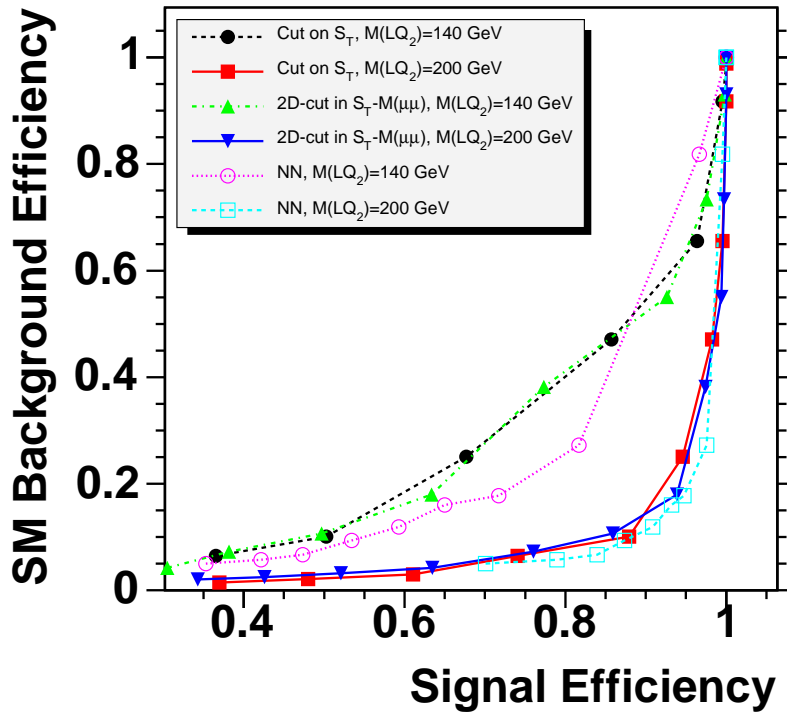
Figure 7.11: SM background acceptance versus signal efficiency for a simple final cut on the variable S_T (as it was used in a previous analysis [56]), for varying offsets S_T^{105} of the two-dimensional cut in the S_T-$M(\mu\mu)$ plane (at fixed slope $m = -0.6$), and for the neural network analysis. The efficiencies shown in these graphs are the efficiencies with respect to all events passing the preselection. The associated errors are not shown in this diagram.
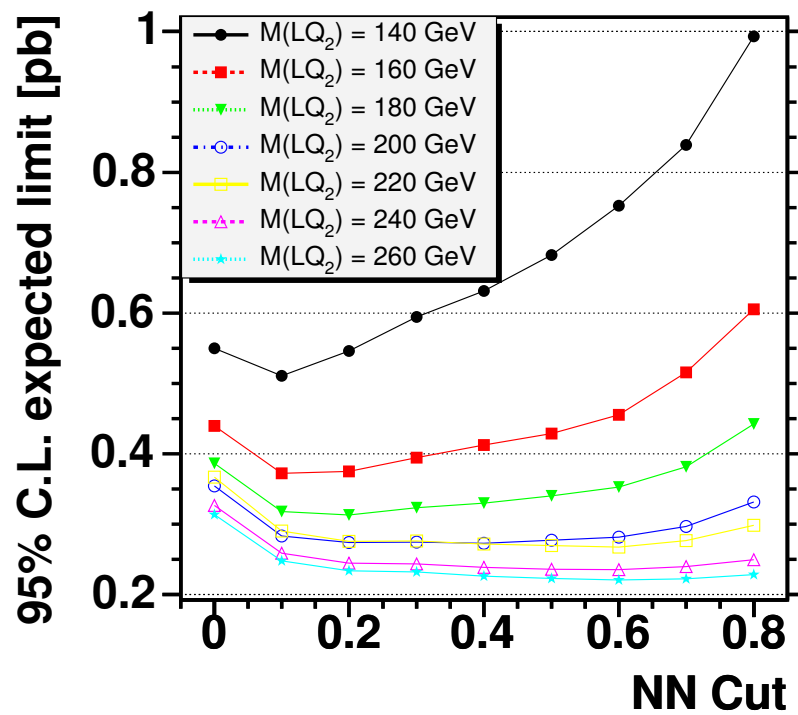
Figure 7.12: Expected limits for the neural network analyses for various cuts on the network output.

luminosity in Table 7.4. The expected limits of the completely cut-based analysis is already close to this "optimum", which is why at this stage with the luminosity available, the neural network can only marginally improve the limits compared to the purely cut-based analysis. The expected limit of the neural-network analysis can be found in Figure 7.12.

7.2.4   Systematic Uncertainties

The systematic uncertainties in the estimation of the effective luminosity was already discussed in section 7.1.2. In the following paragraphs, the main sources of systematic effects and their impact on the number of expected background events will be described.

The systematic errors on the estimated numbers of background events, obtained from Monte-Carlo simulations, arise from uncertainties of the Monte-Carlo normalisation (11%, see section 7.1) as well as the error on the jet-reconstruction efficiency (3% per jet, see section 7.2.1) in data and Monte-Carlo. The uncertainties of the jet-energy scale was estimated by observing the effect on the number of expected background events when shifting the η-dependent uncertainty of the jet-energy correction [53] for simulated events by $\pm 1\sigma$: the effect on the number of expected background events is 22% for DY-Z/γ^* and 7% for $t\bar{t}$ background after the final cut of the purely cut-based analysis. Adding all these uncertainties in quadrature, the systematic error of the expected numbers of events for background (see Table 7.3) then becomes 33% and 15% for DY-Z/γ^* and $t\bar{t}$ background, respectively. The contribution from WW processes is negligible. The corresponding errors for the neural-network analysis are of similar size. Table 7.5 gives a summary of the different sources of uncertainties related to the number of expected background events after the final cut.

7.2.5   Signal Efficiency

Zero events remain from the data, and the signal efficiencies after the last cut are 0.092, 0.106, 0.118, 0.137, 0.133, 0.151, and 0.160 for scalar second-generation leptoquarks with leptoquark masses of 140 GeV, 160 GeV, 180 GeV, 200 GeV, 220 GeV, 240 GeV, and 260 GeV, respectively. These efficiencies are the fraction of events left from the full sample of simulated events, including the tracking efficiency correction as described in section 6.4.1. The differences in the di-muon identification efficiency in data and Monte Carlo as well as the trigger efficiency is not accounted for in the signal efficiencies, since these effects are included in the "effective" luminosity $\tilde{L}$.

While the statistical uncertainties are small, the main systematic uncertainty of the signal efficiency originates from the different topology of the events as compared to Drell-Yan Z processes for which the detector efficiencies have been studied. The muons from

	Cut	Data	DY-Z/γ^*	$t\bar{t}$	$WW \to \mu\nu\mu\nu$	$M_{LQ} = 200\,\mathrm{GeV}$
Preselection	2 isol. muons, $p_T^\mu > 15\,\mathrm{GeV}$, $M(\mu\mu) > 60\,\mathrm{GeV}$	3321	3248 ± 13	0.650 ± 0.018	0.731 ± 0.010	5.24 ± 0.11
	≥ 1 jets, $E_T > 25\,\mathrm{GeV}$	386	410 ± 5	0.638 ± 0.017	0.078 ± 0.003	5.23 ± 0.11
	≥ 2 jets, $E_T > 25\,\mathrm{GeV}$	55	46.8 ± 2.0	0.479 ± 0.015	0.004 ± 0.001	4.54 ± 0.10
	$M(\mu\mu) > 105\,\mathrm{GeV}$	3	1.83 ± 0.30	0.192 ± 0.010	0.001 ± 0.000	3.74 ± 0.09
Choice of	Cut in S_T-$M(\mu\mu)$ plane	0	0.289 ± 0.058	0.076 ± 0.006	0.000 ± 0.000	3.54 ± 0.09
different	NN output > 0.2	0	0.275 ± 0.058	0.078 ± 0.006	0.000 ± 0.000	3.55 ± 0.09
final cuts	NN output > 0.6	0	0.093 ± 0.018	0.036 ± 0.004	0.000 ± 0.000	3.14 ± 0.08

Table 7.3: Cut-flow Table of the preselection and three choices of final cuts for data, Standard-Model backgrounds and signal. The errors shown are statistical errors only, the corresponding systematic uncertainties on the final cuts are summarised in Table 7.5. The final cut in the S_T-$M(\mu\mu)$ plane is described in section 7.2.2 and corresponds to the black line in Figure 7.8. Only those events on the upper right side of the black lines pass this cut. The two last rows of this table show the remaining events and their statistical errors for a cut on the neural-network output at 0.2 and 0.6. For a leptoquark mass of 200 GeV, requiring a neural-network output greater than 0.2 yields the best expected limit.

| Analysis (final cut)	σ_{95}^{exp} [pb] for $M(LQ_2) = 200$ GeV
After preselection	0.38
"Best-possible" limit	0.22
2-dim. cut in S_T-$M(\mu\mu)$ plane	0.27
Neural Network (>0.2)	0.27

Table 7.4: 95% C.L. expected upper limits on the cross-section for scalar leptoquarks of the second generation with a mass of $M(LQ_2) = 200$ GeV. The limits are calculated for different (final) cuts. The "best-possible" limit corresponds to a "perfect" final cut which would reject all background while keeping the signal efficiency of the preselection.

Source of error	Cut-based analysis		NN analysis	
	DY-Z/γ^*	$t\bar{t}$	DY-Z/γ^*	$t\bar{t}$
Monte Carlo statistics	20%	8%	22%	6%
Normalisation	10%	10%	10%	10%
Jet reconstruction	3% / jet	3% / jet	3% / jet	3% / jet
Jet-energy scale	22%	7%	14%	2%
Reweighting of $Z \to \mu\mu$ + jets events	9%		9%	
Total	33%	15%	30%	13%

Table 7.5: Summary of the statistical and systematic errors of the number of background events N_{bgd} after the last cut.

Z-boson decays tend to fly in opposite directions. However, this is not the case for the signal and might lead to systematic effects due to the asymmetry of the DØ muon-system ("bottom hole") originating from uncovered regions in the muon system occupied by support structures.
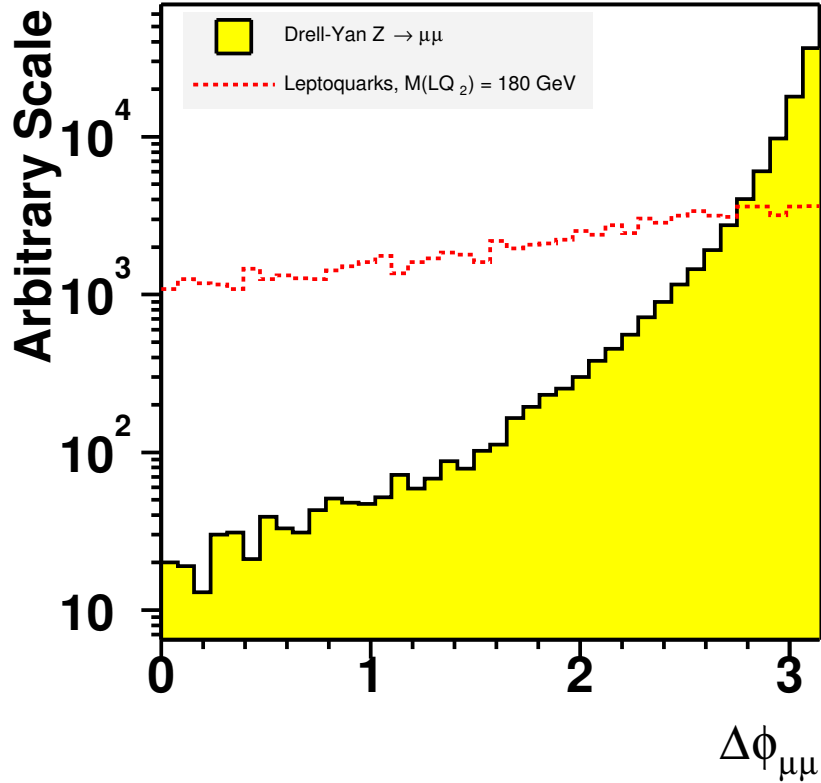
Figure 7.13: ϕ separation of the di-muon system in $Z \to \mu\mu$ ($60\,\text{GeV} < \text{M}(Z/\gamma^*) < 130\,\text{GeV}$) and leptoquark ($M(LQ_2) = 180\,\text{GeV}$) events at generator level.

Figure 7.13 shows the distribution of the ϕ-separation $\Delta\phi_{\mu\mu}$ of the two muons in Drell-Yan Z ($60\,\text{GeV} < \text{M}(Z/\gamma^*) < 130\,\text{GeV}$) and leptoquark ($M(LQ_2) = 180\,\text{GeV}$) events on generator level. While the $Z \to \mu\mu$ events tend to result in back-to-back muons, the direction of the two muons is less correlated for the signal. It turns out that the efficiency indeed drops for small $\Delta\phi_{\mu\mu}$, but the efficiency studies, performed on a sample of well-separated Z events, do not cover high-p_T di-muons that are close to each other in ϕ. In particular, there is hardly a chance of a Z boson to decay into a pair of muons which both end up in the central "bottom hole" at around $4.25 < \phi < 5.15$. This is not the case for most of the muons from leptoquark decays either, but in order to obtain a "worst case" estimate for systematic effects with respect to the muon separation, it was assumed that

those signal events with a muon separation of $\Delta\phi_{\mu\mu} < 0.9$ (this is roughly the size of the "bottom hole") are not detected at all. The fraction of $LQ_2 LQ_2$ events with $\Delta\phi_{\mu\mu} < 0.9$ is 17%. Excluding these events, the signal efficiency drops by 6% of the total signal efficiency.

Varying the jet-energy scale for signal events similar to what was done for the Z and $t\bar{t}$ background, leads to effects of the order of 3% of the total signal efficiency. The dependence on the jet-energy scale is much smaller for signal events due to the higher jet energies in $LQ_2 LQ_2 + X \rightarrow \mu j \mu j + X$ events. The limited statistics of the Monte Carlo sample for the signal leads to an additional uncertainty of 3%. Adding these systematic errors in quadrature, the relative systematic error on the signal efficiency becomes 7.3%.

8 Cross-Section Limits for Scalar Leptoquark Production

8.1 Calculation of the Run II Limits for Scalar Leptoquarks

No excess of data over background was found. Therefore, assuming a branching fraction to charged leptons of $\beta = BF(LQ_2 \to \mu j) = 1$, an upper limit on the cross-section σ_{LQ_2} is calculated, based on the results shown in the last rows of the cut-flow Table 7.3. This calculation is performed as described in appendix B, using the error of the number of expected background events shown in Table 8.1 (the statistical and systematic uncertainty are added in quadrature), and using the "effective" luminosity $\tilde{L} = L \cdot c =(97.2 \pm 9.7)\,\mathrm{pb}^{-1}$. The assumption made for the calculation of the efficiency-corrected limit is that the correction factor c, including the trigger efficiency as well as differences in the reconstruction efficiencies of the data compared to the simulation, is the same for background and signal events.

With a signal acceptance between 0.092 ± 0.007 (for $M_{LQ_2} = 140\,\mathrm{GeV}$) and 0.160 ± 0.012 (for $M_{LQ_2} = 260\,\mathrm{GeV}$) for the cut-based analysis with respect to the full cross-section, the 95 % confidence level upper bound to the cross-section for scalar second-generation leptoquarks is calculated for both the purely cut-based search as well as the analysis using a neural network after the preselection of $\mu j + \mu j$ events. Table 8.1 contains a summary of the resulting upper cross-section limits.

The signal acceptances used in this calculation are determined from the selection cuts applied to the Monte Carlo events only, i.e. the trigger inefficiencies and the differences in the reconstruction efficiencies between data and Monte Carlo are not included. This is a valid approach, because the trigger inefficiency and the difference between the reconstruction efficiencies for the di-muon selection is accounted for in the term $\tilde{L} = L \cdot c$ used in the limit calculation, while the difference in the jet efficiency between data and Monte Carlo is accounted for in the systematic errors assigned to the number of expected background events from Monte Carlo.

The main uncertainty in the calculation of the effective integrated luminosity comes from the theoretical prediction of the cross-section. Although the luminosity error also enters the uncertainty related to the number of SM-background events, the errors from limited Monte-Carlo statistics and the jet-energy scale are the dominant error-sources of N_{bgd} as can be seen in Table 7.5. The same is true for the signal efficiency whose largest uncertainty arises from the difference of the leptoquark event topologies as compared to the SM background. Consequently, the estimated errors used in the calculation of the upper limit of the leptoquark cross-section are treated as independent.

Comparing the upper limits (Table 8.1) to theoretical calculations of the cross-section of scalar second-generation leptoquarks, the lower bound of the leptoquark mass becomes $M_{LQ_2}^{\beta=1} > 200\,\text{GeV}$ for both the cut-based and the neural-network analysis, as can be seen from the curves in Figure 8.1. The branching fraction for the process $LQ_2 LQ_2 \to \mu j + \mu j$ is $\beta^2 = BF(LQ_2 \to \mu j)^2$. Therefore, the cross-section limit for $\beta < 1$ is obtained by multiplying the cross-section limit for $\beta = 1$ with the factor $1/\beta^2$. Figure 8.1 also shows the cross-section limit for $\beta = 1/2$.

In summary, the yellow area in Figure 8.2 shows the excluded region in the β-$M(LQ_2)$ parameter space for second-generation leptoquarks. The 95 % C.L. limits shown in this two-dimensional diagram are the results of the neural-network based analysis, presented in this document.

8.1.1 Combination of Limits with Run I Results

The search for leptoquarks of the second generation has already been performed for $(94 \pm 5)\,\text{pb}^{-1}$ of data recorded at DØ during Run I. This analysis revealed no evidence for the existence of leptoquarks [6]. After the last selection cut, zero events remained in data, while 0.7 ± 0.5 background events were expected. The results for the $\mu j + \mu j$ channel from Run I are shown in Table 8.2.

For a single data sample, the upper limits on the cross-section are calculated by determining a likelihood curve $L \equiv P(\sigma|n, I)$ as a function of the signal cross-section. This likelihood can be interpreted the probability density of observing N_{obs} events for a given signal cross-section σ under the signal+background hypothesis (see appendix B for a description of the limit calculation and the Bayesian likelihood function $P(\sigma|n, I)$).

The 95 % C.L. upper limit σ_{95} is then given by

$$\int_0^{\sigma_{95}} L d\sigma \cdot \left(\int_0^{\infty} L d\sigma \right)^{-1} = 0.95. \qquad (8.1)$$

If the two independent data sets which are to be combined had identical cross-sections, i.e. if the production mechanism and the centre-of-mass energies were the same for both
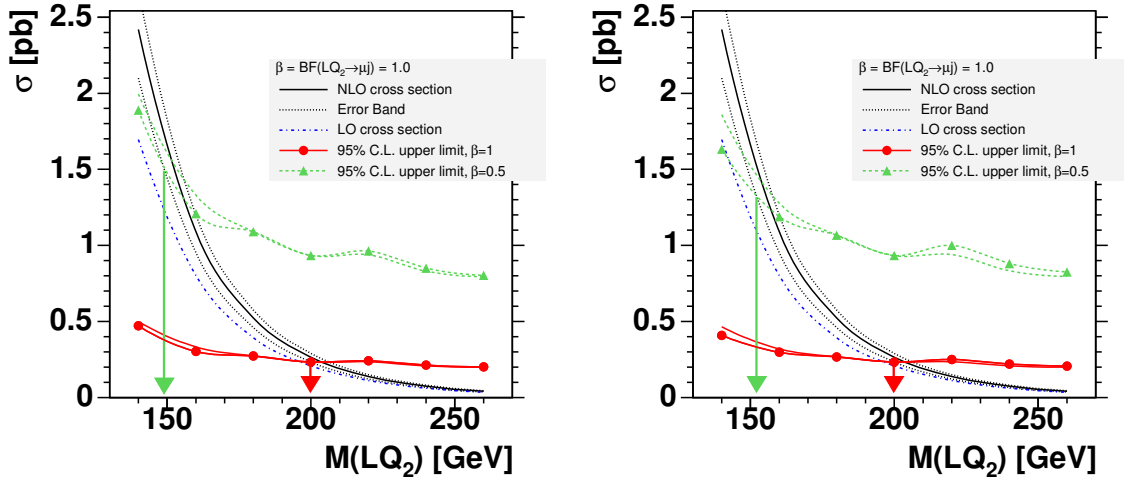
Figure 8.1: Calculated cross sections for scalar second-generation leptoquarks as compared to the 95 % C.L. upper limit on the cross section, assuming 100 % (red circles) and 50 % (green triangles) branching fraction to a muon and a quark, obtained from the cut-based analysis (left) and from the neural-network analysis (right). The LO cross-section is taken from PYTHIA. As a comparison, the second red (green) lines without the data circles (triangles) show the corresponding limits for the analysis with identical cuts for *all LQ$_2$-mass* points. The corresponding lines with data points represent the limits with mass-optimised final cuts. The NLO cross-section is calculated using reference [27] for a centre-of-mass energy of $\sqrt{s} = 1.96$ TeV, where the error is estimated by varying the renormalisation and factorisation scale between $M_{LQ}/2$ and $2M_{LQ}$. The green and red arrows indicate the resulting 95 % C.L. lower limit on the mass of scalar leptoquarks for $\beta = 1/2$ and $\beta = 1$, respectively.

samples, then a combined limit could be calculated by simply multiplying the two likelihood functions, $L = L_1 \cdot L_2$, before solving equation (8.1).

The combination of the Run I and Run II results is a little more involved, however, since the centre-of-mass energies are different, and therefore are the theoretical cross-sections. In order to combine these two results, one can express L_i not as a function of σ but as a function of

$$f \equiv \frac{\sigma}{\sigma_i^{\text{theor.}}} \tag{8.2}$$

where $\sigma_i^{\text{theor.}}$ is the theoretical cross-section for the leptoquark pair-production corresponding to sample i. Then the two different likelihood curves can be multiplied, $L(f) = L_1(f) \cdot L_2(f)$, and the 95 % C.L. upper limit on f can be calculated from

$$\int_0^{f_{95}} L(f)df \cdot \left(\int_0^{\infty} L(f)df \right)^{-1} = 0.95. \tag{8.3}$$
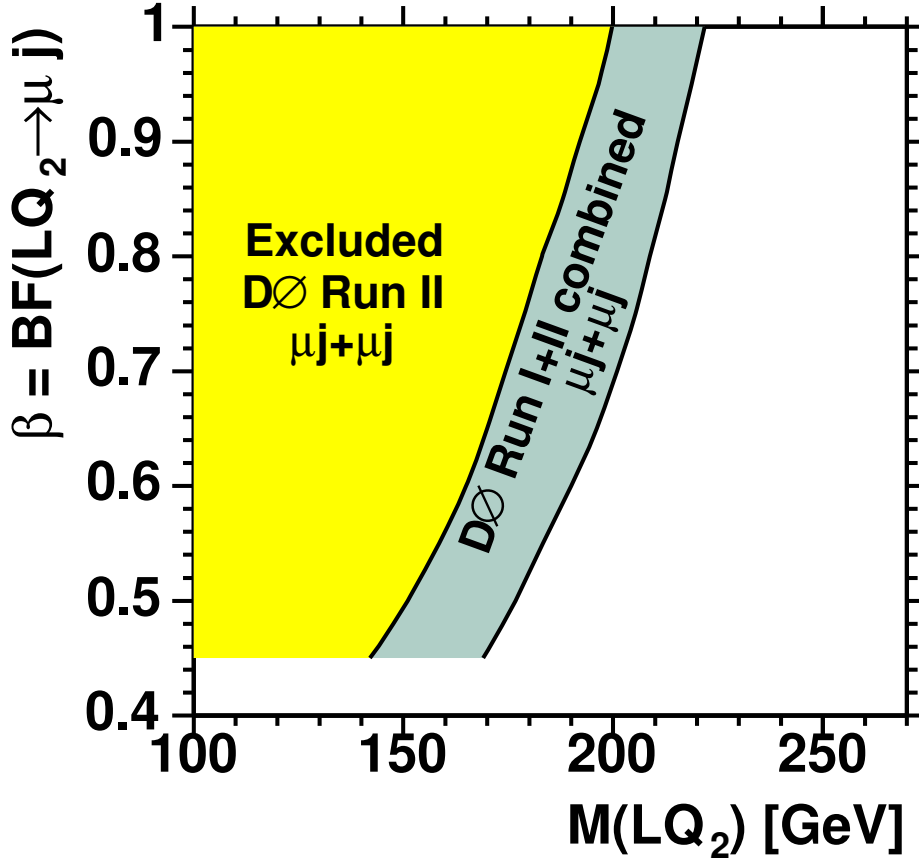
Figure 8.2: This exclusion diagram for scalar leptoquarks of the second generation shows the area of the β-$M(LQ_2)$ parameter space which is excluded by the neural network analysis at 95 % confidence level (yellow area). The grey area, stretching out to even higher values of the leptoquark mass, is the result of a combination of these results with the results from the search for scalar second-generation leptoquarks in $\mu j + \mu j$ events at DØ Run I [6].

Since $\sigma_i^{\text{theor.}}$ in definition (8.2) is the theoretical cross-section for $\beta = 1$, the 95 % C.L. lower mass limit is the intersection of the limit curve with $f_{95} \equiv 1$. Figure 8.3 illustrates this procedure. Since the branching fraction $LQ_2 LQ_2 \rightarrow \mu j + \mu j$ is equal to β^2, the lower limit for $\beta = 1/2$ is the intersection of the limit curve with $f_{95} \equiv 0.25$. Figure 8.2 shows the exclusion limit of the combined DØ Run I and Run II analyses in the $\mu j + \mu j$ channel.

It has been shown that the cross-sections for scalar leptoquark production is significantly lower than for vector leptoquarks while the kinematic distributions for massive leptoquarks are similar [6]. In principle, if the cross-sections for vector leptoquarks were
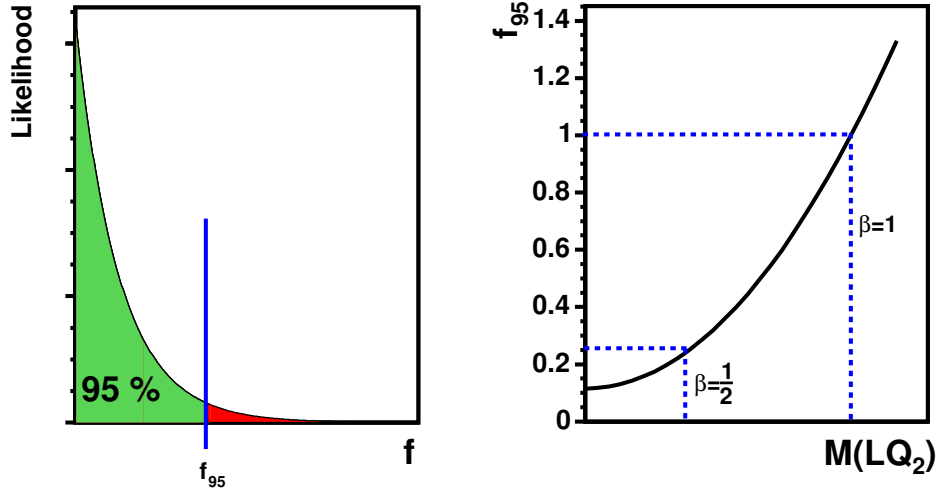
Figure 8.3: Illustration of the procedure to determine combined cross-section limits. The left plot shows the likelihood curve as a function of f (see equation 8.2). The right diagram shows the determined 95 % C.L. curve, f_{95}, as a function of the leptoquark mass. The intersection of f_{95} with 1 (0.25) determines the mass limit for $\beta = 1$ ($\beta = 1/2$).

recalculated for a centre-of-mass energy of $\sqrt{s} = 1.96\,\text{TeV}$, the cross-section limits, determined in this analysis, could also be applied to vector leptoquarks in order to extract lower bounds to the vector-leptoquark mass. Since the differences in the kinematic distributions of scalar and vector leptoquarks have not been compared in this analysis, and since the cross-sections for vector leptoquarks are not yet calculated for the increased collision energy, this thesis focused on the study of scalar leptoquarks while limits for vector-leptoquark pair production are not presented.

8.1.2 Outlook to higher Integrated Luminosities

Since the numbers of expected background events for both the cut-based and the neural network analyses have been shown to be quite low (≤ 1), the (expected) limits predominately depend on the signal acceptances. This is the reason why the neural network analysis at this stage with an integrated luminosity of approximately $114\,\text{pb}^{-1}$ does not lead to significantly better limits, even though the background rejection is higher than in the case of the cut-based search. The dashed red line in figure 8.4 shows the expected 95 % C.L. upper cross-section limit for an integrated luminosity of $1\,\text{fb}^{-1}$, which is approximately 8.8 times the luminosity presented in this document. This limit is calculated with the same signal efficiencies as for the neural-network analysis discussed in this thesis, but with scaled luminosity and number of expected background events. With $1\,\text{fb}^{-1}$ of $p\bar{p}$ events at DØ Run II, the sensitivity of the analysis will significantly improve all

previous results. Adding the complementary analyses in the $\mu j + \nu_\mu j$ and the $\nu_\mu j + \nu_\mu j$ channels, the sensitivity will improve even more, in particular for branching fractions $\beta = BF(LQ_2 \rightarrow \mu j)$ smaller than one.
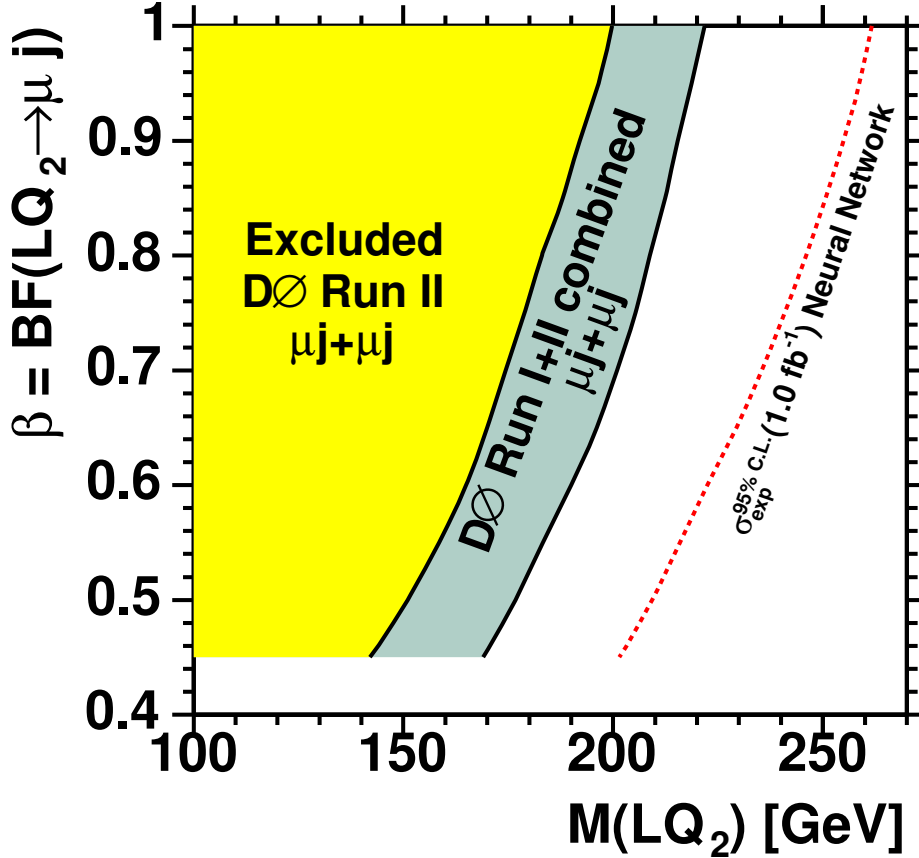
Figure 8.4: This exclusion diagram for scalar leptoquarks of the second generation shows the area of the β-$M(LQ_2)$ parameter space which is excluded by the neural network analysis at 95 % confidence level (yellow area). The grey area, stretching out to even higher values of the leptoquark mass, is the result of a combination of these results with the results from the search for scalar second-generation leptoquarks in $\mu j + \mu j$ events at DØ Run I [6]. The dashed red line indicates the expected limit for the neural-network analysis for $1.0 \, \text{fb}^{-1}$ of $p\bar{p}$ collisions at DØ Run II, which is approximately 8.8 times the statistics as examined in the analysis presented in this document.

Cut-based Analysis: Final cut in the S_T-$M(\mu\mu)$ plane

$M(LQ_2)$	Cut in S_T-$M(\mu\mu)$ plane slope m	offset S_T^{105}	ϵ_{signal}	N_{data}	N_{bgd}	95% C.L. upper limit σ_{95} [pb]	NLO cross-sections [pb] for renorm. scale $M_{LQ}/2$	M_{LQ}	$2\cdot M_{LQ}$
140 GeV		240 GeV	0.092 ± 0.007		1.29 ± 0.34	0.47	2.68	2.42	2.10
160 GeV		300 GeV	0.106 ± 0.008		0.77 ± 0.25	0.30	1.20	1.09	0.952
180 GeV		330 GeV	0.118 ± 0.009		0.37 ± 0.11	0.27	0.575	0.524	0.460
200 GeV	-0.6	330 GeV	0.137 ± 0.010	0	0.37 ± 0.11	0.23	0.289	0.265	0.233
220 GeV		360 GeV	0.133 ± 0.010		0.25 ± 0.08	0.24	0.150	0.138	0.122
240 GeV		360 GeV	0.151 ± 0.011		0.25 ± 0.08	0.21	0.081	0.075	0.066
260 GeV		360 GeV	0.160 ± 0.012		0.25 ± 0.08	0.20	0.044	0.041	0.036

Neural Network Analysis

$M(LQ_2)$	NN cut	ϵ_{signal}	N_{data}	$N_{\text{bgd.}}$	95% C.L. upper limit σ_{95} [pb]
140 GeV	0.1	0.079 ± 0.006		0.55 ± 0.17	0.41
160 GeV	0.1	0.108 ± 0.008		0.55 ± 0.17	0.30
180 GeV	0.2	0.126 ± 0.009		0.35 ± 0.09	0.25
200 GeV	0.2	0.138 ± 0.010	0	0.35 ± 0.09	0.23
220 GeV	0.6	0.137 ± 0.010		0.13 ± 0.03	0.23
240 GeV	0.6	0.146 ± 0.011		0.13 ± 0.03	0.21
260 GeV	0.6	0.156 ± 0.011		0.13 ± 0.03	0.20

Table 8.1: These tables summarise the signal acceptances ϵ_{signal} for various leptoquark masses $M(LQ_2)$, the number of data events N_{data}, the number of expected background events N_{bgd} and the resulting 95 % C.L. upper limit on the cross-section for scalar leptoquark production. In addition, the upper table shows the calculated cross-sections for leptoquark pair-production for different renormalisation scales [27]. The errors shown include statistical and systematic uncertainties, added in quadrature.

LQ_2 Mass [GeV]	Efficiency [%]	$\sigma^{95\,\%\,\text{C.L.}}_{\mu j+\mu j}$ [pb]	$\sigma^{\text{theor.}}_{LQ_2}$ [pb]
140	$10.3 \pm 0.3 \pm 1.1$	0.33	1.5
160	$14.5 \pm 0.3 \pm 1.6$	0.24	0.68
180	$18.9 \pm 0.4 \pm 2.1$	0.18	0.32
200	$21.8 \pm 0.4 \pm 2.1$	0.16	0.16
220	$22.6 \pm 0.4 \pm 2.4$	0.15	0.08
240	$23.5 \pm 0.4 \pm 2.5$	0.15	0.04
260	$24.3 \pm 0.5 \pm 2.6$	0.15	0.02

Table 8.2: Results from the DØ Run I search for second-generation leptoquarks in the $\mu j + \mu j$ channel. The errors on the signal efficiency denote the statistical and systematic uncertainties. $\sigma^{95\,\%\,\text{C.L.}}_{\mu j+\mu j}$ is the 95 % C.L. upper cross-section limit for $\beta = 1$ and $\sigma^{\text{theor.}}_{LQ_2}$ is the theoretical cross-section (NLO) for scalar leptoquarks at the Run I energy, $\sqrt{s} = 1.8\,\text{TeV}$. The number of expected background events for this analysis is 0.7 ± 0.5. [6]

9 Conclusion

Various theories beyond the Standard-Model of Elementary Particle Physics attempt to explain the apparent symmetry between the quark and the lepton sector [1, 10, 14, 15, 16]. Most of these models predict a new gauge interaction which mediates lepton-quark transitions. The corresponding new gauge bosons, called leptoquarks, carry both lepton and quark quantum numbers, and could have masses of the order of $100\,\mathrm{GeV}$ if further constraints on intra-generational interactions are applied [2]. As a consequence, we obtain three different generations of leptoquarks, each only interacting within one generation of quarks and leptons.

In the proton-antiproton collisions at a centre-of-mass energy of $\sqrt{s} = 1.96\,\mathrm{TeV}$, provided by the Run II TeVatron accelerator, leptoquarks of all three generations would mainly be produced in pairs. The sensitivity of the experiment to the signal from second-generation leptoquarks strongly depends on the triggering and the reconstruction of muons. After the main components of the DØ detector had been introduced, this thesis provided a detailed description and a comprehensive study of the efficiencies and rejection capabilities of the DØ Level-2 muon system for triggering highly-energetic muon pairs.

The analysis presented in this document focuses on the search for leptoquarks of the second generation in the channel in which both leptoquarks decay into a muon and a jet: $p\bar{p} \rightarrow LQ_2 + LQ_2 + X \rightarrow \mu j + \mu j + X$. A preselection of highly-energetic di-muon + di-jet events has been presented. About $114\,\mathrm{pb}^{-1}$ of $p\bar{p}$-collision data, collected during Run II with the DØ detector between September 2002 and June 2003, were compared to Monte-Carlo simulations of the expected Standard-Model background as well as simulated scalar leptoquark events. This comparison was performed using both a purely cut-based search as well as a neural-network analysis, in order to separate the Standard-Model background from the signal. Both approaches provide similar discrimination power. No deviation from the Standard Model was observed and the data was shown to be in agreement with the expected background, arising predominately from Drell-Yan $Z/\gamma^* \rightarrow \mu\mu + \mathrm{jets}$ processes.

Since no excess of the data over the expected background was observed, 95 % confidence level (C.L.) upper limits on the cross-section for scalar leptoquark production were calculated, assuming 100 % branching fraction into a muon and a jet, $\beta = BF(LQ_2$

$\rightarrow \mu j) = 1$. These limits have been compared to theoretically calculated cross-sections, and a lower bound to the mass of scalar second-generation leptoquarks of

$$M_{LQ_2}^{\beta=1} > 200\,\text{GeV}$$

was extracted. The corresponding mass-limit for $\beta = 1/2$ is

$$M_{LQ_2}^{\beta=1/2} > 152\,\text{GeV}.$$

The upgraded DØ detector has reached the state of performance and understanding, that—with a similar amount of recorded luminosity—the resulting limit is comparable to that of a previous result of the DØ collaboration, extracted from data collected during Run I in the same channel [6].

Consequently, the results from both analyses in the $\mu j + \mu j$ channel from Run I and Run II have been combined to a single lower limit on the mass of scalar second-generation leptoquarks, yielding

$$M_{LQ_2}^{\beta=1} > 222\,\text{GeV}$$

for $\beta = 1$ at 95 % confidence level. This exclusion limit is the best limit for scalar second-generation leptoquarks from a single experiment to date.

The fact that, despite the slightly increased cross-sections due to the increased centre-of-mass energy of the TeVatron Run II, the limits shown do not exceed those from Run I, lies in the extensive usage of the newly installed detector systems. The new tracking system, for instance, provides a more precise measurement of the muon momenta as compared to Run I, but the efficiencies for tracking highly-energetic charged particles and for identifying muons have yet to be improved. For example, using the latest reconstruction algorithms, the single-track efficiency is expected to exceed 90 % (as compared to approximately 80 % as available in this document), once the data sample will be re-processed.

This study provides efficient tools for a search for second-generation leptoquarks. They result an excellent rejection of the Standard-Model background and can therefore easily be applied to future searches with enhanced integrated luminosity without modification. Together with additional, complementary analyses in the $p\bar{p} \rightarrow LQ_2 LQ_2 + X \rightarrow \mu j + \nu_\mu j + X$ and $p\bar{p} \rightarrow LQ_2 + \mu + X \rightarrow \mu j + \mu + X$ channels, this analysis will be able to push the sensitivity of the DØ experiment to second-generation leptoquarks into regions of the parameter space, which are not examined to date.

A The Forward SLIC Algorithms of the Level-2 Muon Trigger

A.1 The Forward BC-Algorithm

For the forward-BC algorithm, there are two unpacking routines: one for the scintillator hits (the so-called pixels) and one for the drift tube hits (the MDTs, MDT = Mini Drift Tube). The first input information from each channel contains for each event the module-ID of the channel, followed by the number of hits to be expected. The unpacking routine knows from its setup which module-ID, unique to each input channel, to expect. After the incoming data has been checked, the incoming signals as defined in reference [69] are translated and the hits relevant for the specific detector region are stored in arrays for each of the two octants separately.

The data array for the MDT hits contains the following information:

- the layer (B or C) of the hit,

- the plane (1, 2, or 3) within the layer,

- and the tube number (0 to 351 for layer B, 0 to 384 for layer C) within each layer. The tube with index 0 is the closest to the beam pipe.

The array also stores the total number of hits received for each individual plane. A maximum of 15 hits is stored for each plane of each octant.

The data array for the hits in the scintillation counters (pixels) contains the following information:

- the layer (B or C) of the pixel hit,

- the r-index (0 to 11, rising with increasing distance from the beam pipe),

- the ϕ-index (0 to 9) within the octant,

- and the timing of the pixel hit (0 to 255). The number 128 is equivalent to $t = 0$ and the least significant bit represents 1 ns. Zero time is defined as the timing for a hit from a speed-of-light particle coming from the nominal interaction point.

Again, the number of pixel hits in each layer is saved with a maximum number of hits of 15.

After all inputs for both the corresponding octants have been received, the segment-finding algorithm is called. The algorithm then processes the two octants separately, one after the other. In a first step, the algorithm looks for valid MDT hit combinations within the three planes of one layer. There are four kinds of combinations allowed: 1 hit in each of the three planes lines up to a valid hit pattern (3-hit candidate), and the three combinations for which one of the three planes is without a matching hit (2-hit combinations).

The following condition has to be fulfilled for three hits, one in each layer, to be counted as a valid 3-hit candidate: If i_0 is the tube number of the hit in the inner-most plane, then i_1, the tube number of the hit in the second plane, has to be in the vicinity of i_0, such that

$$i_0 - 3 \le i_1 < i_0 + 9 \quad (i_0 - 4 \le i_1 < i_0 + 8) \tag{A.1}$$

is fulfilled for layer B (C). If condition (A.1) is true, then $i_2^{\text{exp.}} = i_0 + 2(i_1 - i_0)$ is the straight projection of the first two hits into the third plane, and i_2, the hit in the third and outer-most plane, is required to fulfil

$$i_2^{\text{exp.}} - 3 \le i_2 < i_2^{\text{exp.}} + 4. \tag{A.2}$$

For a visualisation of the track finding see Figure 4.2. The intervals allowed for the hits in the second and third plane are chosen to optimise the efficiency of the segment finding and were studied with Monte-Carlo simulated single-muon events. If only two hits are available, then the straight-line projection of the two hits into the plane lacking a hit yields the approximate position of the potential (but undetected) third hit, and then the two hits plus the projected third hit are again tested whether they fulfil conditions (A.1) and (A.2). If a valid 2- or 3-hit candidate is found, the algorithm loops over all pixel hits of the corresponding layer and stores all pixel hits which line up with the first hit. This information for each of the at maximum 120 pixel counters which cover one octant is stored in a look-up table, which contains the interval of matching tube numbers.

After all single-layer candidates have been stored in the array of a candidate structure, the candidates of the B-layer are matched with the candidates of the C-layer. This is done by looping over all B-layer candidates (first the 3-hit combinations, then the 2-hit combinations), for which the look-up table provides the following quantities:

- the "centre-of-mass" of the candidate (this is basically the projection of all the available hits into the middle plane),

- the most likely projection of this B-candidate into layer C,

- and the allowed deviation of the "centre-of-mass" of the C-layer candidate from this most likely projection.

Analogously to this table for all possible B-layer combinations, there also is a table for all C-layer combinations available in the look-up tables.

A C-layer candidate is matched to a B-layer candidate, if one or more of the following conditions is fulfilled:

- The "centre-of-mass" of the C-layer candidate is not further away than the allowed deviation from the most likely projection as taken from the B-candidate.

- The "centre-of-mass" of the B-layer candidate is not further away than the allowed deviation from the most likely projection as taken from the C-candidate.

One candidate can only be matched once. If there are more than one possible combination for a candidate, then the combination with the smallest difference to the most likely projections in both layers is chosen. Two matching candidates from the two layers B and C are called *stubs* and they are stored until all potential combinations have been considered.

Since the azimuthal coordinate is determined by the signals in the scintillation counters, the azimuthal angle of the "best" pixel hit associated with the two candidates is determined by their timing: The "best" time is the one closest to zero, i.e. with the smallest value of $|t|$.

Once the stub composition within one of the two octants has ended, the algorithm loops over all stubs identified and determines the following stub properties to be sent out:

- the timing from the best matching pixel hit in layer B,

- the timing from the best matching pixel hit in layer C,

- ϕ, looked up from the best matching pixel of the two layers B and C,

- η (w.r.t. the nominal interaction point and the beam pipe), determined from the straight projection of the BC-stub into the middle of the magnetic toroid between the layers A and B (see Figure 4.2),

- the deflection of the BC-trajectory from the straight line defined by η,

- and the quality assignment of the stub as will be described later.

Having determined the pseudo-rapidity and the *deflection*, the sign of the charge and the momentum of the muon can be estimated by the ALPHA processor.

B Calculation of Confidence Limits

This appendix describes the construction of confidence limits using a Bayesian approach to incorporate errors. A more general description can be found in [66].

The number of expected events, μ, for the signal+background hypothesis is given by

$$\mu = N_{bgd} + \mathcal{L}\varepsilon\sigma, \tag{B.1}$$

where N_{bgd} is the number of expected background events, $\mathcal{L}$ is the integrated luminosity, ε is the signal efficiency, and σ is the cross-section of the signal.

Neglecting all errors on the integrated luminosity $\mathcal{L}$, the signal efficiency ε, and the number of expected background events N_{bgd}, the probability density for observing n events for a given signal cross-section becomes

$$P(n|\sigma, \mathcal{L}, \varepsilon, N_{bgd}) = \frac{e^{-\left(N_{bgd} + \mathcal{L}\varepsilon\sigma\right)} \cdot \left(N_{bgd} + \mathcal{L}\varepsilon\sigma\right)^n}{n!}. \tag{B.2}$$

For such a "perfect" counting experiment without systematical uncertainties, the 95 % C.L. upper limit on the cross-section, σ_{95}, is determined by

$$0.95 = \int\limits_0^{\sigma_{95}} d\sigma\, P(n|\sigma, \mathcal{L}, \varepsilon, N_{bgd}). \tag{B.3}$$

This means that the probability for observing n events for a cross-section greater than σ_{95} is less than 5 %.

The incorporation of (systematic) errors in this probabilistic ansatz, however, is difficult. Without any prior knowledge, it is impossible to interpret this result as a probability that nature realises a cross-section σ. In a Bayesian approach, a specific prior $P(\sigma|I)$ is chosen to convert this measured probability into a probability for the cross-section, given the expected result:

$$P(\sigma|n, I) = \frac{P(n|\sigma, I)\, P(\sigma|I)}{P(n|I)}. \tag{B.4}$$

Herein, *I* represents any relevant prior information in the problem. The denominator on the right of equation (B.4) is determined by the normalisation condition

$$\int\limits_0^\infty d\sigma\, P(\sigma|n,I) = 1.\tag{B.5}$$

The choice of prior for the cross-section for signal poses a problem. The theory of "uninformative priors" suggests a flat prior, $P(\sigma|I) \equiv$ const., i.e. without the measurement all values for σ are equally "probable". In this Bayesian ansatz, the uncertainties on the luminosity, the signal efficiency, and the number of expected background events can be incorporated by expressing the prior not only as a function of the cross-section, but as a function of σ, $\mathcal{L}$, ε, and N_{bgd}:

$$P(\sigma|I) \rightarrow P(\sigma, \mathcal{L}, \varepsilon, N_{bgd}|I) = P(\sigma|I) \cdot P(\mathcal{L}, \varepsilon, N_{bgd}|I).\tag{B.6}$$

This way, the case for vanishing systematic errors is regained by replacing $P(\mathcal{L}, \varepsilon, N_{bgd}|I)$ with delta functions. In the analysis presented in this document, in which the errors are assumed to be uncorrelated, $P(\mathcal{L}, \varepsilon, N_{bgd}|I)$ is factorised as follows:

$$P(\mathcal{L}, \varepsilon, N_{bgd}|I) = P(\mathcal{L}|I)\,P(\varepsilon|I)\,P(N_{bgd}|I) = G(\mathcal{L}, \delta\mathcal{L})\,G(\varepsilon, \delta\varepsilon)\,G(N_{bgd}, \delta N_{bgd}),\tag{B.7}$$

where $G(x, \delta x)$ is a Gaussian with mean x and width δx.

The Bayesian limit for the cross-section with systematic errors, using a flat prior, is calculated by the integration:

$$P(\sigma|n,I) \propto \int\limits_0^\infty d\mathcal{L} \int\limits_0^1 d\varepsilon \int\limits_0^\infty dN_{bgd}\, P(n|\sigma, \mathcal{L}, \varepsilon, N_{bgd})\,G(\mathcal{L}, \delta\mathcal{L})\,G(\varepsilon, \delta\varepsilon)\,G(N_{bgd}, \delta N_{bgd}).$$
$$\tag{B.8}$$

The constant of proportionality is determined by the condition $\int_0^\infty d\sigma\, P(\sigma|n,I) = 1$.

The upper limit σ_β, specified at some level of confidence β, is then defined by:

$$\beta = \int\limits_0^{\sigma_\beta} d\sigma\, P(\sigma|n,I).\tag{B.9}$$

In the limit of vanishing errors, this confidence limit is identical to the one from a purely probabilistic approach.

C Event Displays of Highly-Energetic $\mu\mu+ \geq 2j$ Events

This appendix shows the event displays of the three data events which pass the preselection (see section 7.2.2). The figure captions of this appendix contain the individual event properties. Herein, $M(\mu\mu)$ denotes the $\not{E}_T$-corrected di-muon mass as defined in equation (6.2). These three events pass neither the final cut of the purely cut-based analysis nor the cut on the neural-network output variable. The events are compatible with the Standard-Model background, dominated by Drell-Yan $Z/\gamma^* + X \rightarrow \mu\mu + X$ events.

To guide the eye, the blue circles and the green arrows in the "lego" plots, showing the raw calorimeter entries (before jet-energy scale correction), represent the reconstructed jets and muons, respectively. Note that the green arrows only indicate the muon direction, but not the momentum associated with the muon track.
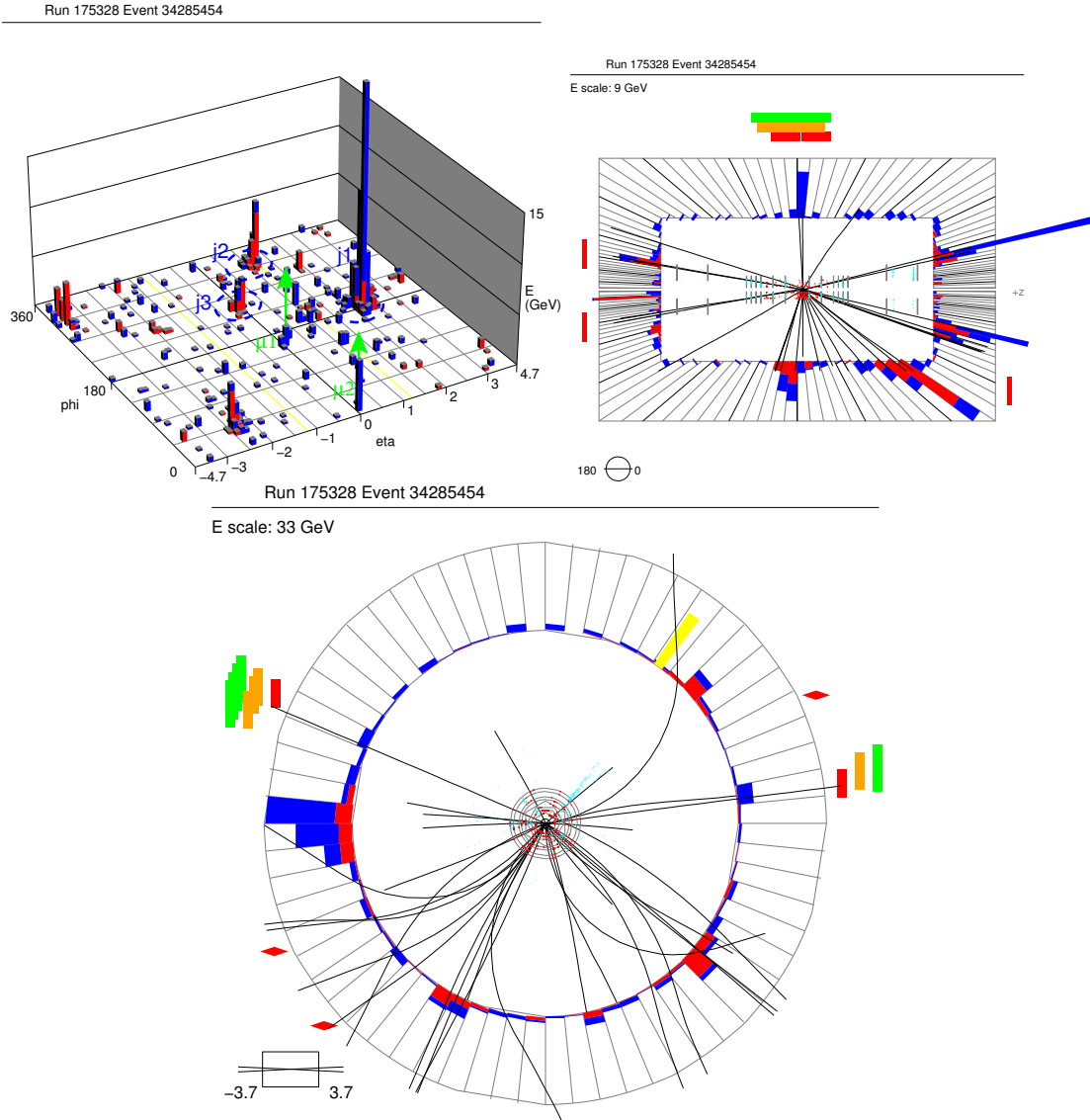
Figure C.1: DØ event display for event 2658694 of run 176214: $M(\mu\mu) = 134$ GeV, $S_T = 209$ GeV, $M(\mu j) = 125$ GeV. The two muons: $p_T = 78$ / 75 GeV, $\phi = 2.74$ / 0.13, $\eta = -0.05$ / 0.0. The three 0.5-cone jets: $E_T = 26$ / 26 / 23 GeV, $\phi = 3.25$ / 5.55 / 4.24, $\eta = 2.13$ / 1.03 / 0.18. The neural-network output variable for this event is 0.03.
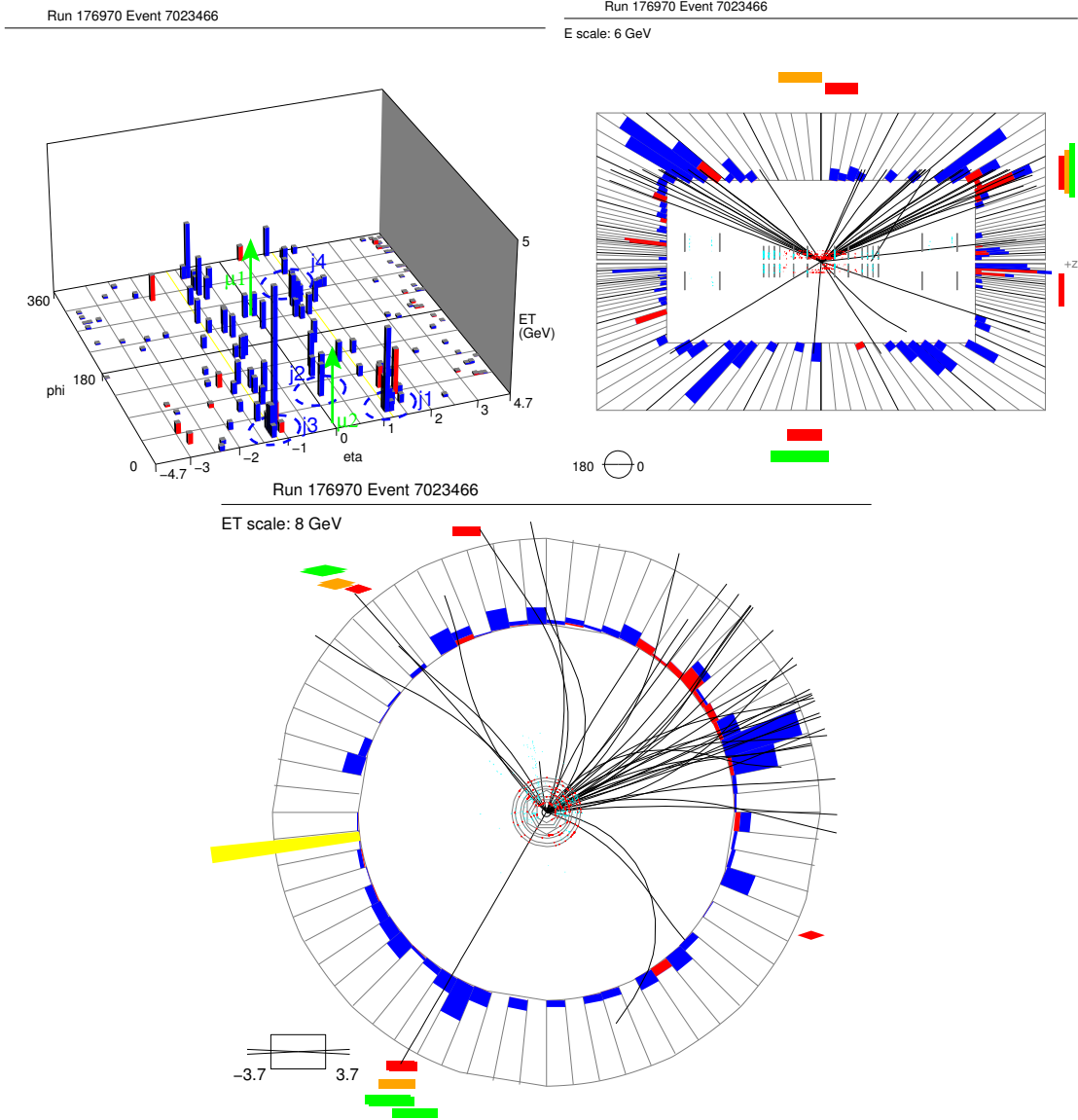
Figure C.2: DØ event display for event 7023466 of run 176970: $M(\mu\mu) = 118$ GeV, $S_T = 266$ GeV, $M(\mu j) = 109$ GeV. The three muons: $p_T = 110 / 24 / 5$ GeV, $\phi = 4.19 / 2.28 / 0.38$, $\eta = -0.08 / 1.40 / 1.27$. The four 0.5-cone jets: $E_T = 38 / 37 / 24 / 23$ GeV, $\phi = 0.50 / 0.84 / 0.39 / 5.51$, $\eta = 1.31 / 0.37 / -1.21 / 0.56$. The neural-network output variable for this event is 0.04.
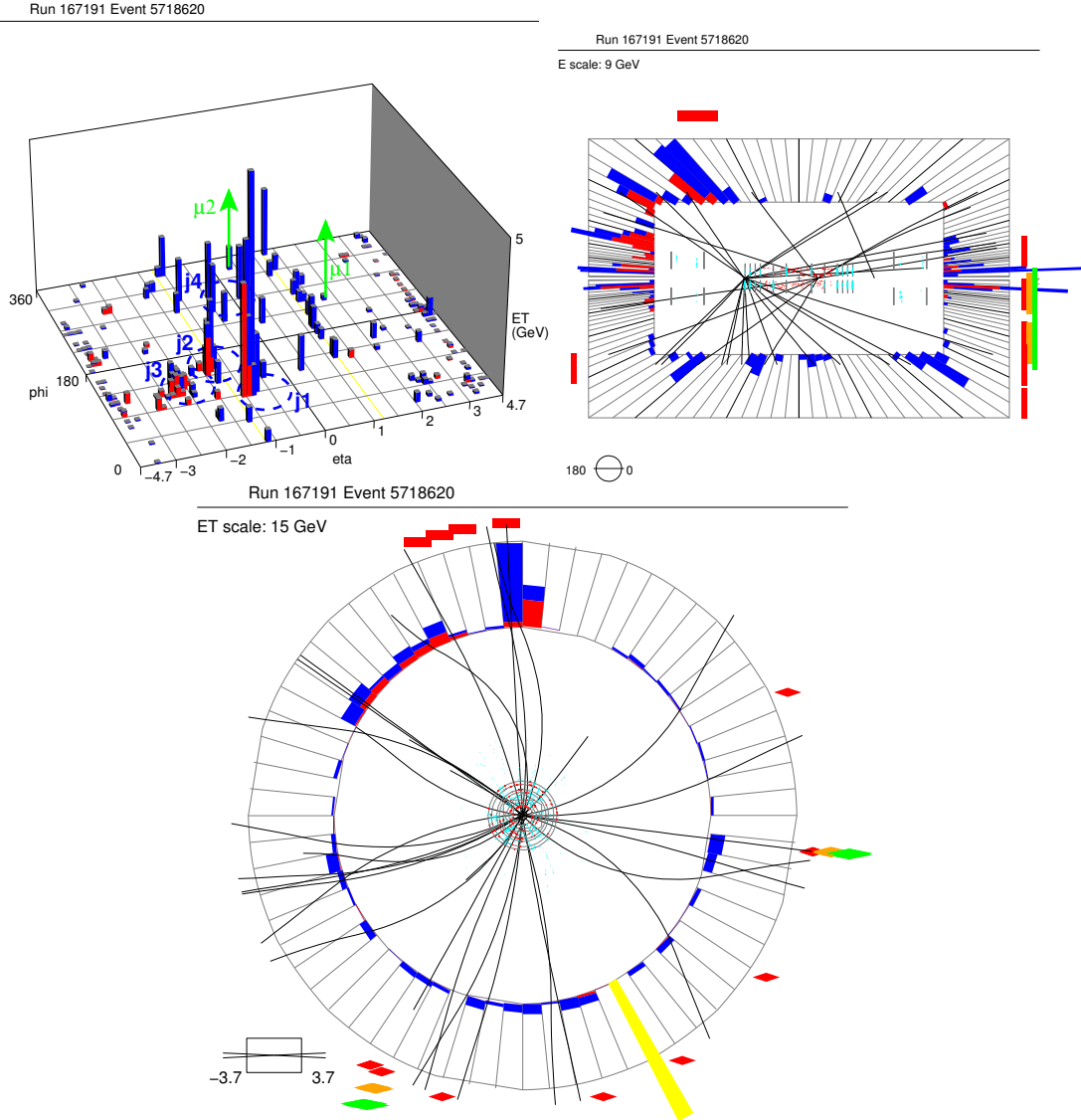
Figure C.3: DØ event display for event 5718620 of run 167191: $M(\mu\mu) = 119\,\text{GeV}$, $S_T = 231\,\text{GeV}$, $M(\mu j) = 205\,\text{GeV}$. The two muons: $p_T = 83\,/\,70\,\text{GeV}$, $\phi = 4.20\,/\,6.16$, $\eta = 1.90\,/\,0.41$. The four 0.5-cone jets: $E_T = 48\,/\,29\,/\,21\,/\,14\,\text{GeV}$, $\phi = 1.59\,/\,2.50\,/\,2.08\,/\,4.78$, $\eta = -0.62\,/\,-1.16\,/\,-1.92\,/\,-0.13$. The neural-network output variable for this event is 0.002. In the upper right picture, one can clearly identify two vertices. The appearance of multiple vertices can, for instance, arise from multiple $p\bar{p}$ collisions in the same bunch crossing.

Bibliography

[1] J. C Pati and A. Salam, *Lepton Number as the Fourth Color*, Phys. Rev. D **10** (1974) 275;
E. Eichten *et al.*, *Signatures for Technicolor*, Phys. Rev. D **34** (1986, 1547);
W. Buchmüller and D. Wyler, *Constraints on SU(5) Type Leptoquarks*, Phys. Lett. B **177** (1986) 377;
E. Eichten *et al.*, *New Tests for Quark and Lepton Substructure*, Phys. Rev. Lett. **50** (1983) 811;
H. Georgi and S. Glashow, *Unity of all Elementary Particle Forces*, Phys. Rev. Lett. **32** (1974) 438.

[2] M. Leurer, *New Bounds on Leptoquarks*, Phys. Rev. Lett. **71** (1993) 1324;
M. Leurer, *A Comprehensive Study of Leptoquark Bounds*, Phys. Rev. D **49** (1994) 333.

[3] The H1 Collaboration, C. Adloff *et al.*, *Observation of events at very high Q^2 in ep collisions at HERA*, Z. Phys. C **74** (1997) 191.

[4] The ZEUS Collaboration, J. Breitweg *et al.*, *Comparison of ZEUS data with standard model predictions for $e^+p \rightarrow e + X$ scattering at high x and Q^2*, Z. Phys. C **74** (1997) 207.

[5] The H1 Collaboration, C. Adloff *et al.*, *A Search for Leptoquark Bosons and Lepton Flavor Violation in Positron-Proton Collisions at HERA*, Eur. Phys. J. C **11** (1999) 447;
The H1 Collaboration, C. Adloff *et al.*, *Search for Compositeness, Leptoquarks and Large Extra Large Dimensions in eq Contact Interaction at HERA*, Phys. Lett. B **479** (2000) 358;
The H1 Collaboration, C. Adloff *et al.*, *A Search for Leptoquark Bosons in e^-p Collisions at HERA*, Phys. Lett. B **523** (2001) 234.

[6] The DØ Collaboration, B. Abbott et al., *Search for Second Generation Leptoquarks in $p\bar{p}$ Collisions at $\sqrt{s} = 1.8$ TeV*, Phys. Rev. Lett. **84** (2000) 2088.

[7] G. Kane, *Modern Elementary Particle Physics*, Addison-Wesley (1993);
     D. J. Griffiths, *Introduction to Elementary Particles*, New York Wiley (1987);
     P. Schmüser, *Feynman-Graphen und Eichtheorien für Experimentalphysiker*, Berlin-
     Springer (1988).

[8] The Particle Data Group (and references therein), K. Hagiwara *et al.*, *The Review of
     Particle Physics*, Phys. Rev. D **66** (2002) 010001.

[9] P. Renton, *Electroweak Interactions, An Introduction to the Physics of Quarks and
     Leptons*, Cambridge University Press (1990).

[10] P. Langacker, *Grand Unified Theories and Proton Decay*, Phys. Rep. **72** (1981) 185.

[11] T.-P. Cheng and L.-F. Li, *Gauge Theory of Elementary Particles*, Clarendon, Oxford
     (1984).

[12] The LEP Electroweak Group, the SLAC Electroweak and Heavy Flavor Groups
     [OPAL Collaboration], *A combination of preliminary electroweak measurements
     and constraints on the standard model*, arXiv:hep-ex/0312023.

[13] W.J. Marciano and G. Senjanović, *Predictions of Supersymmetric Grand Unified
     Theories*, Phys. Rev. D **25** (1982) 3092.

[14] H. Murayama and T. Yanagida, *A Viable $SU(5)$ GUT with light Leptoquark Bosons*,
     Mod. Phys. Let. A **7** (1992) 147.

[15] J. C. Pati and A. Salam, *Unified Lepton-Hadron Symmetry and a Gauge Theory of
     the Basic Interactions*, Phys. Rev. D **8** (1973) 1240.

[16] J. L. Hewett and T. G. Rizzo, *Low-Energy phenomenology of Superstring-inspired
     E_6 Models*, Phys. Rept. **183** (1989) 193.

[17] M. B. Greena and J. M. Schwarz, *Anomaly Cancellation in Supersymmetric $D = 10$
     Gauge Theory and Superstring Theory*, Phys. Lett. B **149** (1984) 117;
     M. B. Green, J. M. Schwarz, and E. Witten, *Superstring Theory*, Cambridge Uni-
     versity Press, Cambridge (1987).

[18] M. M. Boyce, M. A. Doncheski, and H. König,, *Charged Heavy Lepton Production
     in Superstring Inspired E_6 Models*, Phys. Rev. D**55** (1997) 68;
     M. Drees and A. Yamada, *A Decisive Test of Superstring Inspired E(6) Models*,
     Phys. Rev. D **53** (1996) 1586.

[19] S. P. Martin, *A Supersymmetry Primer*, in G. L. Kane (editor): *Perspectives on
     supersymmetry* (1997), or arXiv:hep-ph/9709356 (1999).

[20] M. Kuze and Y. Sirois, *Search for Particles and Forces Beyond the Standard Model at HERA ep and TeVatron p$\bar{p}$ Colliders*, DESY-02-165, arXiv:hep-ex/0211048 (2002).

[21] W. Buchmüller, R. Rückl, and D. Wyler, *Leptoquarks in Lepton-Quark Collisions*, Phys. Lett. B **191** (1987) 442; erratum in Phys. Lett. B **448** (1999) 320.

[22] J. Blümlein and R. Rückl, *Production of Scalar and Vector Leptoquarks in e^+e^- Annihilation*, Phys. Lett. B **304** (1993) 337;
J. Blümlein, E. Roos, and A. Kryukov, *Vector Leptoquark Pair Production in e^+e^- Annihilation*, Phys. Lett. B **392** (1997) 150.

[23] J. Blümlein, E. Roos, and A. Kryukov, *Leptoquark Pair Production in Hadronic Interactions*, Z. Phys. C **76** (1997) 137.

[24] T. G. Rizzo, *Desert GUTs and New Light Degrees of Freedom*, Phys. Rev. D **45** (1992) 3903.

[25] P. H. Frampton and B.-H. Lee, *SU*(15) *Grand Unification*, Phys. Rev. Lett. **64** (1990) 619;
P. H. Frampton and T. W. Kephart, *Higgs Sector and Proton Decay in SU*(15) *Grand Unification*, Phys. Rev. D **42** (1990) 3892;
P. H. Frampton, *Light Leptoquarks as possible Signature of Strong Electroweak Unification*, Mod. Phys. Lett. A **7** (1992) 559.

[26] J. L. Hewett and S. Pakvasa, *Leptoquark Production In Hadron Colliders*, Phys. Rev. D **37** (1988) 3165.

[27] M. Krämer, T. Plehn, M. Spira, P.M. Zerwas, *Pair Production of Scalar Leptoquarks at the TeVatron*, Phys. Rev. Lett. **79** (1997) 341.

[28] H.L. Lai *et al.*, *Improved Parton Distributions from Global Analysis of Recent Deep Inelastic Scattering and Inclusive Jet Data*, Phys. Rev. D **55**, 1280 (1997).

[29] P. B. Straub, *Minireview of Leptoquark Searches*, to appear in the proceedings of 31st International Conference on High Energy Physics (ICHEP 2002), Amsterdam, The Netherlands, 24-31 Jul 2002, arXiv:hep-ex/0212023 (2002).

[30] The DØ Collaboration, S. Abachi *et al.*, *Observation of the Top Quark*, Phys. Rev. Lett. **74** (1995) 2632.

[31] G. Jackson (editor), *The Fermilab Recycler Ring Technical Design Report*, Technical Design Report, FERMILAB-TM-1991;
J. Thompson, *Introduction to Cooling Beams at Fermilab*, FERMILAB-TM-1909 (1994).

[32] The Fermilab Run II Upgrade Committee, *The Run II Luminosity Upgrade at the Fermilab TeVatron*, submitted to the U.S. Department Of Energy, `http://www-bd.fnal.gov/doereview03/docs/Overview7.1.pdf` (2003).

[33] The DØ Collaboration, S. Abachi *et al.*, *The DØ Upgrade: The Detector and its Physics*, Fermilab Pub-96/357-E (1996).

[34] The DØ Collaboration, *The DØ Silicon Tracker Technical Design Report*, DØ Note **2169**, `http://d0server1.fnal.gov/projects/silicon/www/tdr_final.ps` (1994).

[35] S.T. Repond, DØ Note **3925** (unpublished), 7th International Conference on Advanced Technology and Particle Physics, Como, Italy (October 15-19, 2001).

[36] A. Besson, *Étude des événements di-leptons + 4 jets dans le Run II de l'expérience DØ à Fermilab*, Ph.D. thesis, Université Joseph Fourier-Grenoble 1 (2002).

[37] D. Lincoln, *New Technologies in the DØ Central Tracker Upgrade* FERMILAB-Conf-96/137, VIth International Conference of Nuclear Physics on Instrumentation for Experiments at e^+e^- Colliders, Budker Institute of Nuclear Physics, Novosibirsk, Russia (March 1996).

[38] L. Groer, *DØ Calorimeter Upgrades for the TeVatron Run II*, IXth International Conference on Calorimetry in Particle Physics, Annecy, France, (Oct 9-14, 2000).

[39] V. Büscher and J. Zhu, *em_cert: EM Certification Tools*, DØ Note **4171** (unpublished) (2003).

[40] R.J. Culbertson *et al.*, *Low-Scale and Gauge-Mediated Supersymmetry Breaking at the Fermilab TeVatron Run II*, SUSY Working Group Collaboration, arXiv:hep-ph/0008070 (2000).

[41] S. Hagopian, *The Run 2 DØ Muon System at the Fermilab TeVatron*, 7th International Conference on Advanced Technology and Particle Physics, Como, Italy, submitted to World Scientific (2002).

[42] G. Alexeev *et al.*, *Technical Design Report for the DØ Muon Tracking Detector Based on Mini-drift Tubes*, technical design report, DØ Note **3366** (unpublished) (1997);
V. Abramov *et al.*, *Technical Design Report for the DØ forward trigger scintillation counters*, technical design report, DØ Note **3237** (unpublished) (1997).

[43] J. Butler, *Local Muon Momentum Resolution*, DØ Note **4002** (unpublished) (2002).

[44] The DØ Collaboration, S. Abachi *et al.*, *The DØ Upgrade: Forward Preshower, Muon System and Level 2 Trigger*, Fermilab-FN-641 DØ(1996).

[45] A. Maciel, Northern Illinois University, U.S.A., private communication (2001).

[46] J. T. Linnemann for the DØ Level 2 Trigger Group, *The DØ Level 2 Trigger*, Int. J. Mod. Phys. A **16S1C** (2001) 1166.

[47] The DØ Level-2 Group, *The DØ Level-2 Muon Trigger*, DØ Note, in preparation (2004).

[48] T. Christiansen, *The L2-Muon Trigger Performance in* `P11`, DØ Note **4053** (unpublished) (2002).

[49] The DØ trigger group, private communication and DØ internal documents (2003).

[50] T. Sjostrand *et al.*, Computer Physics Commun. **135** (2001) 238.

[51] R. Brun, *GEANT 3 Users Guide*, Technical Report CERN/DD/EE/84-1, CERN (1984);
The DØ Collaboration, *D0GSTAR - DØ GEANT Simulation of the Total Apparatus Response*, internal DØ document, currently available at
`http://www-d0.fnal.gov/computing/MonteCarlo/simulation/d0gstar.html`
(2001).

[52] E. Nurse and P. Telford, *Measurement of $\sigma \cdot BR$ for $Z \to \mu^+\mu^-$ in $p\bar{p}$ Collisions at $\sqrt{s} = 1.96$ TeV*, DØ Note **4284** (unpublished) (2003).

[53] The DØ Jet-Energy Scale Group, *Jet Energy Scale and Resolution for p13 Data and Monte Carlo*, internal DØ documentation, (June 2003)

[54] Raimund Ströhmer, LMU München, Germany, private communication (2003).

[55] T. Christiansen and T. Nunnemann, *Search for 2nd-Generations Leptoquarks in $p\bar{p}$ Collisions at $\sqrt{s} = 1.96$ TeV*, DØ Note **4107** (unpublished) (2003).

[56] T. Christiansen, *Search for 2nd-Generations Leptoquarks in $p\bar{p}$ Collisions at $\sqrt{s} = 1.96$ TeV*, DØ Note **4190** (unpublished) (2003).

[57] M. Agelou, A. Askew *et al.*, *Measurement of the Inclusive $W \to \mu\nu$ Cross-Section in $p\bar{p}$ Collisions at $\sqrt{s} = 1.96$ TeV*, DØ Note **4128** (unpublished) (2003).

[58] D. Whiteson and M. Kado, *Muon Isolation Studies*, DØ Note **4070** (unpublished) (2003).

[59] The DØ Experiment, S. Abachi *et al.*, *W and Z Boson Production in $p\bar{p}$ Collisions at $\sqrt{s} = 1.8$ TeV*, Phys. Rev. Lett. **75** (1995) 1456.

[60] D. Perret-Gallix, *Automatic Calculation and Event Generation for Collider Physics:* `GRACE` *and* `CompHEP`, 14th International Workshop on High-Energy Physics and Quantum Field Theory, Moscow, Russia (**QFTHEP 99**) (1999).

[61] The CTEQ Collaboration, H. L. Lai *et al.*, *Global QCD Analysis of Parton Structure of the Nucleon: CTEQ5 Parton Distributions*, Eur. Phys. J. C **12** (2000) 375.

[62] M. Klute, *Measurement of the $t\bar{t}$ Cross Section at $\sqrt{s} = 1.96$ TeV in μ+jet Events*, DØ Note **4185** (unpublished) (2003).

[63] S. Fu and V. Zutchi, *Search for First Generation Leptoquarks in the Dielectron Channel*, DØ Note **4227** (unpublished) (2003).

[64] F. Abe et al., *Properties of Jets in Z Boson Events from 1.8 TeV $p\bar{p}$ Collisions*, Phys. Rev. Lett. **77** (1996) 448.

[65] A. Kupco et al., *Measurement of the Dijet Mass Cross Section*, Currently available at `http://www-d0.fnal.gov/~kupco/d0_private/dijetmass.ps` (**unpub**lished) (2003).

[66] I. Bertram, G. Landsberg, J. Linnemann, R. Partridge, M. Paterno, and H. B. Prosper, *A Recipe for the Construction of Confidence Limits*, DØ Note **3476** (unpublished) (1999).

[67] J. Schwindling *et al.*, *MLPfit: a Tool for Multi-Layer Perceptrons* (source code and documentation of the MLPfit package), currently available at `http://schwind.home.cern.ch/schwind/MLPfit.html` (2000).

[68] M. L. Mangano, M. Moretti, F. Piccinini, R. Pittau, A. Polosa, *ALPGEN, a generator for hard multiparton processes in hadronic collisions*, arXiv:hep-ph/0206293 (2002), also published in JHEP **0307** (2003) 001;
M. L. Mangano, M. Moretti, R. Pittau, *Multijet matrix elements and shower evolution in hadronic collisions: W B Bbar + N jets as a case study*, arXiv:hep-ph/0108069, Nucl. Phys. B **632** (2002) 343;
F. Caravaglios, M. L. Mangano, M. Moretti, R. Pittau, *A new approach to multijet calculations in hadron collisions*, arXiv:hep-ph/9807570, Nucl. Phys. B **539** (1999) 215.

[69] B. Baldin, O. Bardon, J.M. Butler, M. Fortner, S. Hansen, E. Machado, V. Podstavkov, C. Rotolo, S. Uvarov, and D. Wood, *Muon Data Formats to L2 & L3*, DØ Note **3537** (unpublished) (2001).

Acknowledgements

Curriculum Vitae

Tim Christiansen
Ludwig-Maximilians-Universität Munich
Am Coulombwall 1
D-85748 Garching, Germany

born June 27, 1974 in Schleswig, Germany

Education

1984 - 1993	High school: Lornsenschule (Gymnasium) Schleswig, Germany Leaving certificate (Abitur)
1994 - 2000	Ludwig-Maximilians-Universität Munich, Germany Diploma degree (physics)
1998	CERN Summer Student Programme, Geneva, Switzerland
1999 - 2000	Diploma thesis at the OPAL experiment at CERN
2000 - 2003	Ludwig-Maximilians-Universität Munich, Germany PhD thesis at the DØ experiment at Fermilab near Chicago, U.S.A. (oral exam on March 16, 2004)
2002	CERN Summer School for Particle Physics, Pylos, Greece

Work History

1993 - 1994	Civil service: care for mentally handicapped people, Schleswiger Werkstätten, Schleswig, Germany
1995 - 1997	Part-time work as taxi driver and coaching in maths and physics
Aug-Nov 1996	Max-Planck Institute for Quantum Optics, Garching, Germany: Installation and test of a cryostat; Laser stabilisation using Doppler-free spectroscopy
1997 - 1998	PT employment at Ludwig-Maximilians-Universität Munich, Germany: Test and quality control of muon drift-tubes for the ATLAS experiment
1999 - 2000	During diploma thesis: On-call expert for the time-of-flight detector of the OPAL experiment, including calibrations; Guided tours and presentations for CERN visitors in English, German and French
2000 - 2002	During the two-year stay at Fermilab: System administration of the DØ Linux analysis & desktop cluster, commissioning of the Level-2 (muon) trigger system at DØ (including the test and installation of electronics, writing of muon-tracking algorithms for Level-2 pre-processing, and Level-2 online-expert responsibility), muon identification
2004 -	Postdoc position at LMU Munich (ATLAS experiment).

Munich, December 23, 2003